ODELING AND OBSERVATIONS OF THE ATMOSPHERIC RESPONSE TO SQUALL LINES

Rolf F.A. Hertenstein

Colorado State University

DEPARTMENT OF ATMOSPHERIC SCIENCE

PAPER NO.
434

MODELING AND OBSERVATIONS OF THE ATMOSPHERIC RESPONSE TO SQUALL LINES

Rolf F.A. Hertenstein

The research reported here has been supported by the National Science Foundation under Grant ATM 8510664 and its continuation ATM 8814541. Additional funding was provided by ONR Grant N00014-87-K-0535.

Department of Atmospheric Science
Colorado State University
Fort Collins, Colorado 80523

November, 1988

Atmospheric Science Paper No. 434

ABSTRACT

MODELING AND OBSERVATIONS OF THE ATMOSPHERIC RESPONSE TO SQUALL LINES

In order to study the atmospheric response to a moving squall line a two-dimensional version of the semi-geostrophic theory on isentropic coordinates is used. This model reduces to a system of two equations which includes a predictive equation for the potential pseudo-density σ^* (or inverse potential vorticity), and an invertibility principle which can be solved for the Bernoulli function M^*. Wind and mass fields can be diagnosed from the solution for M^*. The invertibility principle must be solved by an iterative technique; in this study both a simple Gauss-Seidel (GS) relaxation and a Full Multigrid (FMG) method are used and the results using each method are compared. Both methods converge to identical solutions for M^*. Model results show that the squall line leaves in its wake a positive potential vorticity anomaly in the lower troposphere and a negative potential vorticity anomaly in the upper troposphere. Associated with these potential vorticity anomalies are geostrophic flows which have cyclonic shear in the lower troposphere and anticyclonic shear in the upper troposphere. The stability profile is also modified due to the squall line passage such that the lower troposphere is stabilized while the mid to upper troposphere is destabilized.

An observational study is also presented to provide verification for the model results. Supplemental sounding data from the 1985 OK PRE-STORM field study were composited over three times centered around 27 June 1985 0000Z, at which time the squall line had reached its maximum intensity. Cross sections of potential vorticity and the component of the geostrophic flow along the squall line were created at three locations. These show that

the observed squall line has left in its wake a region of relatively high potential vorticity in the lower troposphere and a region of relatively low potential vorticity in the upper troposphere. Cross sections of the component of the observed wind along the squall line are also studied to investigate whether any agreement exists between the observed and geostrophic flows. These flows do show some agreement and indicate cyclonic shear in the lower troposphere and anticyclonic shear in the upper troposphere.

The two-dimensional model incorporates very simple physics, specifically it does not capture the complicated moist physics associated with a squall line. However, comparisons of the model and observational results show that the model does predict many of the features associated with the observed squall line.

Rolf F.A. Hertenstein
Department of Atmospheric Science
Colorado State University
Fort Collins, Colorado 80523
Fall, 1988

ACKNOWLEDGEMENTS

I would first like to thank my advisor, Dr. Wayne Schubert, for his excellent guidance, patient explanations and many helpful suggestions. He has been an ideal advisor; always ready to answer questions and equally important, he allowed me to work unhindered when I had no questions. Thanks also to the other members of my committee; Dr. Richard Johnson with ideas and suggestions for the observational part of the study, and Dr. Gerald Taylor for exposure to new mathematical ideas and techniques.

A very special thanks to Emily Walker for her persistent encouragement of my research efforts and help in data processing. Additionally, her marvelous introduction to hiking, camping and skiing the Rockies on weekends has enabled me to approach each new week of research with refreshed mind and spirit.

Three members of Dr. Schubert's research group, Paul Ciesielski, Gudrun Magnusdottir and Hung-Chi Kuo offered much advice in the current research specifically and for making progress with research in general. I can honestly say that without Paul's numerous suggestions this project would have taken many more months to complete.

I am also grateful to Jennifer Cram and Mike Moran for their help with the observational study, as well as supplying handy tips for dealing with graduate education in general.

Many thanks also to Jenny Martin for her cheerful assistance in the seemingly endless details in preparation of this manuscript.

Funding for this research was provided by the National Science Foundation under Grant ATM 8510664 and its continuation ATM 8814541. Additional funding was provided by ONR Grant N00014-87-K-0535.

TABLE OF CONTENTS

1 INTRODUCTION 1

2 MODELING STUDY 4
2.1 Theory 4
2.1.1 Three-dimensional semi-geostrophic theory 4
2.1.2 Invertibility principle 8
2.1.3 Two-dimensional response to a moving heat source 10
2.2 Numerical procedure 14
2.2.1 General description 14
2.2.2 Invertibility using Gauss-Seidel (GS) relaxation 16
2.2.3 Invertibility using a full multigrid (FMG) method 17
2.2.4 Diagnosing physical fields and transforming to physical space 18
2.3 Numerical experiments and results 18
2.3.1 General model results 18
2.3.2 Comparison of the FMG and GS methods to solve the invertibility 24
2.3.3 Further model experiments 25
2.3.4 Experiments with a stratosphere 31

3 OBSERVATIONAL STUDY 38
3.1 Data 38
3.1.1 Brief description of PRE-STORM 38
3.1.2 Sounding stations and available data 40
3.2 Analysis procedure 40
3.3 Synoptic situation 52
3.4 Observational results 53

4 CONCLUSIONS 91

LIST OF FIGURES

2.1 Characteristic curves $Z(X, Z_0, T)$ as given by the rearrangement of (2.34) for $T = 8$ hr. According to (2.32) the quantity $\sigma^* \sin Z$ is constant along each characteristic. The diagram is in (X, Θ) space for $\Theta_T - \Theta_B = 40$ K, $Q_0 = 7$ K hr^{-1}, $X_0 = 40$ km, and $c = 50$ km hr^{-1}, all of which result in $\alpha = 2.3$. 13

2.2 Isolines of $q = \sigma_0/\sigma^*$ (i.e., potential vorticity measured in units of f) for $T = 8$ hr and $\alpha = 2.3$ in (a) geostrophic space and (b) physical space. The squall line generates a lower tropospheric region of high q and an upper tropospheric region of low q. Note the effect of the coordinate transform from geostrophic to physical space; regions of cyclonic shear have been tightened and regions of anticyclonic shear have been broadened. 19

2.3 (a) $\mathcal{M}$ field resulting from applying the invertibility (2.29) to the q field in Fig. 2.2. $\mathcal{M}$ has units m^{2}s^{-2}. Use of the definition of the deviation Bernoulli field and (2.24) result in the mass and wind fields shown in (b). Pressure (nearly horizontal lines) are in millibars. Solid contours indicate flow into the page, dashed contours indicate flow out of the page; contour interval is 1 ms^{-1}. 21

2.4 Potential vorticity (a) and pressure and wind fields (b) for $T = 16$ hr and $\alpha = 2.3$. q has been nondimensionalized as in Fig. 2.2; pressure and wind fields have the same contour values as Fig. 2.3. 23

2.5 Potential vorticity (a) and pressure and wind fields (b) for $T = 8$ hr, $Q_0 = 7$ K hr^{-1}, $X_0 = 20$ km, and $c = 50$ km hr^{-1}, resulting in $\alpha = 4.6$. Contour values as in Fig. 2.4. 26

2.6 Potential vorticity (a) and pressure and wind fields (b) for $T = 8$ hr, $Q_0 = 7$ K hr^{-1}, $X_0 = 80$ km, and $c = 50$ km hr^{-1}, resulting in $\alpha = 1.15$. Contour values as in Fig. 2.4. 28

2.7 Potential vorticity (a) and pressure and wind fields (b) for $T = 8$ hr, $Q_0 = 3.5$ K hr^{-1}, $X_0 = 40$ km, and $c = 50$ km hr^{-1}, resulting in $\alpha = 4.6$. Contour values as in Fig. 2.4. 29

2.8 Potential vorticity (a) and pressure and wind fields (b) for $T = 8$ hr, $Q_0 = 14$ K hr^{-1}, $X_0 = 40$ km, and $c = 50$ km hr^{-1}, resulting in $\alpha = 1.1$. Contour values as in Fig. 2.4. 30

2.9 Potential vorticity (a) and pressure and wind fields (b) for $T = 8$ hr, $Q_0 = 7$ K hr^{-1}, $X_0 = 40$ km, and $c = 65$ km hr^{-1}, resulting in $\alpha = 3.0$. Contour values as in Fig. 2.4. 32

2.10 Potential vorticity (a) and pressure and wind fields (b) for $T = 8$ hr, $Q_0 = 7$ K hr^{-1}, $X_0 = 40$ km, and $c = 35$ km hr^{-1}, resulting in $\alpha = 1.6$. Contour values as in Fig. 2.4. 33

2.11 (a) An idealized atmospheric σ profile. (b) A standard atmosphere σ profile using data for July and 45 degrees north latitude from the U.S. Standard Atmosphere Supplements. σ is in units of pa K^{-1}. 34
2.12 Potential vorticity (a) and pressure and wind fields (b) for an experiment with a stratosphere and a σ profile as given by Fig. 2.11a. The tropopause is located at 320 K. Contour values as in Fig. 2.4. 35
2.13 Potential vorticity (a) and pressure and wind fields (b) for an experiment with a stratosphere and a σ profile as given by Fig. 2.11b. The tropopause is located at 350 K. Contour values as in Fig. 2.4. 37

3.1 Overview of the surface measurement network showing its boundaries and the locations of various instrumentation (from Meitín and Cunning, 1985). . . . 39
3.2 (a) PRE-STORM radar images for 26 June 1985 2235Z. 43
3.2 (b) PRE-STORM radar images for 27 June 1985 0011Z. 44
3.2 (c) PRE-STORM radar images for 27 June 1985 0029Z. 45
3.2 (d) PRE-STORM radar images for 27 June 1985 0100Z. 46
3.2 (e) PRE-STORM radar images for 27 June 1985 0134Z. 47
3.2 (f) PRE-STORM radar images for 27 June 1985 0156Z. 48
3.3 Map showing the analysis domain and the location of the supplemental stations. The station identifier is labeled next to the actual station location. The dark outline represents the outline of the squall line radar image from 27/0000Z. Also shown are cross sections AA′, BB′, and CC′ (dashed lines). 50
3.4 500 mb heights (solid lines) and vorticity (dashed lines) for (a) 26 June 1985 0000Z and (b) 26 June 1985 1200Z. 54
3.5 500 mb heights (solid lines) and vorticity (dashed lines) for (a) 27 June 1985 0000Z and (b) 27 June 1985 1200Z. 55
3.6 Surface chart for 26 June 1985 1200Z. Precipitation areas are shaded. 56
3.7 Surface chart for 27 June 1985 1200Z. Precipitation areas are shaded. 57
3.8 Geopotential heights (m) at 900 mb. Shaded area represents the 15 dBz or greater radar image at 0000Z. 63
3.9 As in Fig. 3.8 except at 850 mb. 64
3.10 As in Fig. 3.8 except at 700 mb. 65
3.11 As in Fig. 3.8 except at 650 mb. 66
3.12 As in Fig. 3.8 except at 500 mb. 67
3.13 As in Fig. 3.8 except at 400 mb. 68
3.14 As in Fig. 3.8 except at 300 mb. 69
3.15 As in Fig. 3.8 except at 200 mb. 70
3.16 Flow pattern at 900 mb for (a) component of the observed flow along the squall line and (b) component of the geostrophic wind along the squall line. Shaded area represents the 15 dBz or greater radar image at 0000Z. Vector along the abscissa represents 60 ms^{-1}. 71
3.17 As in Fig. 3.16 except at 850 mb. 72
3.18 As in Fig. 3.16 except at 700 mb. 73
3.19 As in Fig. 3.16 except at 650 mb. 74
3.20 As in Fig. 3.16 except at 500 mb. 75
3.21 As in Fig. 3.16 except at 400 mb. 76

3.22 Flow pattern at 300 mb for (a) component of the observed flow along the squall line and (b) component of the geostrophic wind along the squall line. Shaded area represents the 15 dBz or greater radar image at 0000Z. Vector along the abscissa represents 100 ms^{-1}. 77
3.23 Flow pattern at 200 mb for (a) component of the observed flow along the squall line and (b) component of the geostrophic wind along the squall line. Shaded area represents the 15 dBz or greater radar image at 0000Z. Vector along the abscissa represents 100 ms^{-1} in (a) and 200 ms^{-1} in (b). 78
3.24 (a) Cross section of potential temperature along AA′ with pressure as a vertical coordinate. Contour interval is 3 K. (b) Cross section of pressure along AA′ with potential temperature as a vertical coordinate. Contour interval is 25 mb. The darker line represents the 900 mb surface with hashing under that surface. 79
3.25 Cross section of potential vorticity along AA′ (a) with pressure as the vertical coordinate and (b) with potential temperature as a vertical coordinate. Darker line in (b) represents the 900 mb surface with hashing under that surface. 80
3.26 As in Fig. 3.25 except for the component of the observed wind along the squall line $V_{\parallel}$. 81
3.27 As in Fig. 3.25 except for the component of the geostrophic wind along the squall line $V_{g_{\parallel}}$. 82
3.28 As in Fig. 3.24 except along cross section BB′. 83
3.29 As in Fig. 3.25 except along cross section BB′. 84
3.30 As in Fig. 3.26 except along cross section BB′. 85
3.31 As in Fig. 3.27 except along cross section BB′. 86
3.32 As in Fig. 3.24 except along cross section CC′. 87
3.33 As in Fig. 3.25 except along cross section CC′. 88
3.34 As in Fig. 3.26 except along cross section CC′. 89
3.35 As in Fig. 3.27 except along cross section CC′. 90

LIST OF TABLES

2.1 Efficiencies for the GS and FMG methods in terms of CRAY XMP execution time (in sec) per grid point for five cases using different numbers of grid points. 24

3.1 Supplemental OK-PRESTORM sounding availibility. In the Date/Time column an 'F' denotes a full sounding, a 'P' denotes a partial sounding and an 'M' denotes a missing sounding. 41

3.2 Levels to which data is available for stations with partial soundings. 41

Chapter 1

INTRODUCTION

A squall line propagating through the atmosphere not only generates perturbations on the mesoscale but also produces more permanent modifications to the larger scale balanced flow. These modifications can be studied in terms of the balanced response associated with the potential pseudo-density (i.e., the inverse of the Rossby-Ertel potential vorticity) anomaly induced by a moving heat source such as a squall line. This response can be most easily studied with a balanced model; here semi-geostrophic theory is used to study the atmospheric response to a moving squall line.

Hoskins (1975) introduced the geostrophic set of coordinates which depend on components of the geostrophic wind (see (2.5) below). Using this new coordinate he derives a set of equations which are equivalent to the primitive equations with the geostrophic momentum approximation and are referred to as the semi-geostrophic equations. The semi-geostrophic system is a filtered set of equations which provides accurate description of many phenomena which lie beyond description by the quasi-geostrophic equations, including fronts, jets and occluded baroclinic waves.

There exists a duality between the use of geostrophic coordinates in the horizontal and isentropic coordinates in the vertical as first pointed out by Hoskins and Draghici (1977). A version of semi-geostrophic theory using the geostrophic/isentropic coordinates was developed by Schubert et al. (1988). This approach produces a simple mathematical form in which the horizontal ageostrophic components of the flow are entirely implicit and the dynamics reduces to a predictive equation for the potential pseudo-density and an invertibility relation. The solution of the invertibility principle yields the balanced wind and mass fields induced by the potential pseudo-density anomaly.

A two-dimensional version of the model was derived by considering an infinitely long squall line which induces a flow field with all derivatives in the direction along the squall line equal to zero. For the two-dimensional case the potential pseudo-density equation is in a form simple enough to be solved analytically. The invertibility was solved using two different iterative techniques, the first a simple Gauss-Seidel (GS) relaxation method and the second a full multigrid (FMG) method. This allowed a check of the accuracy of the solution to the invertibility by comparing the results obtained by the two methods. Although the more efficient FMG method was not crucial to the solution of the problem, it did allow for an efficiency comparison between the two methods.

The model predicts two-dimensional fields of the inverse potential vorticity from which geostrophic flows along the squall line can be diagnosed. Observational studies of the characteristic features of squall lines (e.g., Ogura and Chen, 1977 and Ogura and Liou, 1980) do not treat these parameters. In order to verify the model simulations, two questions should be answered: 1) What is the nature of any potential vorticity anomaly induced by a squall line, and 2) Are the observed winds along a squall line at all geostrophic, i.e., is any balanced state attained?

The observational study was motivated in an effort to answer these questions. Sounding data was obtained for a squall line case occurring on 26/27 June 1985 during the Oklahoma-Kansas Preliminary Regional Experiment for STORM Central (OK PRESTORM) field study. Soundings from 12 stations in the mesonetwork were composited in time to increase the effective amount of data. A Barnes (1964) objective analysis technique was then applied to the data in order to format it on an evenly spaced grid. Cross sections of potential vorticity as well as the component of the geostrophic and observed flow along the squall line were analysed at three locations.

Finally, a comparison is made between the model output and results from the observational analysis. Even though the model incorporates very simple physics, comparisons show that it does predict many of the features associated with the observed squall line.

Chapter 2 of this study deals with semi-geostrophic theory, describes the numerical methods used to solve the two-dimensional problem and discusses results of several experiments using the model. The data and analysis procedures used, as well as the results

obtained, are discussed in Chapter 3. Comparisons between model output and observations are made along with concluding remarks and recommendations for further study in Chapter 4.

Chapter 2

MODELING STUDY

In this chapter we begin with a discussion of the three-dimensional version of semi-geostrophic theory on isentropic coordinates. The combination of geostrophic/isentropic coordinates yields a closed system with a predictive equation for the potential pseudo-density (see (2.22) below) and an invertibility relation (see (2.27) below). From (2.27) wind and mass fields can be diagnosed (see (2.24) below). A simplification of the theory to two dimensions is discussed with an application to a mid-latitude squall line. The second section covers the numerical procedure used, which included two schemes to solve the invertibility: a simple Gauss-Seidel relaxation scheme and a full multigrid method. The final section describes the numerical experiments and results obtained using the model.

2.1 Theory

2.1.1 Three-dimensional semi-geostrophic theory

We begin our discussion of three-dimensional semi-geostrophic theory with the f-plane system of equations with the geostrophic momentum approximation (Eliassen, 1948). The system, assumed frictionless and using potential temperature as a vertical coordinate becomes

$$\frac{Du_g}{Dt} - fv_a = 0, \tag{2.1}$$

$$\frac{Dv_g}{Dt} + fu_a = 0, \tag{2.2}$$

$$\frac{\partial M}{\partial \theta} = \Pi, \tag{2.3}$$

$$\frac{D\sigma}{Dt} + \sigma\left(\frac{\partial u}{\partial x} + \frac{\partial v}{\partial y} + \frac{\partial \dot{\theta}}{\partial \theta}\right) = 0, \tag{2.4}$$

where (u, v) are the horizontal components of the total velocity, $(u_g, v_g) = f^{-1}(-\partial M/\partial y, \partial M/\partial x)$ the components of geostrophic velocity, $(u_a, v_a) = (u - u_g, v - v_g)$ the components of the ageostrophic velocity, $\Pi = c_p\,(p/p_0)^\kappa$ the Exner function, $M = \theta\Pi + \phi$ the Montgomery potential, $\sigma = -\partial p/\partial\theta$ the pseudo-density, and $D/Dt = \partial/\partial t + u\partial/\partial x + v\partial/\partial y + \dot{\theta}\partial/\partial\theta$ the total derivative. The vertical theta velocity $\dot{\theta}$ is regarded as known or parameterized and is included for diabatic applications.

Hoskins (1975) introduced a set of geostrophic coordinates

$$(X, Y, \Theta, T) = (x + v_g/f, y - u_g/f, \theta, t). \tag{2.5}$$

Since this new coordinate is a function of the geostrophic flow there will be a distortion in (X, Y, Θ, T) space depending on the strength of the flow. In geostrophic space there is a stretching of the coordinate in regions of cyclonic shear while a tightening occurs in regions of anticyclonic shear (Hoskins, 1975, Fig. 1). By (2.5) semi-geostrophic theory is limited to regions of small anticyclonic shear; during an inverse coordinate transform regions of large anticyclonic shear may produce a non-monotonic $x(X)$.

Derivatives in (x, y, θ, t) space are related to derivatives in (X, Y, Θ, T) space by

$$\frac{\partial}{\partial t} = \frac{\partial X}{\partial t}\frac{\partial}{\partial X} + \frac{\partial Y}{\partial t}\frac{\partial}{\partial Y} + \frac{\partial}{\partial T}, \tag{2.6}$$

$$\frac{\partial}{\partial x} = \frac{\partial X}{\partial x}\frac{\partial}{\partial X} + \frac{\partial Y}{\partial x}\frac{\partial}{\partial Y}, \tag{2.7}$$

$$\frac{\partial}{\partial y} = \frac{\partial X}{\partial y}\frac{\partial}{\partial X} + \frac{\partial Y}{\partial y}\frac{\partial}{\partial Y}, \tag{2.8}$$

$$\frac{\partial}{\partial \theta} = \frac{\partial X}{\partial \theta}\frac{\partial}{\partial X} + \frac{\partial Y}{\partial \theta}\frac{\partial}{\partial Y} + \frac{\partial}{\partial \Theta}. \tag{2.9}$$

The above derivative transformations are obtained by noting the functional dependence of the coordinates as defined in (2.5). It is important to note that although $t = T$ and $\theta = \Theta$, $\partial/\partial t \neq \partial/\partial T$ and $\partial/\partial\theta \neq \partial/\partial\Theta$.

Using (2.5), (2.1) and (2.2) it can easily be shown that

$$\frac{DX}{Dt} = \frac{Dx}{Dt} + \frac{1}{f}\frac{Dv_g}{Dt} = u - u_a = u_g, \tag{2.10}$$

$$\frac{DY}{Dt} = \frac{Dy}{Dt} - \frac{1}{f}\frac{Du_g}{Dt} = v - v_a = v_g. \tag{2.11}$$

These two relations, together with (2.6)-(2.9) imply that the operator

$$\frac{D}{Dt} = \frac{\partial}{\partial t} + u\frac{\partial}{\partial x} + v\frac{\partial}{\partial y} + \dot{\theta}\frac{\partial}{\partial \theta} \tag{2.12}$$

can also be written as

$$\frac{D}{Dt} = \frac{\partial}{\partial T} + u_g\frac{\partial}{\partial X} + v_g\frac{\partial}{\partial Y} + \dot{\theta}\frac{\partial}{\partial \Theta}. \tag{2.13}$$

A major advantage of the transformation from (x, y, θ, t) space to (X, Y, Θ, T) space is the change from advection by (u, v) in (2.12) to advection by (u_g, v_g) in (2.13). Thus, given information only about the distribution of the Montgomery potential field, the advective quantities (u_g, v_g) can be calculated and (2.13) can then be applied. The ageostrophic components (u_a, v_a) become implicit in the coordinate transformation.

The vertical component of the vorticity equation can be derived from (2.1) and (2.2). It takes the form

$$\frac{D\varsigma}{Dt} + \varsigma\left(\frac{\partial u}{\partial x} + \frac{\partial v}{\partial y}\right) - \left(\xi\frac{\partial}{\partial x} + \eta\frac{\partial}{\partial y}\right)\dot{\theta} = 0, \tag{2.14}$$

where the components of the three dimensional absolute vorticity vector are given by

$$(\xi, \eta, \varsigma) = f\left(\frac{\partial(X,Y)}{\partial(y,\theta)}, \frac{\partial(X,Y)}{\partial(\theta,x)}, \frac{\partial(X,Y)}{\partial(x,y)}\right)$$

$$= \left(-\frac{\partial v_g}{\partial \theta} + \frac{1}{f}\frac{\partial(u_g, v_g)}{\partial(y,\theta)}, \frac{\partial u_g}{\partial \theta} + \frac{1}{f}\frac{\partial(u_g, v_g)}{\partial(\theta,x)}, f + \frac{\partial v_g}{\partial x} - \frac{\partial u_g}{\partial y} + \frac{1}{f}\frac{\partial(u_g, v_g)}{\partial(x,y)}\right). \tag{2.15}$$

We can now eliminate the horizontal divergence between (2.4) and (2.14) to obtain

$$\sigma\frac{D\varsigma}{Dt} - \varsigma\frac{D\sigma}{Dt} - \sigma\left(\xi\frac{\partial}{\partial x} + \eta\frac{\partial}{\partial y} + \varsigma\frac{\partial}{\partial \theta}\right)\dot{\theta} = 0, \tag{2.16}$$

Inverting (2.7) and (2.8) to obtain

$$\frac{\varsigma}{f}\frac{\partial}{\partial X} = \frac{\partial Y}{\partial y}\frac{\partial}{\partial x} - \frac{\partial Y}{\partial x}\frac{\partial}{\partial y}, \tag{2.17}$$

$$\frac{\varsigma}{f}\frac{\partial}{\partial Y} = -\frac{\partial X}{\partial y}\frac{\partial}{\partial x} + \frac{\partial X}{\partial x}\frac{\partial}{\partial y}, \tag{2.18}$$

and using (2.17) and (2.18) in (2.9) to obtain

$$\varsigma\frac{\partial}{\partial\Theta}=\xi\frac{\partial}{\partial x}+\eta\frac{\partial}{\partial y}+\varsigma\frac{\partial}{\partial\theta}, \tag{2.19}$$

we can write (2.16) as

$$\frac{D\sigma^*}{Dt}+\sigma^*\frac{\partial\dot{\theta}}{\partial\Theta}=0, \tag{2.20}$$

where

$$\sigma^*=\frac{f}{\varsigma}\sigma \tag{2.21}$$

is the potential pseudo-density. Using (2.13) and (2.24) we can write (2.20) in the flux form

$$\frac{\partial\sigma^*}{\partial T}+\frac{\partial}{\partial X}\left(u_g\sigma^*\right)+\frac{\partial}{\partial Y}\left(v_g\sigma^*\right)+\frac{\partial}{\partial\Theta}\left(\dot{\theta}\sigma^*\right)=0, \tag{2.22}$$

which serves as the fundamental predictive equation of the model.

Recalling the definition of σ, it can be seen that the potential pseudo-density σ^* is simply the inverse of potential vorticity q. That is,

$$q=-\frac{\varsigma}{f}\frac{\partial\theta}{\partial p}.$$

A physical interpretation of σ^* is analogous to that of q. Consider a cylindrically shaped mass of fluid bounded on the top and bottom by two isentropic surfaces. Assuming initially that the fluid is spinning cyclonically relative to the earth, i.e., $\varsigma > f$, and that the flow is adiabatic it can be seen from (2.20) that

$$\frac{D\sigma^*}{Dt}=\frac{D}{Dt}\left(\frac{f}{\varsigma}\sigma\right)=0.$$

From the above equation we conclude that σ/ς must be conserved, so that if σ decreases ς also decreases. Imagine a situation in which the mass of the fluid is rearranged in such a way that mass moves outward without crossing the top or bottom isentropic surface. In this case pressure increases between the two isentropic surfaces and thus σ decreases and ς must therefore also decrease for conservation to hold. We can then interpret σ^* as the pseudo-density that the mass of fluid would have if the relative vorticity were reduced to f under the adiabatic rearrangement process. In the case of an originally anticyclonically

spinning fluid, i.e., $\varsigma < f$, fluid moving inward would cause a simultaneous increase in both σ and ς. Because of the simple form that (2.20) takes it is a much easier variable for which to solve than its inverse, the more commonly used potential vorticity. For a discussion of integral constraints on the potential vorticity field the reader is referred to Haynes and McIntyre (1987).

2.1.2 Invertibility principle

The potential pseudo-density σ^* is a combination of the mass field σ and the wind field ς. However, since σ is related to M through hydrostatic balance and ς is related to M through (2.15) and geostrophic balance, σ^* depends only on M. Thus, everything can be obtained from σ^* if we can somehow invert it to obtain M. Actually, rather than invert for M, it is more convenient to invert for the Bernoulli function

$$M^* = M + \frac{1}{2}\left(u_g^2 + v_g^2\right). \tag{2.23}$$

Using this new variable, it can be shown that the geostrophic and hydrostatic relations in (X, Y, Θ, T) space take the form

$$(fv_g, -fu_g, \Pi) = \left(\frac{\partial M^*}{\partial X}, \frac{\partial M^*}{\partial Y}, \frac{\partial M^*}{\partial \Theta}\right), \tag{2.24}$$

which is identical to the form taken in (x, y, θ, t) space. The relation between M^* and σ^* is derived as follows. From the definition of σ^* we have

$$\frac{f}{\varsigma}\frac{\partial \Pi}{\partial \Theta} + \Gamma\sigma^* = 0, \tag{2.25}$$

where $\Gamma = d\Pi/dp = \kappa\Pi/p$. This last equation can be written

$$\frac{\partial(x, y, \Pi)}{\partial(X, Y, \Theta)} + \Gamma\sigma^* = 0. \tag{2.26}$$

Expressing x and y in terms of u_g and v_g by (2.5), and then using (2.24), we can write (2.26) as

$$\frac{1}{f^4}\left[\left(f^2 - \frac{\partial^2 M^*}{\partial X^2}\right)\left(\frac{\partial^2 M^*}{\partial Y \partial \Theta}\right)^2 + \left(f^2 - \frac{\partial^2 M^*}{\partial Y^2}\right)\left(\frac{\partial^2 M^*}{\partial X \partial \Theta}\right)^2\right.$$
$$\left. +2\left(\frac{\partial^2 M^*}{\partial X \partial Y}\right)\left(\frac{\partial^2 M^*}{\partial Y \partial \Theta}\right)\left(\frac{\partial^2 M^*}{\partial \Theta \partial X}\right)\right] + \frac{1}{f^2}\left\{f^2 - \frac{\partial^2 M^*}{\partial X^2} - \frac{\partial^2 M^*}{\partial Y^2}\right.$$

$$+\frac{1}{f^2}\left[\left(\frac{\partial^2 M^*}{\partial X^2}\right)\left(\frac{\partial^2 M^*}{\partial Y^2}\right)-\left(\frac{\partial^2 M^*}{\partial X \partial Y}\right)^2\right]\Bigg\}\frac{\partial^2 M^*}{\partial \Theta^2}+\Gamma\sigma^*=0. \qquad (2.27a)$$

If the upper boundary is an isentropic and isobaric surface with potential temperature Θ_T and Exner function Π_T, the upper boundary condition for (2.27a) is simply

$$\frac{\partial M^*}{\partial \Theta}=\Pi_T \qquad \text{at} \qquad \Theta=\Theta_T. \qquad (2.27b)$$

If we neglect the effects of topography and assume that the lower boundary is the constant height surface $\phi=0$ and the isentropic surface $\Theta=\Theta_B$, then $M=\Theta\Pi$ at $\Theta=\Theta_B$. Written in terms of M^*, this lower boundary condition becomes

$$\Theta\frac{\partial M^*}{\partial \Theta}-M^*+\frac{1}{2f^2}\left[\left(\frac{\partial M^*}{\partial X}\right)^2+\left(\frac{\partial M^*}{\partial Y}\right)^2\right]=0 \qquad \text{at} \qquad \Theta=\Theta_B. \qquad (2.27c)$$

The lateral boundary conditions depend on the particular application.

Equations (2.22), (2.24) and (2.27) form a closed system. The computational scheme is as follows: knowing σ^*, solve (2.27) for M^*; use (2.24) to compute u_g and v_g; use these geostrophic winds in (2.22) to predict a new σ^*.

The system (2.22), (2.24) and (2.27) is more general than it might appear at first sight. To see this, we adopt an idea which has proved useful in such contexts as the definition of available potential energy (Lorenz, 1955), the analysis of baroclinic instability (Bretherton, 1966; Hoskins et al., 1985), and the finite amplitude Eliassen-Palm theorem (Andrews, 1983). The idea involves what happens when an isentropic surface intersects the earth's surface. We can regard such an isentrope as continuing just under the earth's surface with a pressure equal to the surface pressure. At any horizontal position where two distinct isentropic surfaces run just under the earth's surface (and hence have the same pressure), there is no mass trapped between them, so that $\sigma^*=\sigma=0$ there. We can regard the Θ_B in (2.27c) as the largest value of Θ which remains everywhere below the earth's surface. Thus, we can use (2.22) to predict σ^* and (2.27) to diagnose M^* on all Θ surfaces such that $\Theta>\Theta_B$. This procedure is consistent with Bretherton's (1966) conclusion that "any flow with potential temperature variations over a horizontal rigid plane boundary may be considered equivalent to a flow without such variations, but with a concentration of potential vorticity very close to the boundary." We have simply replaced Bretherton's

thin sheet of infinite potential vorticity with a thin sheet of zero potential pseudo-densit and chosen to predict the evolution of the entire σ^* field (including this zero potentia pseudo-density region) with (2.22).

2.1.3 Two-dimensional response to a moving heat source

A simplification of equations (2.20) and (2.27) to two dimensions will be considered To simulate an infinitely long moving heat source, it will be assumed that $\partial/\partial y = \partial/\partial Y =$ 0, so that $u = u_a$ (i.e., $u_g = 0$) and $v = v_g$ (i.e., $v_a = 0$). Equation (2.20) then reduces t

$$\frac{\partial \sigma^*}{\partial T} + \frac{\partial}{\partial \Theta}\left(\dot{\theta}\sigma^*\right) = 0, \tag{2.28}$$

and (2.27) reduces to

$$\frac{1}{f^2}\left[\left(f^2 - \frac{\partial^2 M^*}{\partial X^2}\right)\frac{\partial^2 M^*}{\partial \Theta^2} + \left(\frac{\partial^2 M^*}{\partial X \partial \Theta}\right)^2\right] + \Gamma\sigma^* = 0, \tag{2.29a}$$

$$\frac{\partial M^*}{\partial \Theta} = \Pi_T \qquad \text{at} \qquad \Theta = \Theta_T, \tag{2.29b}$$

$$\Theta\frac{\partial M^*}{\partial \Theta} - M^* + \frac{1}{2f^2}\left(\frac{\partial M^*}{\partial X}\right)^2 = 0 \qquad \text{at} \qquad \Theta = \Theta_B. \tag{2.29c}$$

Equations (2.28) and (2.29) along with (2.24) form the closed system in two dimen sions. Using (2.28) a σ^* field is predicted over the entire domain. This predicted fiel is then applied to (2.29) and an associated M^* field is diagnosed using an iterative tech nique. Finally, (2.24) is used to obtain information about the wind and mass fields fron the diagnosed M^* field.

The two dimensions (X, Θ) are chosen such that X is the direction across the moving heat source. Thus the structure in the direction along the heat source is assumed to be uniform so that many of the physically interesting features can be studied by examining the structure across it. Mathematically the two-dimensional study has advantages for two reasons. First, comparing the two-dimensional invertibility equation (2.29) with the three-dimensional invertibility equation (2.27), it can easily be seen that (2.29) will be computationally much simpler. Second, the invertibility principle must be applied at each time step in the three-dimensional case because the predictive equation for σ^* (2.20) depends on the geostrophic flow at each time step, which must be diagnosed from M^*.

In the case of two-dimensions the predictive equation (2.28) has no dependence on the geostrophic flow and therefore the invertibility principle must be applied only once, after the time integration is complete.

Since the M^* field contains information about the wind and mass fields through the thermal wind relation, M^* diagnosed after the final time step will provide insight into the geostrophic flow and vertical structure through (2.24). The component of the geostrophic wind along the moving heat source is given by v_g; this component can be determined from $\partial M^*/\partial X$ over the domain. Since $\partial/\partial Y = 0$ for the two-dimensional case, the component of the geostrophic wind across the heat source, u_g, is zero by assumption. However, using the v-momentum equation (2.2) the ageostrophic component across the moving heat source can be derived. The vertical structure is represented by the Exner function Π and is related to M^* through $\partial M^*/\partial\Theta$.

The moving heat source to be considered is a mid-latitude squall line. As a simple parameterization of the squall line a steady state heating given by

$$\dot{\theta}(X,\Theta,T) = \begin{cases} 0 & T < 0 \\ Q_0 \exp\left[-\frac{(X-cT)^2}{X_0^2}\right] \sin\left[\frac{\pi(\Theta-\Theta_B)}{\Theta_T-\Theta_B}\right] & T > 0 \end{cases}, \tag{2.30}$$

will be considered. Here Q_0 is the heating rate, c is the eastward X-space propagation speed and X_0 is the e-folding half width of the squall line. Horizontal structure is Gaussian, given by the exponential term and the vertical structure is represented by a sine function, giving maximum heating in the middle of the troposphere.

An important parameter to be used in the derivation of a dimensionless form of the predictive equation for σ^* is given by

$$\alpha = \frac{(\Theta_T - \Theta_B)/(\pi Q_0)}{X_0/c}. \tag{2.31}$$

This dimensionless parameter can be regarded as the ratio of mesoscale convective overturning time to the squall line passage time. Squall lines of differing characteristics can then be simulated by varying α. For instance, α is small for intensely raining, wide, slowly moving squall lines while it is large for weakly raining, narrow, fast moving squall lines. Results of several experiments using differing values of X_0, Q_0 and c will be described in Section 2.3.

An analytical solution to (2.28) is derived as follows. Substituting (2.31) in (2.28) w obtain

$$\alpha e^{\tau^2} \frac{\partial}{\partial \tau} (\sigma^* \sin Z) + \sin Z \frac{\partial}{\partial Z} (\sigma^* \sin Z) = 0, \tag{2.32}$$

where $Z = \pi(\Theta - \Theta_B)/(\Theta_T - \Theta_B)$ and $\tau = (cT - X)/X_0$. According to (2.32) the quantit $\sigma^* \sin Z$ is constant along each characteristic curve determined from

$$\frac{d\tau}{\alpha e^{\tau^2}} = \frac{dZ}{\sin Z}. \tag{2.33}$$

By integration of (2.33) we can show that the characteristic through the point $(X, Z, T$ approaches (in the far field) the level

$$Z_0(X, Z, T) = 2 \tan^{-1} \left(e^{-\beta(X,T)} \tan \frac{Z}{2} \right), \tag{2.34}$$

where

$$\beta(X, T) = \frac{\sqrt{\pi}}{2\alpha} \left[\text{erf} \left(\frac{cT - X}{X_0} \right) + \text{erf} \left(\frac{X}{X_0} \right) \right] \tag{2.35}$$

These characteristic curves are shown in Fig. 2.1. Let us assume that as $X \to \pm\infty$, σ approaches the constant σ_0. Since $\sigma^* \sin Z$ is constant along each characteristic, we car write the solution of (2.28) as

$$\sigma^*(X, Z, T) = \sigma_0 \frac{\sin Z_0(X, Z, T)}{\sin Z}. \tag{2.36a}$$

Although (2.36a) is indeterminate at the top and bottom boundaries, use of L'Hopital's rule yields

$$\sigma^*(X, Z, T) = \sigma_0 \begin{cases} e^{\beta(X,T)} & Z = \pi \\ e^{-\beta(X,T)} & Z = 0 \end{cases}. \tag{2.36b}$$

Equation (2.36) becomes the predictive equation for σ^* in the two-dimensional case.

Reduction of the original three-dimensional problem to one in two-dimensions allows for the use of a simple iterative technique to solve (2.29). This equation can be further simplified by isolating the dynamically significant part of M^* given by the deviation Bernoulli field $\mathcal{M} = M^* - \bar{M}^*$ where

$$\bar{M}^* = c_p \Theta_B + c_p p_0 \sigma_0^{-1} (1 + \kappa)^{-1} \left[1 - (\bar{p}/p_0)^{1+\kappa} \right] \tag{2.37a}$$

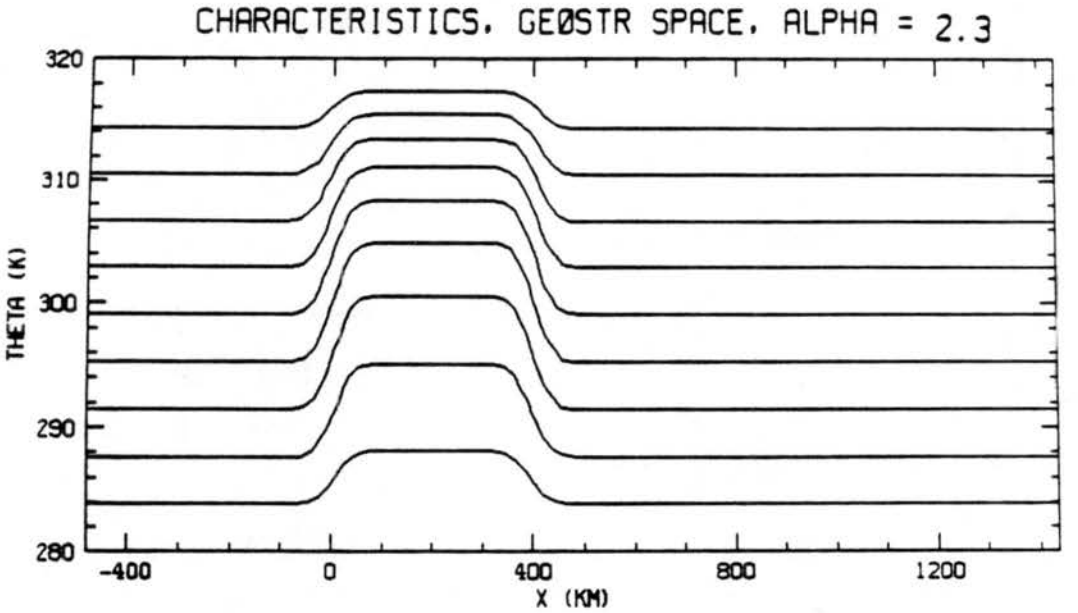

Figure 2.1: Characteristic curves $Z(X, Z_0, T)$ as given by the rearrangement of (2.34) for $T = 8$ hr. According to (2.32) the quantity $\sigma^* \sin Z$ is constant along each characteristic. The diagram is in (X, Θ) space for $\Theta_T - \Theta_B = 40$ K, $Q_0 = 7$ K hr^{-1}, $X_0 = 40$ km, and $c = 50$ km hr^{-1}, all of which result in $\alpha = 2.3$.

is the horizontally uniform basic state Bernoulli field and

$$\bar{p} = p_T + \sigma_0 (\Theta_T - \Theta) \tag{2.37b}$$

is the horizontally uniform basic state pressure. From (2.37b) we can also define

$$\bar{\Gamma} = \frac{R}{p_0} \left(\frac{\bar{p}}{p_0} \right)^{\kappa - 1}, \tag{2.37c}$$

Using (2.29) it can easily be shown that $\mathcal{M}$ satisfies

$$\left(f^2 - \frac{\partial^2 \mathcal{M}}{\partial X^2} \right) \left(\bar{\Gamma} \sigma_0 - \frac{\partial^2 \mathcal{M}}{\partial \Theta^2} \right) - \left(\frac{\partial^2 \mathcal{M}}{\partial X \partial \Theta} \right)^2 = f^2 \Gamma \sigma^* \tag{2.38a}$$

$$\frac{\partial \mathcal{M}}{\partial \Theta} = 0 \qquad \text{at} \qquad \Theta = \Theta_T \tag{2.38b}$$

$$\Theta \frac{\partial \mathcal{M}}{\partial \Theta} - \mathcal{M} + \frac{1}{2f^2} \left(\frac{\partial \mathcal{M}}{\partial X} \right)^2 = 0 \qquad \text{at} \qquad \Theta = \Theta_B. \tag{2.38c}$$

Lateral boundary conditions are obtained by noting that $\sigma^* \to \sigma_0$ in the far field and assuming that the far field solution is horizontally homogeneous we also have $M^* \to \bar{M}^*$. Thus we use the Dirichlet lateral boundary condition $\mathcal{M} = 0$. From (2.38) $\mathcal{M}$ is solved iteratively, M^* is then easily calculated and using (2.24) mass and wind fields can be diagnosed. Details of numerical methods applied will be discussed in Section 2.2.

2.2 Numerical procedure

2.2.1 General description

The discussion begins by assuming that a solution for σ^* has been obtained from (2.36). The two-dimensional $X - \Theta$ domain is defined vertically by 32 grid intervals with $\Theta_B = 280$ K at the lower boundary and $\Theta_T = 320$ K at the upper boundary for a vertical increment $\Delta\Theta = 1.25$ K. Initial test runs were made with an idealized linear tropospheric stability profile with pressure defined from $p_0 = 1000$ mb to $p_T = 200$ mb, yielding a constant $\sigma_0 = 20$ mb K^{-1}. In Section 2.3, experiments are described in which a stratosphere was added along with a more physically realistic stability profile.

In order for the solution in the interior of the domain to remain unaffected by the lateral boundaries, the horizontal domain had to be of a large enough size. This was determined experimentally to be six Rossby lengths with one Rossby length λ defined by

$$\lambda = \frac{(\Theta_T - \Theta_B)}{f} \sqrt{\frac{(R_d/p_0)(p_0 - p_T)}{(\Theta_T - \Theta_B)}}$$

where $R_d = 287$ J K^{-1} kg^{-1} is the dry air gas constant and $f = 10^{-4}$ s^{-1} is the coriolis parameter. Use of these values results in $\lambda = 958$ km. An increment in X is defined by $\Delta X = [\lambda/(\Theta_T - \Theta_B)]\Delta\Theta = 29.9$ km. In the horizontal 192 grid intervals were used from $X = -1437$ km to $X = 4311$ km.

In the interior of the domain, using centered second-order finite differences, $\mathcal{M}_{i,k}$ can be defined as the numerical approximation to (2.38a) by

$$(\mathcal{M}_{i,k} - a_{i,k})(\mathcal{M}_{i,k} - b_{i,k}) = c_{i,k} \tag{2.39a}$$

where

$$a_{i,k} = \frac{1}{2}\left[\mathcal{M}_{i+1,k} + \mathcal{M}_{i-1,k} - (f\Delta X)^2\right]$$

$$b_{i,k} = \frac{1}{2}\left[\mathcal{M}_{i,k+1} + \mathcal{M}_{i,k-1} - \bar{\Gamma}_k\sigma_0(\Delta\Theta)^2\right]$$

$$c_{i,k} = \frac{(\Delta X\Delta\Theta)^2}{4}\left[f^2\Gamma_{i,k}\sigma_{i,k}{}^* + d_{i,k}{}^2\right]$$

$$d_{i,k} = \frac{1}{4\Delta X\Delta\Theta}\left[\mathcal{M}_{i+1,k+1} - \mathcal{M}_{i-1,k+1} - \mathcal{M}_{i+1,k+1} + \mathcal{M}_{i-1,k-1}\right]$$

and where i and k are the horizontal and vertical indices respectively.

To enable use of second-order finite differencing on the vertical boundaries, ghost points are needed. These are obtained by finite difference versions of (2.38b) and (2.38c), i.e.,

$$\mathcal{M}_{i,nz+1} = \mathcal{M}_{i,nz-1} \tag{2.39b}$$

at the upper ghost point and

$$\mathcal{M}_{i,-1} = \mathcal{M}_{i,1} - \frac{2\Delta\Theta}{\Theta_0}\left[\mathcal{M}_{i,0} - \frac{1}{2f^2}\left(\frac{\mathcal{M}_{i+1,0} - \mathcal{M}_{i-1,0}}{2\Delta X}\right)^2\right] \tag{2.39c}$$

at the lower ghost point, where the vertical domain is defined by $k = (0, 1, ..., nz-1, nz)$ with $nz = 32$, so that the indices -1 and $nz + 1$ represent the lower and upper ghost points respectively.

As discussed in the previous section, the lateral boundaries are set using the Dirichlet condition $\mathcal{M} = 0$ at both the left and right hand boundaries. Since the far field solution is assumed horizontally homogeneous, the same Dirichlet condition is applied at the vertical ghost points on the lateral boundaries.

2.2.2 Invertibility using Gauss-Seidel (GS) relaxation

The invertibility was first solved numerically using a simple Gauss-Seidel techniqu with no over-relaxation. The procedure begins by calculating the horizontally uniform basic state fields $\bar{M}^*, \bar{p}$ and $\bar{\Gamma}$. An initial guess is next made over the entire domain which for simplicity we set as $\mathcal{M}_{i,k} = 0$ for $i = (0, 1, ..., nx-1, nx)$ where $nx = 192$ and $k = (-1, 0, ..., nz, nz+1)$. To satisfy the lateral boundary conditions, $\mathcal{M}$ at the boundaries (i.e., $\mathcal{M}_{0,k}$ and $\mathcal{M}_{nx,k}$) did not change during the course of the iterations.

The following steps were repeated until a specified tolerance (to be discussed later) has been met:

1. Calculate vertical ghost points along the horizontal domain except at the lateral boundaries using (2.39b) and (2.39c).

2. Update $\Gamma = \kappa\Pi/p$ for all interior points as well as vertical boundaries. Recall that Π can be obtained from a finite difference approximation to (2.24). To reduce the number of computations, the approximation $\Gamma = \bar{\Gamma}$ is used for the first 100 iterations and Γ is only updated every 10 iterations thereafter.

3. Calculate the coefficients $a_{i,k}, b_{i,k}, c_{i,k}$ and $d_{i,k}$ in (2.39a) at all interior points and the vertical boundaries.

4. Calculate a residual at each interior point from (2.39a) using $R_{i,k} = (\mathcal{M}_{i,k} - a_{i,k})(\mathcal{M}_{i,k} - b_{i,k}) - c_{i,k}$. From this array a residual norm RN is calculated

$$RN = \sqrt{\sum \frac{R_{i,k}{}^2}{N}} \tag{2.40}$$

   where N is the number of grid points in the interior.

5. Update $\mathcal{M}_{i,k}$ at all interior points using the quadratic formula applied to (2.39a), i.e.,

$$\mathcal{M}_{j,k} = \frac{1}{2}\left\{a_{j,k} + b_{j,k} + \left[(a_{j,k} - b_{j,k})^2 + 4c_{j,k}\right]^{\frac{1}{2}}\right\}.$$

6. Return to Step 1.

These steps were repeated until either RN was less than the specified tolerance or a specified maximum number of iterations was reached. If the maximum number of iterations was reached, RN at that iteration was also printed out as a guideline for future runs.

In order to check the efficiency of this scheme, the ratio of RN at the current iteration to RN at the previous iteration was calculated. A ratio of 0.5 is considered fast convergence, whereas 0.9 or greater is considered slow convergence. A ratio of 1.0 or greater indicates that the scheme is actually diverging. The Gauss-Seidel scheme described above converged very slowly; normally after about 100 iterations RN ratios were on the order of 0.999.

The tolerance was set to be the RN computed using (2.40) but applied to the final solution of M as obtained by the multigrid method (to be discussed in the next subsection). For most test runs, the Gauss-Seidel scheme required on the order of 1000 to 2000 iterations to converge, depending on the parameters describing the simulated squall line (e.g., X_0, c, Q_0).

2.2.3 Invertibility using a full multigrid (FMG) method

A second and more efficient method for solving the invertibility involved a full multigrid method. The basic idea in a multigrid method is to approximate the problem on a set of grids of varying mesh sizes, cycling between the grids to produce a solution on the finest grid with optimal efficiency. The multigrid method used here featured nonlinear Gauss-Seidel relaxation as a smoother, full weighting of residuals, bilinear interpolation of corrections, and a full multigrid (FMG) control structure with bicubic FMG interpolation. An advantage of the FMG method is that it generates an approximation to the truncation error (truncation error is that obtained by using the continuous solution in the discrete equations). This feature is quite useful in that the problem can be solved to this level of accuracy and unnecessary computational work is thus avoided. A detailed description of this multigrid method is given in Fulton (1988).

For a more general description of multigrid methods, a review is found in Fulton et al. (1986) with a specific application to tropical cyclones described in Ciesielski et al. (1986).

2.2.4 Diagnosing physical fields and transforming to physical space

The component of the geostrophic flow along the squall line v_g was easily calculate using a finite difference approximation to (2.24). Since $M^*(X,\Theta) = \bar{M}^*(\Theta) + \mathcal{M}(X,\Theta)$ w have

$$fv_g = \frac{\partial M^*}{\partial X} = \frac{\partial \mathcal{M}}{\partial X}$$

or in finite difference form

$$fv_{g_{i,k}} = \frac{\mathcal{M}_{i+1,k} - \mathcal{M}_{i-1,k}}{2\Delta X}$$

for $i = 1, 2, ..., nx - 1$ and $k = 0, 1, ..., nz$.

Pressure p was obtained from (2.24) and the definition of the Exner function

$$\Pi = \frac{\partial M^*}{\partial \Theta} = c_p \left(\frac{p}{p_0}\right)^{\kappa}.$$

Solving for p and using finite differences gives

$$p_{i,k} = p_0 \left[\frac{1}{c_p} \frac{M^*_{i,k+1} - M^*_{i,k-1}}{2\Delta\Theta}\right]^{1/\kappa}.$$

Once the geostrophic flow was obtained over the entire domain, the relation betwee x and X could be found from (2.5), i.e., $x = X - v_g/f$. At each vertical level a splin was fit to the variable to be transformed (e.g., p) using x as the abscissa. The spline wa then simply evaluated for the variable at each X at the given vertical level, resulting in a representation of the variable in physical space.

2.3 Numerical experiments and results

2.3.1 General model results

We begin with a specific sample case (i.e., a specific simulation time and α) and describe the major features predicted by the model. For this purpose a representative case was chosen using the Gauss-Seidel method applied to the invertibility. The sample case is an 8 hr simulation with typical parameters $c = 50$ km hr^{-1}, $Q_0 = 7$ K hr^{-1} and $X_0 = 40$ km which are indicated by two case studies of Oklahoma squall lines by Ogura and Chen (1977) and Ogura and Liou (1980). These parameters yield $\alpha = 2.3$ and correspond to the characteristic curves in Fig. 2.1.

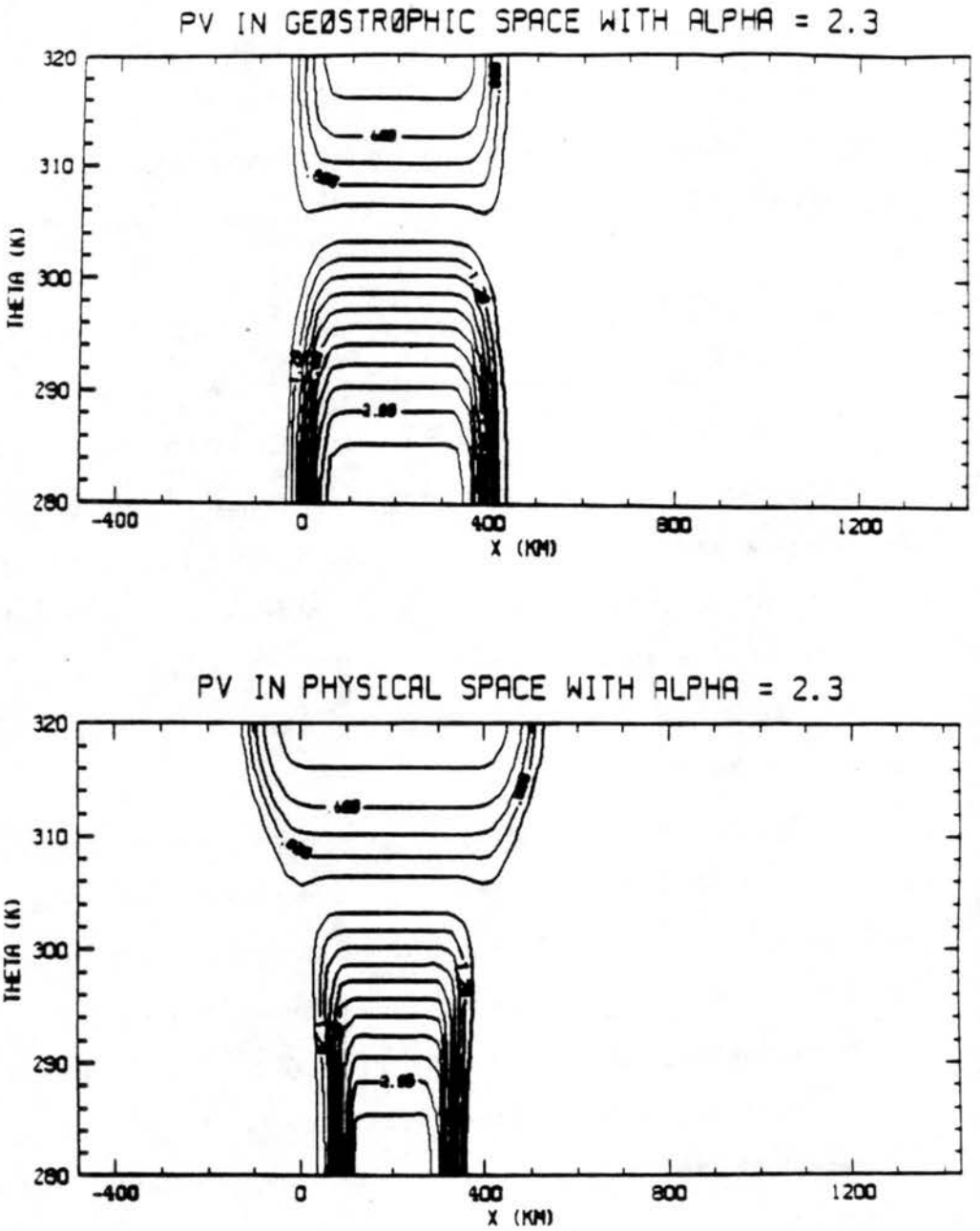

Figure 2.2: Isolines of $q = \sigma_0/\sigma^*$ (i.e., potential vorticity measured in units of f) for $T = 8$ hr and $\alpha = 2.3$ in (a) geostrophic space and (b) physical space. The squall line generates a lower tropospheric region of high q and an upper tropospheric region of low q. Note the effect of the coordinate transform from geostrophic to physical space; regions of cyclonic shear have been tightened and regions of anticyclonic shear have been broadened.

Figure 2.2a shows the potential vorticity $q = \sigma_0/\sigma^*$ field for this case in geostrophi space. Values of q have been non-dimensionalized by σ_0 (i.e., potential vorticity is mea sured in units of f) so that $q = 1$ represents the initial undisturbed field. The squall lin was assumed to have started instantaneously at $X = 0$ km and has propagated along th domain for 8 hours at a speed c. Thus the leading edge of the squall line is located a $X = 400$ km. In its wake the squall line has left a region of high q in the lower troposphere with a maximum of 2.1 and a region of low q in the upper troposphere with a minimum of 0.5.

In Fig. 2.2b the effects of the coordinate transform from geostrophic to physical spac according to (2.5) become apparent. Regions of cyclonic shear (corresponding to regions o high q) have been tightened and regions of anticyclonic shear (corresponding to regions o low q) have been broadened. From these figures an advantage of performing computation in geostrophic space is demonstrated. In geostrophic space, regions of greatest cyclonic shear are resolved by more grid points than corresponding regions in physical space while maintaining the same grid resolution (Hoskins, 1975). A more dramatic example of the coordinate transformation can be seen when the theory is applied to tropical cyclones (Schubert and Alworth, 1987).

As the perturbation q field develops, a corresponding $\mathcal{M}$ field develops (Fig. 2.3a) Negative values of $\mathcal{M}$ occur in the lower troposphere while positive values occur in the upper troposphere. Magnitudes of the positive and negative fields differ by approximately 150 $m^2\ s^{-2}$, the positive field being greater. This asymmetry is due in part to the effect of Γ (which increases with decreasing pressure) in (2.38a). Regions in which the magnitude of the $\mathcal{M}$ field is greatest correspond to regions of the greatest q anomaly.

Horizontal and vertical gradients in the $\mathcal{M}$ field are of greater importance than the magnitudes of these fields. From (2.24) the geostrophic wind field along the squall line v_g as shown in Fig. 2.3b can be anticipated. In the lower troposphere, the positive q anomaly (and associated negative $\mathcal{M}$ field) causes cyclonic shear with positive v_g at the current squall line position and negative v_g at the start-up position. In those lower tropospheric regions where q is unmodified, the horizontal wind shear is anticyclonic. In the upper

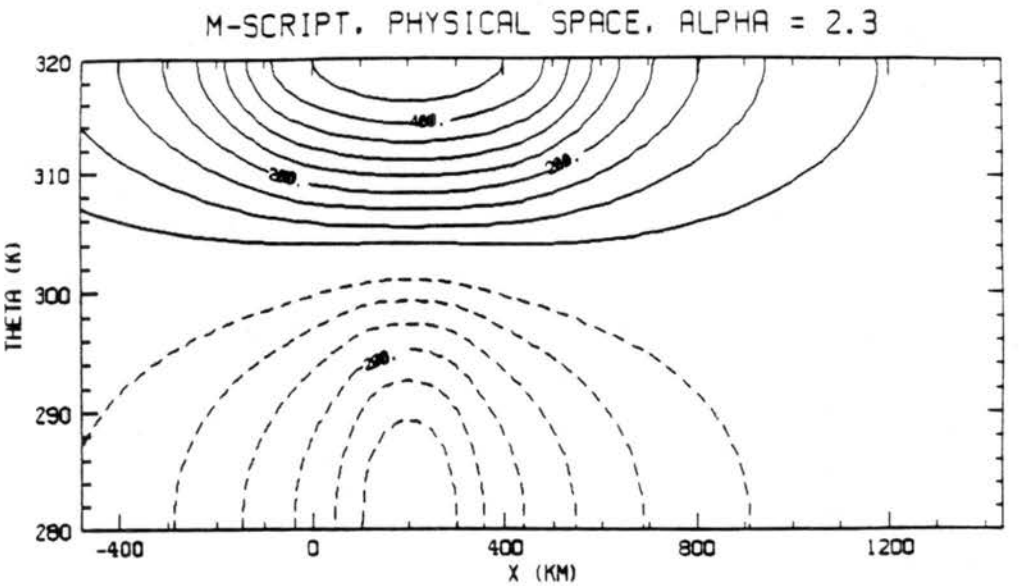

(a)

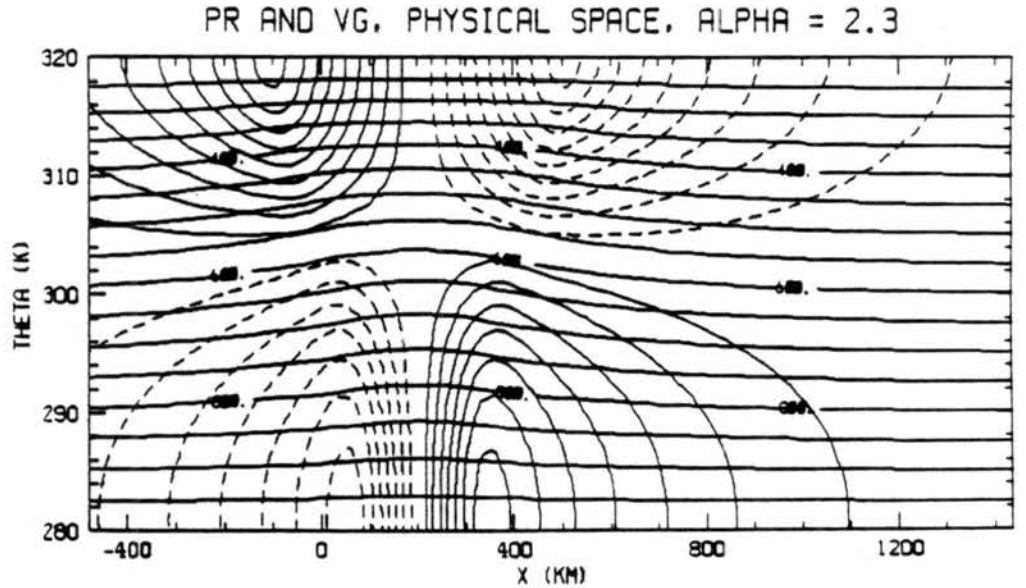

(b)

Figure 2.3: (a) $\mathcal{M}$ field resulting from applying the invertibility (2.29) to the q field in Fig. 2.2. $\mathcal{M}$ has units m^2s^{-2}. Use of the definition of the deviation Bernoulli field and (2.24) result in the mass and wind fields shown in (b). Pressure (nearly horizontal lines) are in millibars. Solid contours indicate flow into the page, dashed contours indicate flow out of the page; contour interval is 1 ms^{-1}.

troposphere the geostrophic flow is reversed because the negative q anomaly there induces anticyclonic shear. A maximum geostrophic flow of 7 ms^{-1} at lower levels and 9 ms^{-1} at upper levels has been generated by the squall line.

Also shown in Fig. 2.3b is the distortion of the pressure field due to the squall line passage. Behind the squall line there has been a decrease of σ (i.e., pressure lines are further apart indicating stabilization) in the lower troposphere and an increase of σ (destabilization) in the upper troposphere. Since q is a combination of the mass and wind fields, this is simply a reflection of the mutual adjustment of those fields. This adjustment occurs in such a way that in the lower troposphere where q is large, ς is large and σ is small whereas in the upper troposphere where q is small, ς is small and σ is large. The destabilization of the upper troposphere may play a role in the maintenance of the stratiform rain region that is often observed in the wake of both tropical (Gamache and Houze, 1982, 1983) and midlatitude squall lines (Ogura and Liou, 1980). The region of maximum destabilization in Fig. 2.3b is displaced behind the squall line; observationally this is in rough agreement with the relative position of the upper level mesoscale updraft associated with the stratiform rain region. Although this model does not capture the complicated moist physics occurring in the stratiform region, it is possible that the upper level destabilization does form a favorable background state for this mesoscale feature. Other possible mechanisms are discussed in Johnson and Houze (1987).

Results of a 16 hr simulation are found in Figs. 2.4a and b. The q anomaly has increased in horizontal extent but not in magnitude. Note that the q anomaly does not extend over a range of 800 km (i.e., 16 hr $\times$ 50 km hr^{-1}). This is due to the fact that the squall line propagated at c in geostrophic space; the results presented have been transformed to physical space. By $T = 16$ hr the squall line has propagated over nearly one Rossby length so that there occurs less cancellation between the flows induced by the edges of the q anomaly. Accordingly, the maximum lower and upper level geostrophic flows have increased to 10 and 12 ms^{-1} respectively and the horizontal extent of induced winds have increased by several hundred kilometers (Fig. 2.4b).

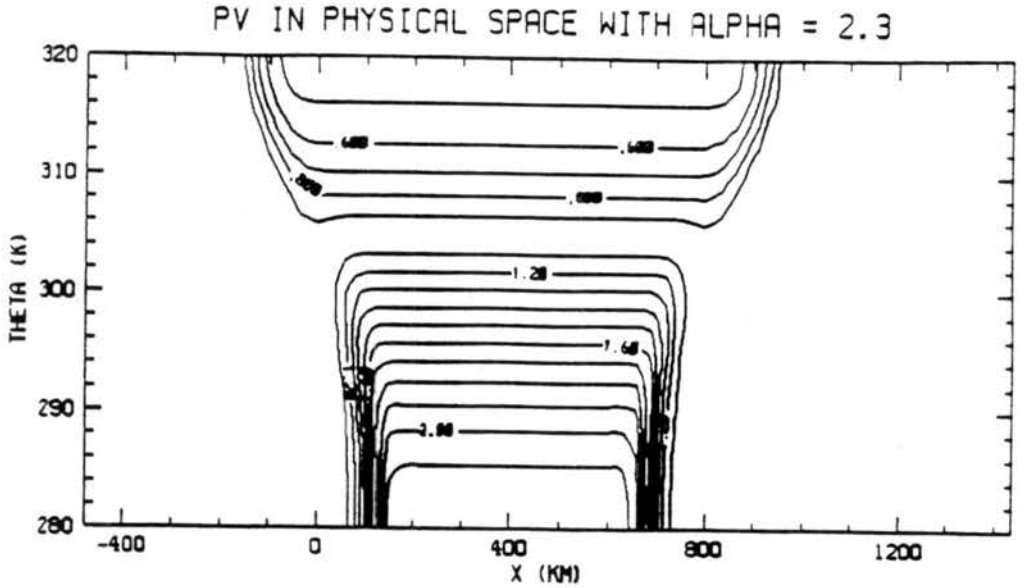

(a)

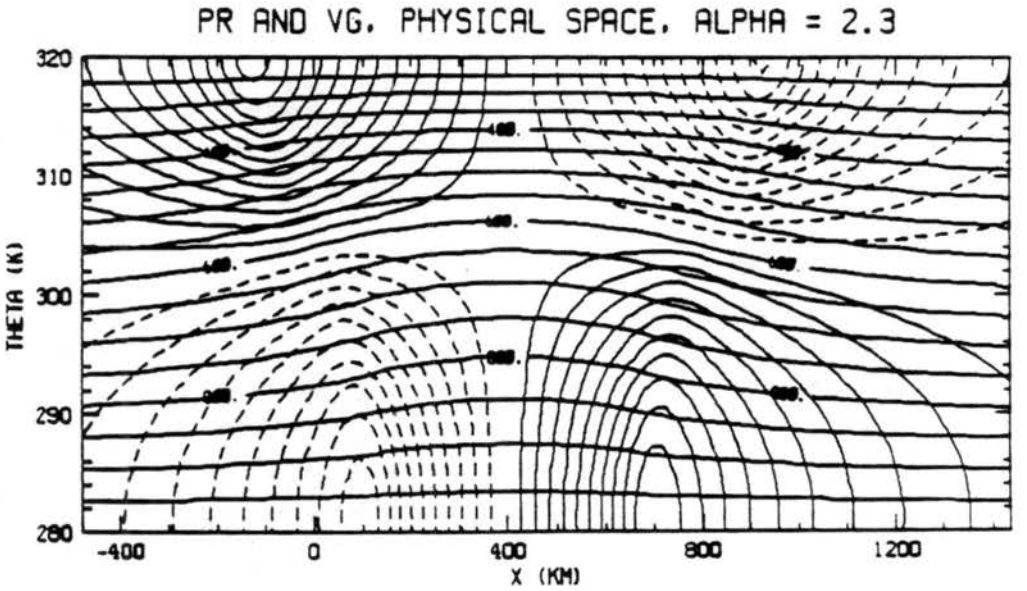

(b)

Figure 2.4: Potential vorticity (a) and pressure and wind fields (b) for $T = 16$ hr and $\alpha = 2.3$. q has been nondimensionalized as in Fig. 2.2; pressure and wind fields have the same contour values as Fig. 2.3.

2.3.2 Comparison of the FMG and GS methods to solve the invertibility

As a check of the solution to the invertibility principle, the solutions obtained fron the FMG and GS methods were compared to each other. The sample case described in th previous section, as well as other cases run using the FMG scheme (e.g., using differen times and values of α), were re-run to the same convergence tolerance as the GS method The results obtained by the GS method were identical to those obtained by the FMC method, adding confidence that both schemes were converging to the correct solution.

Also of interest was an efficiency comparison between the two methods; the FMC scheme should be noticeably more efficient than the GS scheme. For this comparisor the FMG method was first allowed to converge to its internally generated approximat truncation error; this level of accuracy was then used as the convergence tolerance for th GS method. Results of the comparison for a variety of grid sizes is shown in Table 2.1.

TABLE 2.1. Efficiencies for the GS and FMG methods in terms of CRAY XMP execution time (in sec) per grid point for five cases using different numbers of grid points.

Number of grid points			GS iterations	Execution time (sec) per grid point		Ratio of execution time
nx	nz	nx × nz		GS	FMG	GS/FMG
32	64	2048	2104	1.365 (-3)	7.173 (-5)	19.0
32	128	4096	4137	2.686 (-3)	6.045 (-5)	44.4
32	192	6144	6775	4.373 (-3)	5.781 (-5)	75.6
32	256	8192	7696	4.951 (-3)	5.620 (-5)	88.1
64	256	16384	12720	7.052 (-3)	5.550 (-5)	127.1

As the resolution increases, the number of GS iterations required for convergence increases roughly by one iteration for each grid point. The execution time per grid point for the GS scheme increases as the grid resolution increases, consistent with the theoretical asymptotic convergence rate, $1 - O(h)$, where h represents the mesh spacing. On the other hand, as

the resolution increases in the FMG runs, the execution time per grid point decreases. The advantage of the FMG method over GS is clearly illustrated in the last column of Table 2.1, which gives the ratio of the GS execution time per grid to FMG execution time per grid. The GS method required more execution time by factors ranging from 19 to 127. The trend in these ratios is in agreement with experiments performed by Ciesielski et al. (1986, their Table 1); ratios here are much larger because no over-relaxation was used in the GS scheme for these experiments.

The importance of the FMG method's greater efficiency becomes more apparent when considering invertibility in the full 3-D case. In the 2-D case equation (2.29) must be solved only once, after the completion of the time integration. However in the 3-D case, the more complex equation (2.27) must be solved at every time step. Thus in the 3-D case the efficiency becomes an advantage many times over and may even be essential to solve this type of problem especially given limited computer resources.

2.3.3 Further model experiments

In this section experiments are described in which the squall line parameters (i.e., X_0, c, Q_0) were varied from the previously described sample case. These experiments were performed to further test the model output as well as to study the physical effect of each parameter on the squall line. Only one parameter was changed for each experiment; although some experiments produced the same α, the resulting physical features were not necessarily the same. All experiments described are 8 hr simulations using the FMG method to solve the invertibility for M.

In the first experiment the half width X_0 is varied. Figure 2.5a shows the resulting q field for the case $X_0 = 20$ km, giving $\alpha = 4.6$. Although the shape is similar to that of Fig. 2.2b ($\alpha = 2.3$), the magnitudes are much smaller. Also of note is the fact that the lower troposphere q anomaly does not extend as far vertically for this narrower squall line. As can be seen in Fig. 2.5b the corresponding geostrophic wind fields are weaker by 3 to 4 ms^{-1} than the wider ($X_0 = 40$ km) squall line, with weaker pressure perturbations.

When the half width is doubled from $X_0 = 40$ km to $X_0 = 80$ km, giving $\alpha = 1.15$, the opposite effect is seen. The perturbation q field is much stronger and the lower

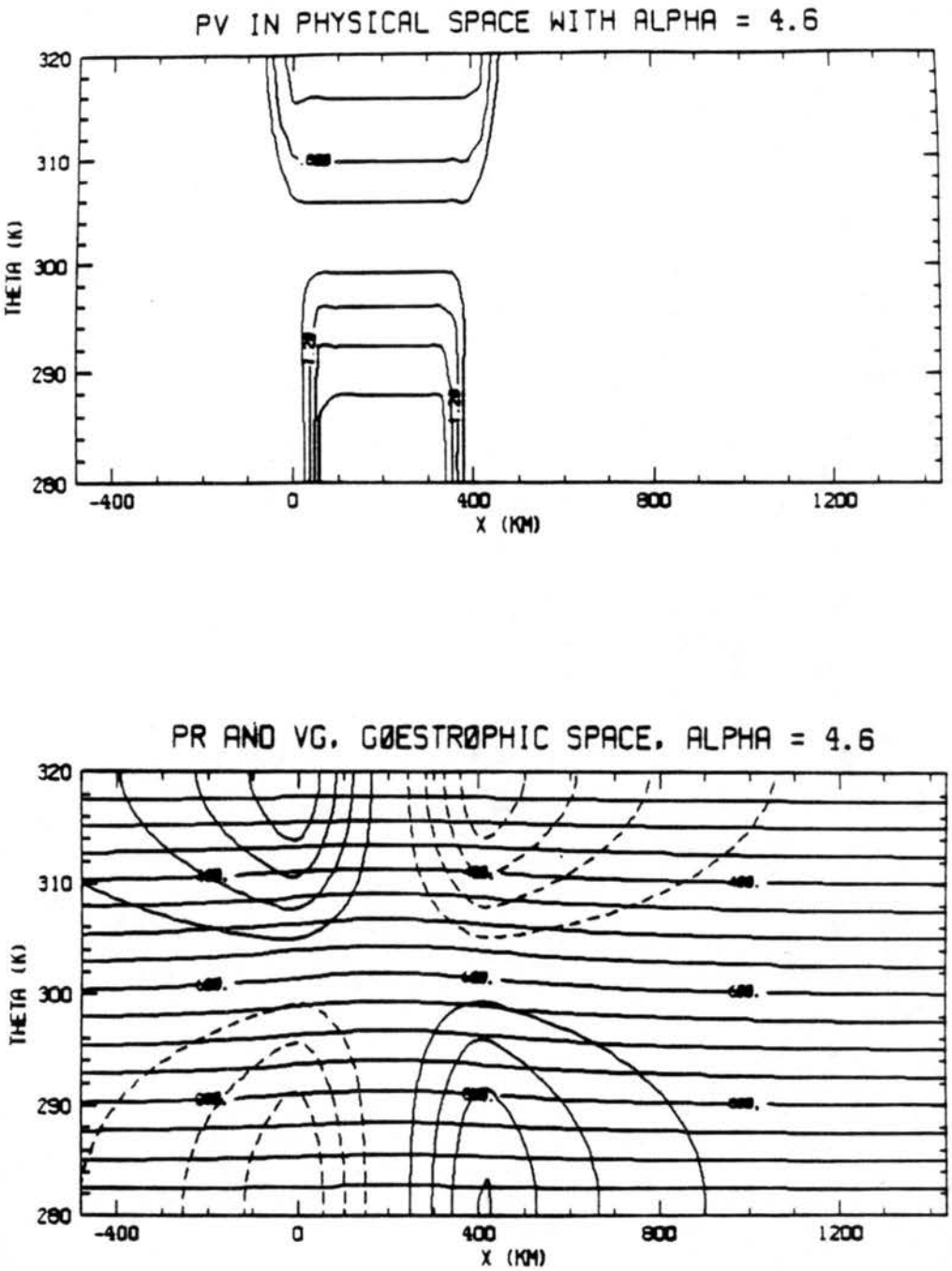

Figure 2.5: Potential vorticity (a) and pressure and wind fields (b) for $T = 8$ hr, $Q_0 = 7$ K hr^{-1}, $X_0 = 20$ km, and $c = 50$ km hr^{-1}, resulting in $\alpha = 4.6$. Contour values as in Fig. 2.4.

troposphere q anomaly extends higher into the troposphere (Fig.2.6a), since with the wider squall line the heating rate Q_0 has had more time to effect q. Induced geostrophic winds have increased to a maximum of 12 ms^{-1} at lower levels and a minimum of -16 ms^{-1} at upper levels. The pressure field also shows an increased perturbation. Thus, as expected, the simulations show that a wider squall line will have a greater effect on the ambient atmosphere.

From this first experiment we can see that the penetration depth of the q anomaly due to the squall line depends on α. Referring to the definition of α and (2.30) we see that the factors which lead to a decrease in α (e.g., increase X_0) lead to an increase in the heating function $\dot{\theta}$. If we rewrite (2.28) in the form

$$\frac{\partial \sigma^*}{\partial T} + \dot{\theta}\frac{\partial \sigma^*}{\partial \Theta} = -\sigma^* \frac{\partial \dot{\theta}}{\partial \Theta}$$

we see that increasing the vertical derivative of $\dot{\theta}$ causes a decrease in σ^* at lower levels and an increase in σ^* at upper levels (because from (2.30) $\dot{\theta}$ is proportional to $\sin(\Theta/\Delta\Theta)$. Since q is simply the inverse of σ^*, we have high q anomalies at lower levels and low q anomalies at upper levels. This agrees with physical intuition; stronger squall lines would be expected to penetrate farther vertically. The experiments also suggests that α may be a useful parameter in classifying the strength of squall lines.

The second experiment simulated squall lines with different heating rates Q_0. In Fig. 2.7a the effects of reducing Q_0 by half from 7 K hr^{-1} to 3.5 K hr^{-1} can be seen. This case also gives $\alpha = 4.6$ the same as the case $X_0 = 20$ km; the q field has the same shape and magnitude. Careful comparison of Figs. 2.5a and 2.7a shows that the latter has a weaker horizontal q gradient. Since v_g depends on the X derivative of the perturbation, a weaker flow would be expected and is seen in Fig. 2.7b, especially in the lower troposphere positive v_g. Although a 1 ms^{-1} difference may not be physically very significant, these results add confidence in the model behavior.

Figure 2.8a shows the q field for $Q_0 = 14$ K hr^{-1}, giving $\alpha = 1.1$. This case is again similar to the previous $\alpha = 1.1$ case but here the horizontal gradients are stronger and slightly stronger geostrophic flows (Fig.2.8b) are produced. The model thus predicts a physically realistic increased atmospheric response with increasing Q_0.

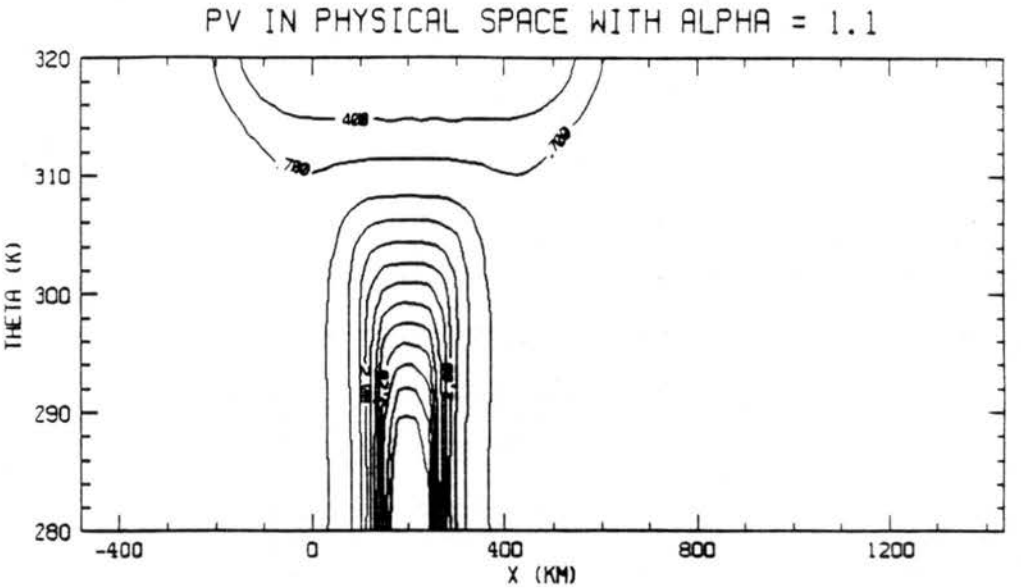

(a)

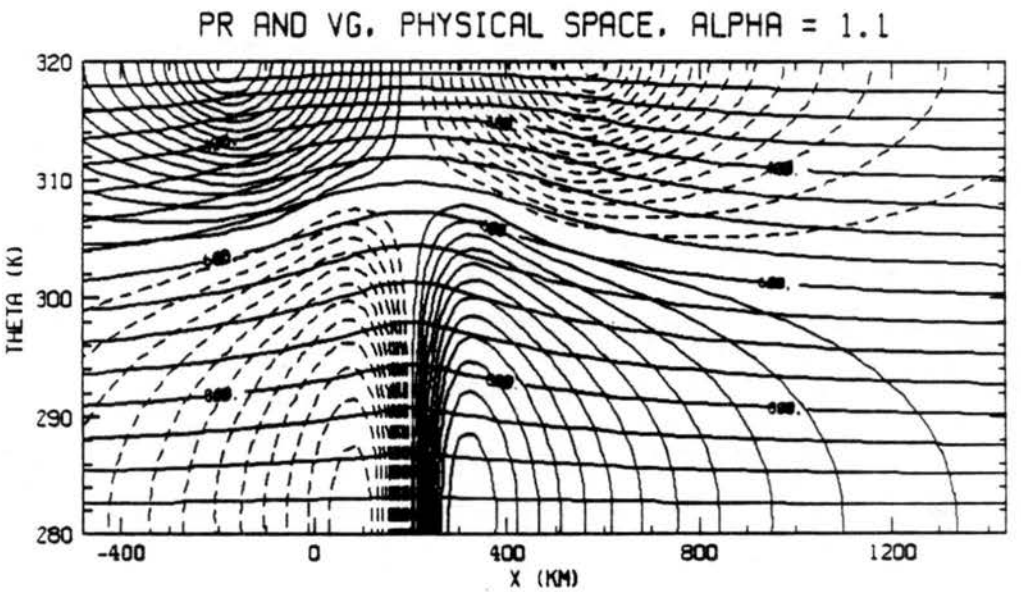

(b)

Figure 2.6: Potential vorticity (a) and pressure and wind fields (b) for $T = 8$ hr, $Q_0 = 7$ K hr^{-1}, $X_0 = 80$ km, and $c = 50$ km hr^{-1}, resulting in $\alpha = 1.15$. Contour values as in Fig. 2.4.

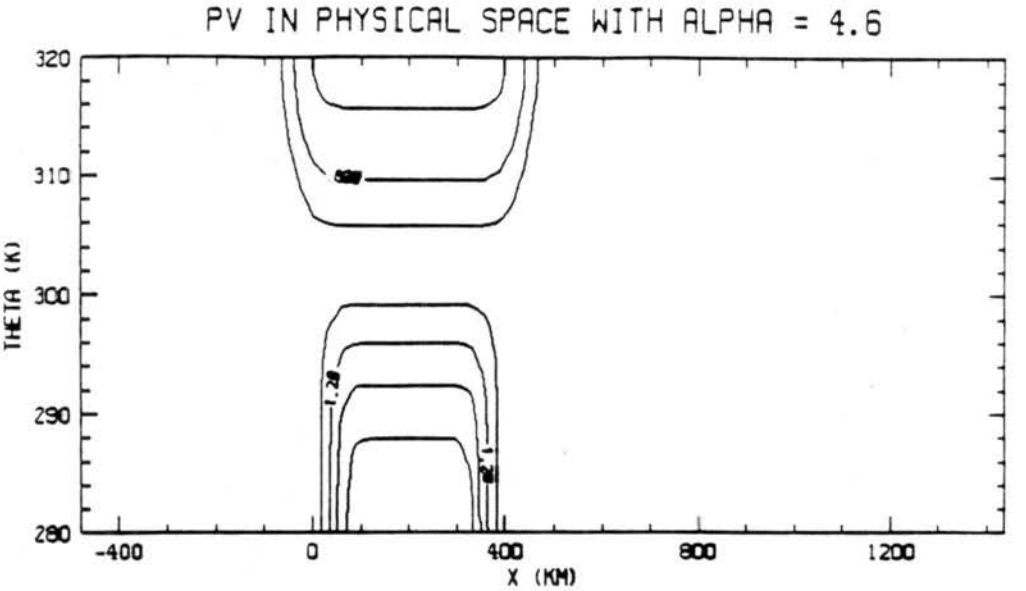

(a)

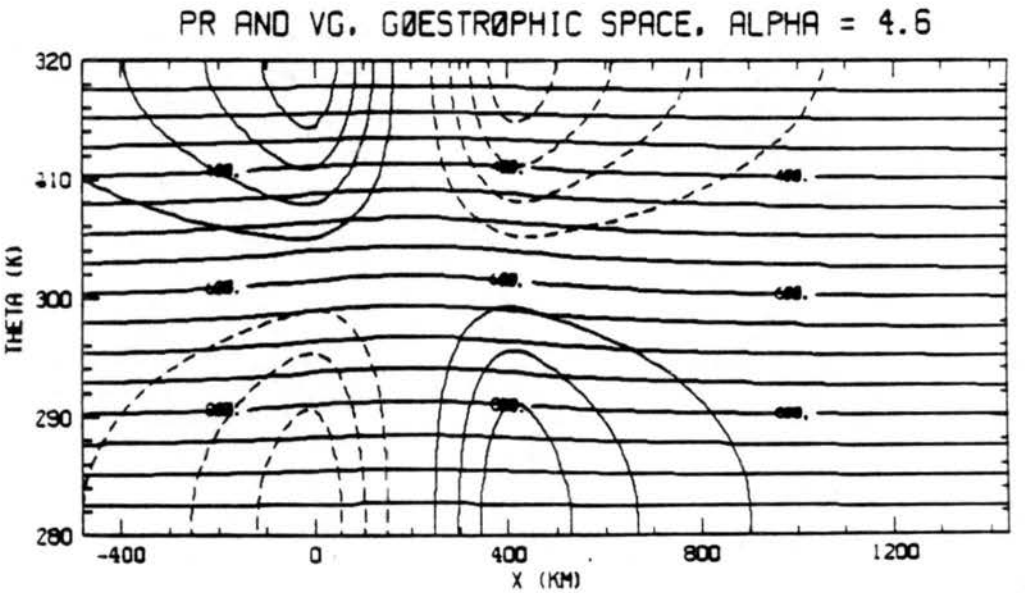

(b)

Figure 2.7: Potential vorticity (a) and pressure and wind fields (b) for $T = 8$ hr, $Q_0 = 3.5$ K hr^{-1}, $X_0 = 40$ km, and $c = 50$ km hr^{-1}, resulting in $\alpha = 4.6$. Contour values as in Fig. 2.4.

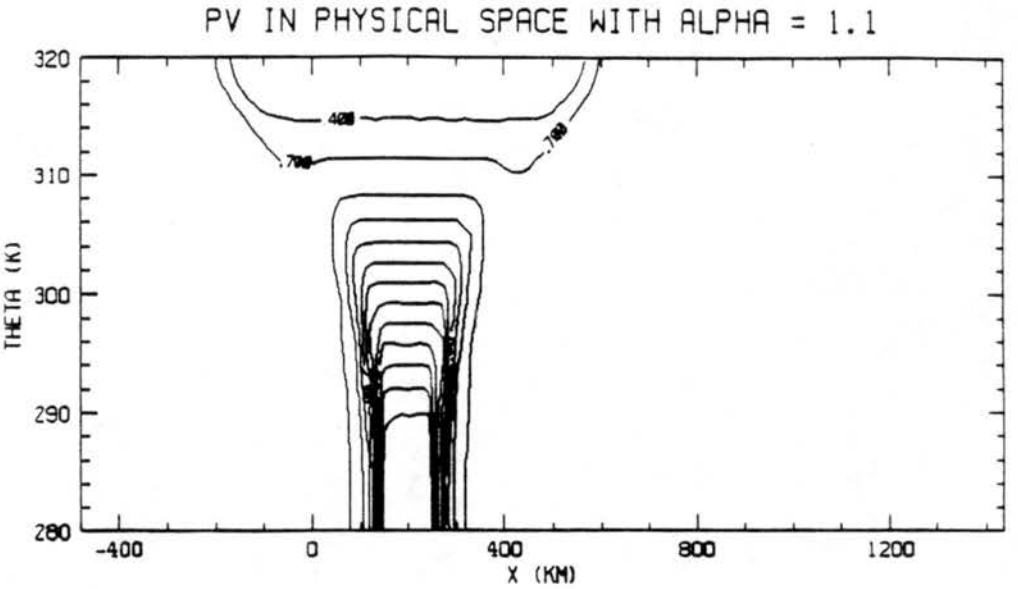

(a)

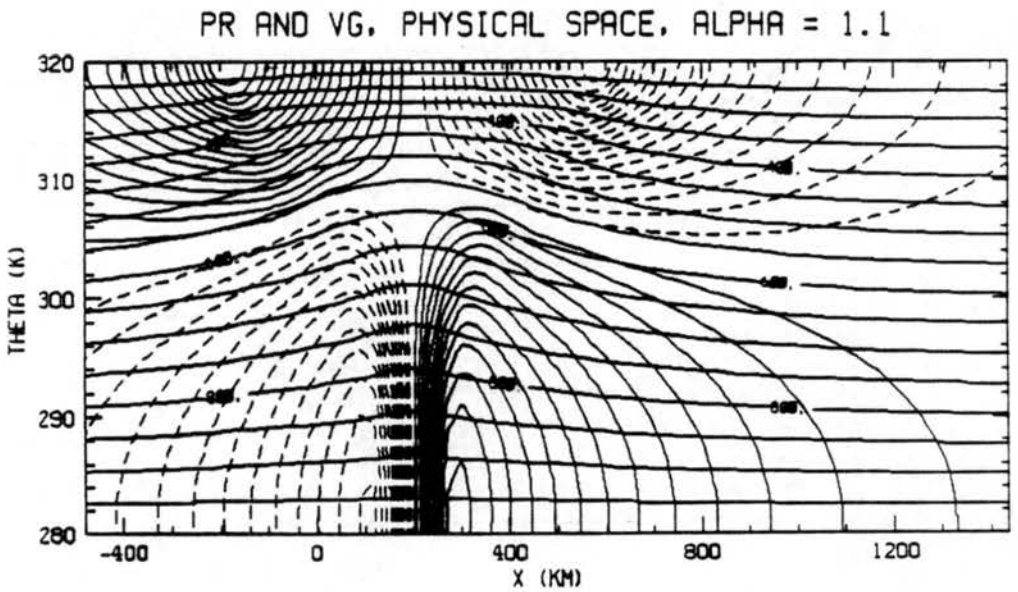

(b)

Figure 2.8: Potential vorticity (a) and pressure and wind fields (b) for $T = 8$ hr, $Q_0 = 14$ K hr^{-1}, $X_0 = 40$ km, and $c = 50$ km hr^{-1}, resulting in $\alpha = 1.1$. Contour values as in Fig. 2.4.

The final experiment involved changing the speed of propagation c. The speed was first increased by 15 km hr^{-1} to 65 km hr^{-1} which resulted in $\alpha = 3.0$. The perturbation q field (Fig.2.9a) extended farther horizontally as expected with a lower troposphere $q = 1.8$ and an upper troposphere $q = 0.6$. The q field has induced geostrophic winds of magnitude 6 ms^{-1} near the surface and 8 ms^{-1} at upper levels (Fig. 2.9b). Reducing the speed to $c = 35$ km hr^{-1} ($\alpha = 1.6$) increased the magnitude of the q field (Fig.2.10a) as well as increasing the induced flows by 1 to 3 ms^{-1}.

From these experiments the model has been found to give physically realistic results and is well behaved. Atmospheric response is greater for increased X_0 or Q_0, or decreased c. In contrast, atmospheric response is less for decreased X_0 or Q_0, or increased c. In all cases the induced geostrophic flows and perturbation pressure fields extended horizontally several hundred km beyond the q anomaly, therefore atmospheric response is on a larger scale than the actual q anomaly.

2.3.4 Experiments with a stratosphere

In applying the invertibility principle in all of the previously described experiments, horizontal and vertical gradients of M were bounded by a top boundary representing tropopause. In order to investigate possible stratospheric response to a tropospheric q anomaly, a stratosphere was added to the model.

As an initial test, an idealized stratosphere and associated σ profile were used. Instead of the 32 vertical layers used thus far, 64 vertical layers were used with the tropopause located at the vertical grid point $k = 32$. Two regions are defined, a troposphere with $\Theta_B = 280$ K, $p_B = 1000$ mb at the bottom and $\Theta_{Trop} = 320$ K, $p_{Trop} = 200$ mb at the tropopause; a stratosphere with Θ_{Trop}, p_{Trop} at the bottom and $\Theta_T = 400$ K, $p_T = 50$ mb at the top. This gives $\sigma = 2000$ mb K^{-1} in the troposphere and $\sigma = 50$ mb K^{-1} in the stratosphere (Fig. 2.11a). Potential vorticity was predicted to the tropopause only, simulating squall line convection that is capped by the tropopause and does not overshoot into the stratosphere. Thus the stratospheric q field remains unperturbed.

The q field resulting from an 8 hr simulation with $\alpha = 2.3$ is shown in Fig. 2.12a. This field is identical to that in the earlier experiment with $\alpha = 2.3$ (Fig. 2.2a), as would

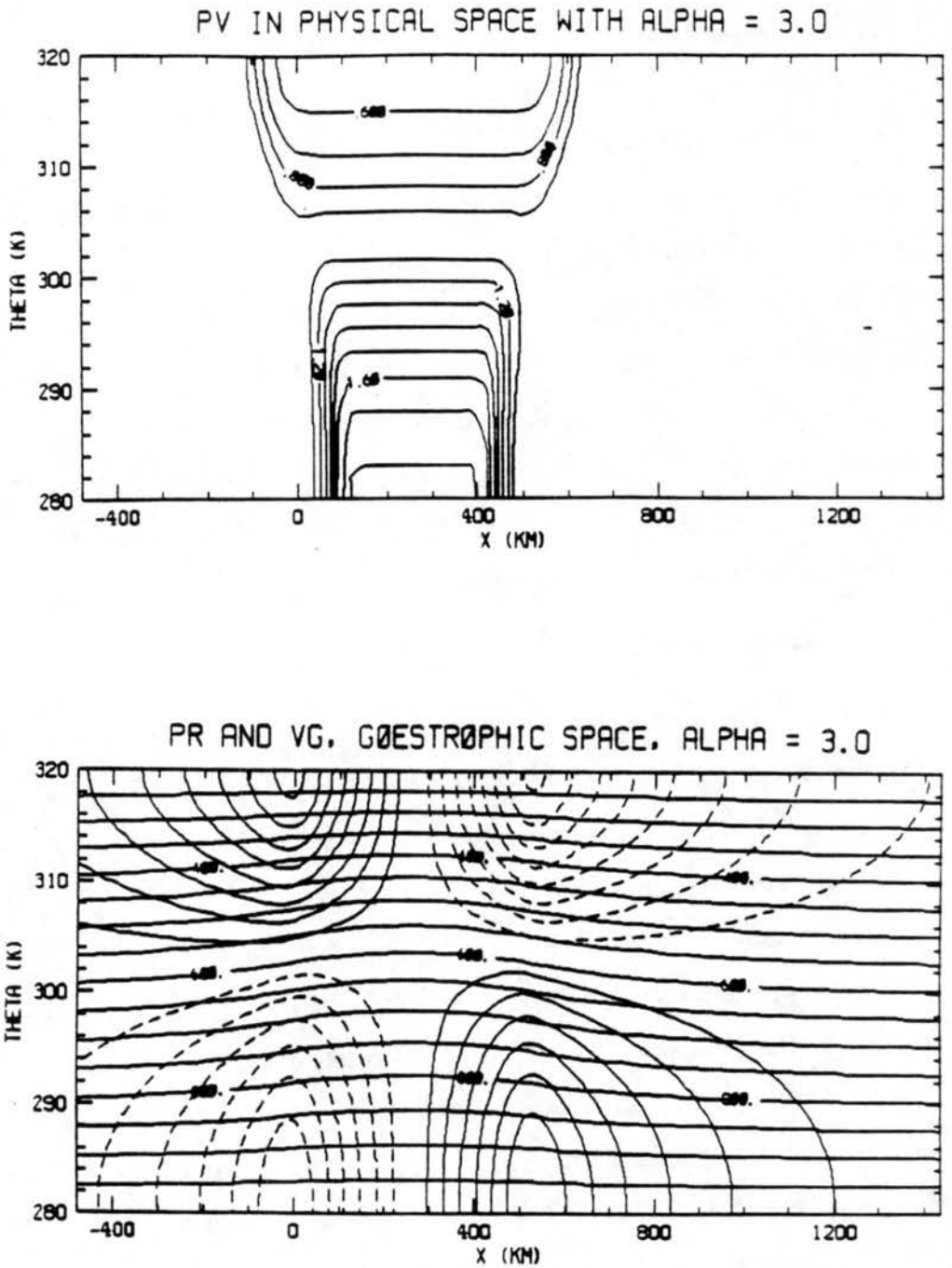

Figure 2.9: Potential vorticity (a) and pressure and wind fields (b) for $T = 8$ hr, $Q_0 = 7$ K hr^{-1}, $X_0 = 40$ km, and $c = 65$ km hr^{-1}, resulting in $\alpha = 3.0$. Contour values as in Fig. 2.4.

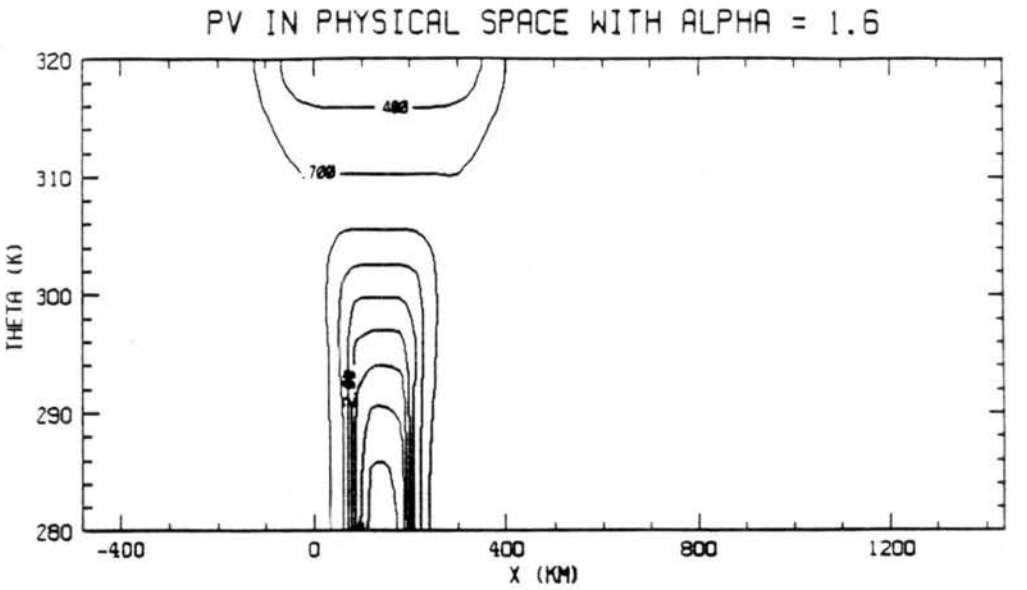

(a)

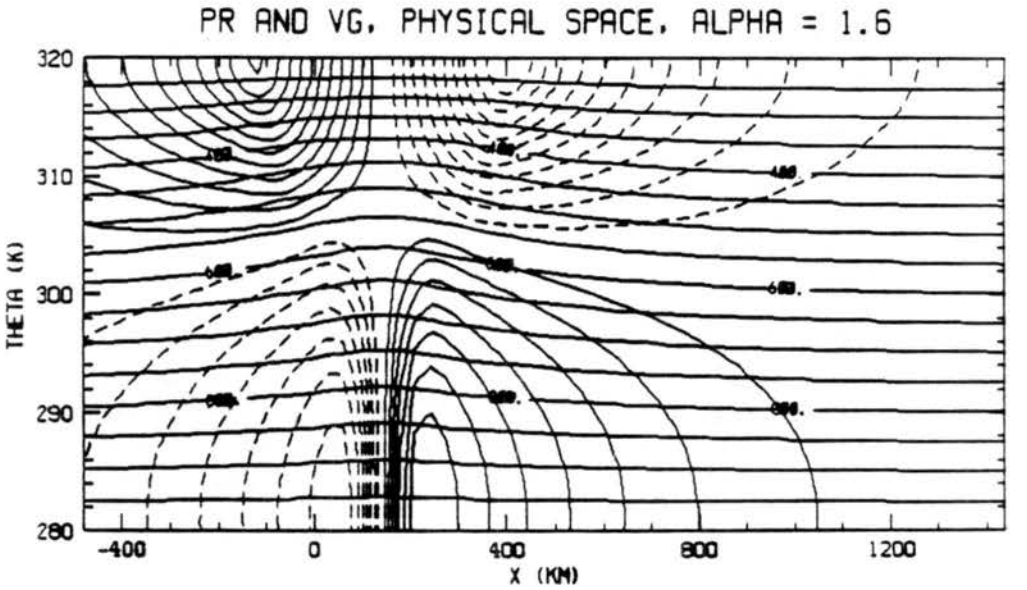

(b)

Figure 2.10: Potential vorticity (a) and pressure and wind fields (b) for $T = 8$ hr, $Q_0 = 7$ K hr^{-1}, $X_0 = 40$ km, and $c = 35$ km hr^{-1}, resulting in $\alpha = 1.6$. Contour values as in Fig. 2.4.

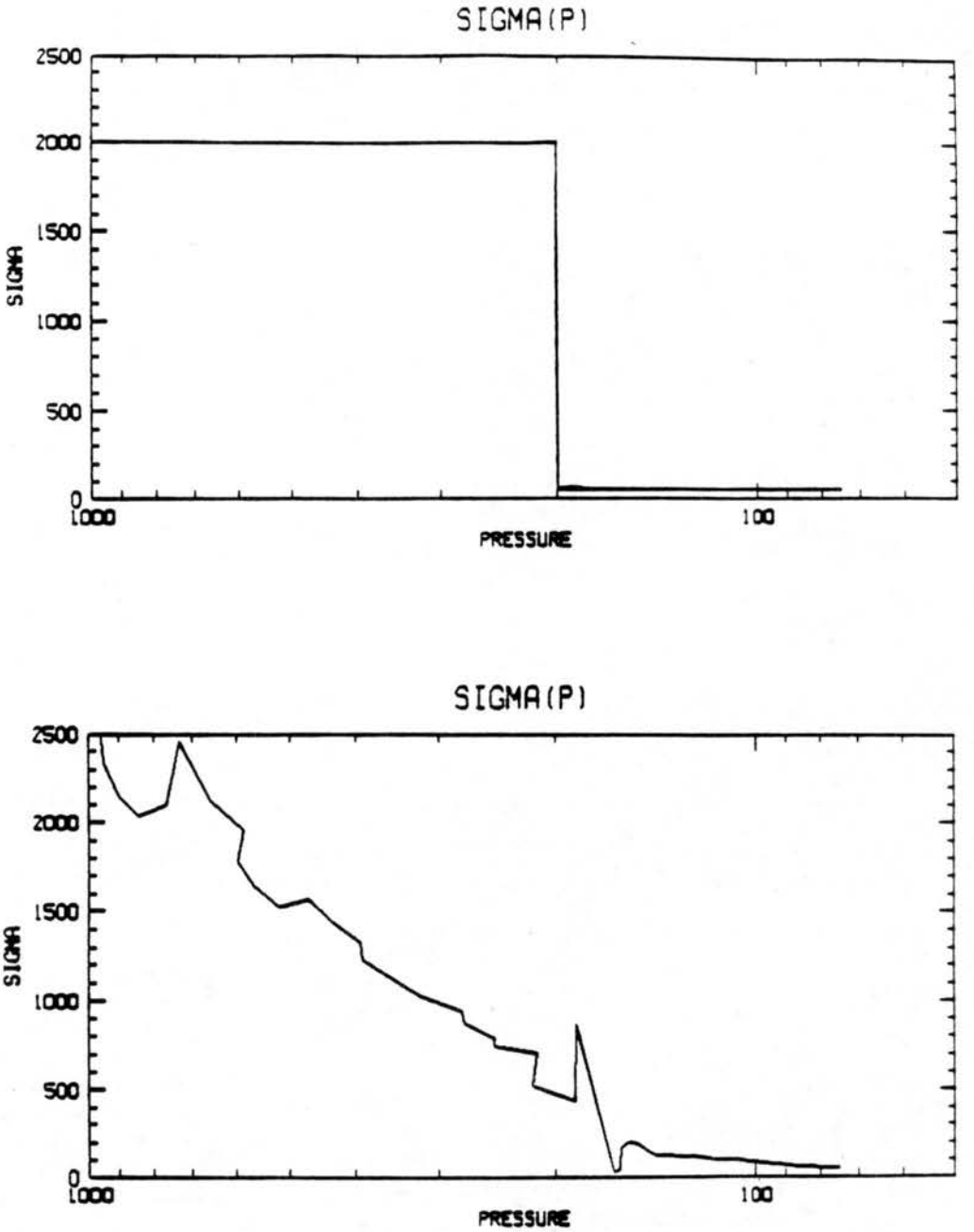

Figure 2.11: (a) An idealized atmospheric σ profile. (b) A standard atmosphere σ profile using data for July and 45 degrees north latitude from the U.S. Standard Atmosphere Supplements. σ is in units of pa K^{-1}.

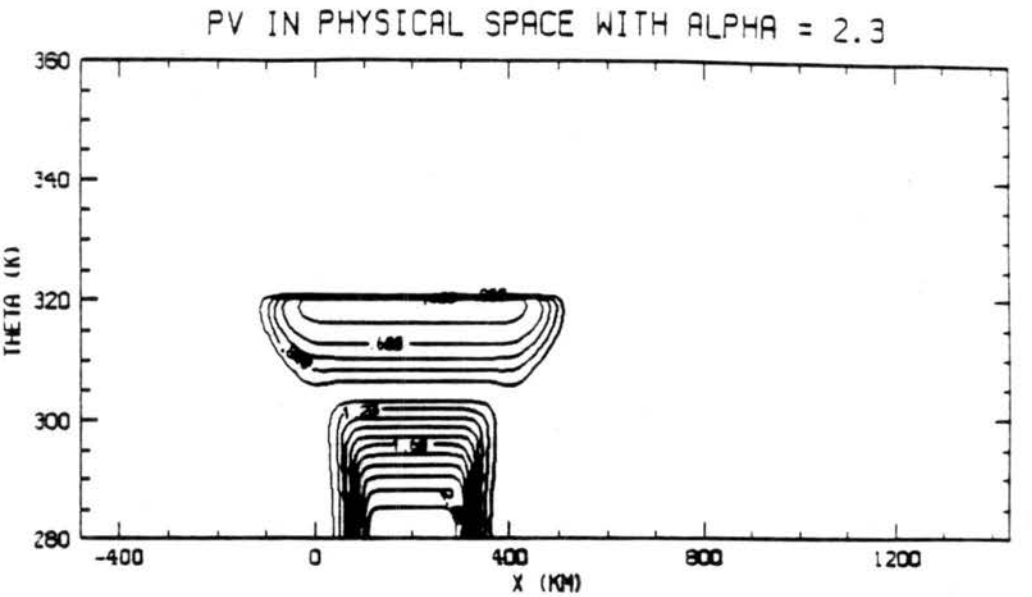

(a)

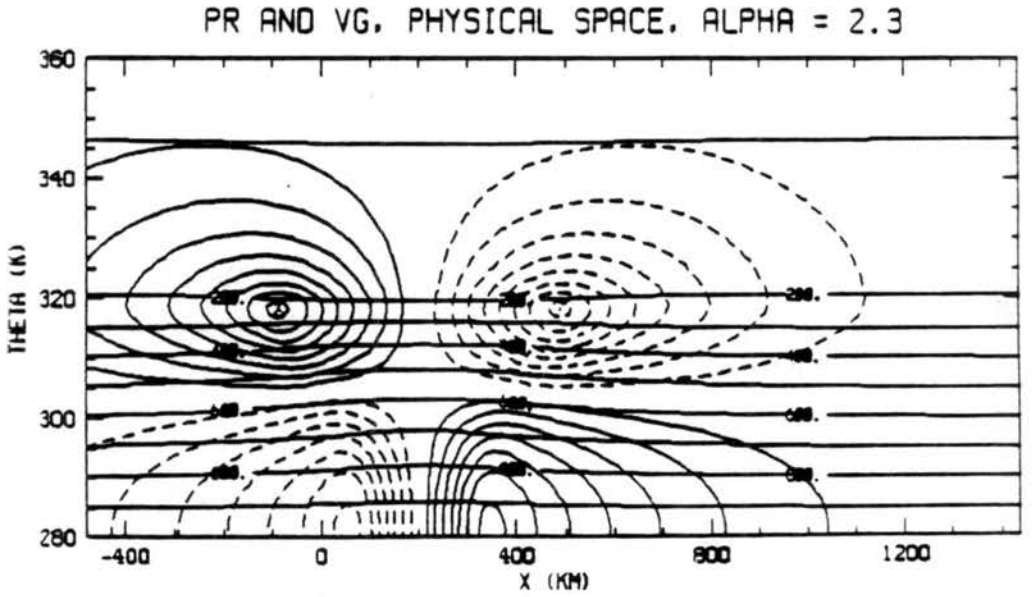

(b)

Figure 2.12: Potential vorticity (a) and pressure and wind fields (b) for an experiment with a stratosphere and a σ profile as given by Fig. 2.11a. The tropopause is located at 320 K. Contour values as in Fig. 2.4.

be expected since the q anomaly was not allowed to propagate into the stratosphere in this experiment. The resulting geostrophic flow field does propagate into the stratosphere (Fig. 2.12b), with induced v_g extending to the 100 mb (346 K) level. The magnitude of the flow at lower levels is unchanged from the previous $\alpha = 2.3$ experiment but has decreased by 1 ms^{-1} in the upper troposphere maximums (associated with the level of the tropopause). Careful examination of the upper troposphere q anomaly for the experiments with and without a stratosphere shows that the former produces a q anomaly which extends farther horizontally, reducing the horizontal q gradient in this experiment.

In order to test the effects due to a more realistic atmospheric stability profile, temperature, pressure, and geopotential height were taken from the US Standard Atmosphere Supplement for July and 45 degrees north. From temperature data potential temperature is easily calculated, from which a relation between isobaric and isentropic surfaces can be easily using a cubic spline routine. Geopotential heights multiplied by gravity g gave the geopotential; this combined with the temperature allows calculation of the Montgomery potential M. Noting that $\partial M/\partial\theta = \Pi$ and recalling the definition of Π, the pressure p can be derived. Finally the pseudo-density is simply given by the definition $\sigma = -\partial p/\partial\theta$. The σ profile thus obtained is shown in Fig. 2.11b. This profile is similar in magnitude in the lower troposphere and above the tropopause (above about 180 mb), but unlike the idealized experiment does not remain constant throughout the troposphere. The jump in σ at the tropopause may be due to the spline routine used to fit the data.

Using this standard atmosphere σ profile, an 8 hr simulation was run which produced the q anomaly field in Fig. 2.13a. This experiment with $\alpha = 3.2$ is similar to a previous experiment with $\alpha = 3.0$ (Fig. 2.9a). However as with the previous stratosphere experiment, the upper troposphere q anomaly extends farther horizontally, again resulting in weaker upper troposphere flows (Fig. 2.13b). This upper troposphere difference in v_g with or without the stratosphere is even more apparent in this experiment than with the idealized σ profile. In this experiment v_g has decreased by 4 ms^{-1} from 8 to 4 ms^{-1} in the upper levels. Thus it appears that the σ profile does play an important role in the atmospheric response especially in the upper levels.

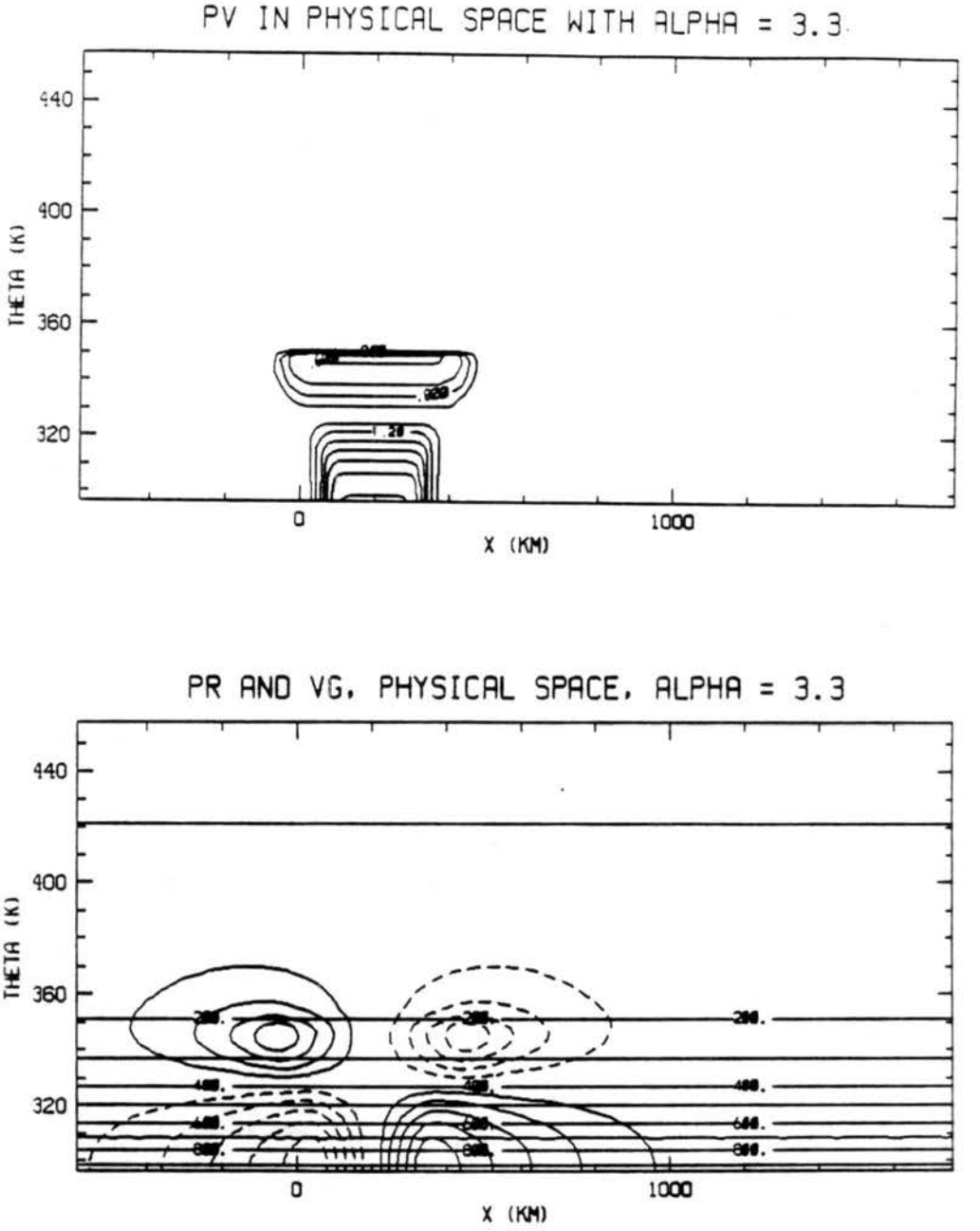

Figure 2.13: Potential vorticity (a) and pressure and wind fields (b) for an experiment with a stratosphere and a σ profile as given by Fig. 2.11b. The tropopause is located at 350 K. Contour values as in Fig. 2.4.

Chapter 3

OBSERVATIONAL STUDY

We begin our discussion of the observational study with a brief description of the source and type of data used. The second section deals with the analysis procedure to produce cross sections of potential vorticity and geostrophic winds. The next section gives a discussion of the synoptic situation during the case of interest, i.e., the 26/27 June 1985 PRE-STORM squall line. Results of the analysis are presented in the final section.

3.1 Data

3.1.1 Brief description of PRE-STORM

The upper air sounding data used in this study were from the Oklahoma-Kansas Preliminary Regional Experiment for STORM-Central (OK PRE-STORM). This field study was carried out between May 1 and June 27, 1985, and was set up to investigate the development and evolution of mesoscale convective systems (MCS).

Figure 3.1 shows some details of the measurement network, including the network domain and locations of various instrumentation. The network instrumentation included National Weather Service (NWS) WSR-57 radar, National Severe Storms Laboratory (NSSL) doppler radars, rawinsonde sites, profilers, and surface automated mesonetwork (SAM) and portable automated mesonetwork (PAM) sites. Also included were two P-3 aircraft as well as satellite support, both from polar orbiting and geostationary satellites. The supplemental sounding stations (PRE-STORM rawinsonde sites in Fig. 3.1) were able to be fully operational within two hours notice and could operate continuously for up to 18 hours. Details of the daily operations for the field study are found in Meitín and Cunning (1985).

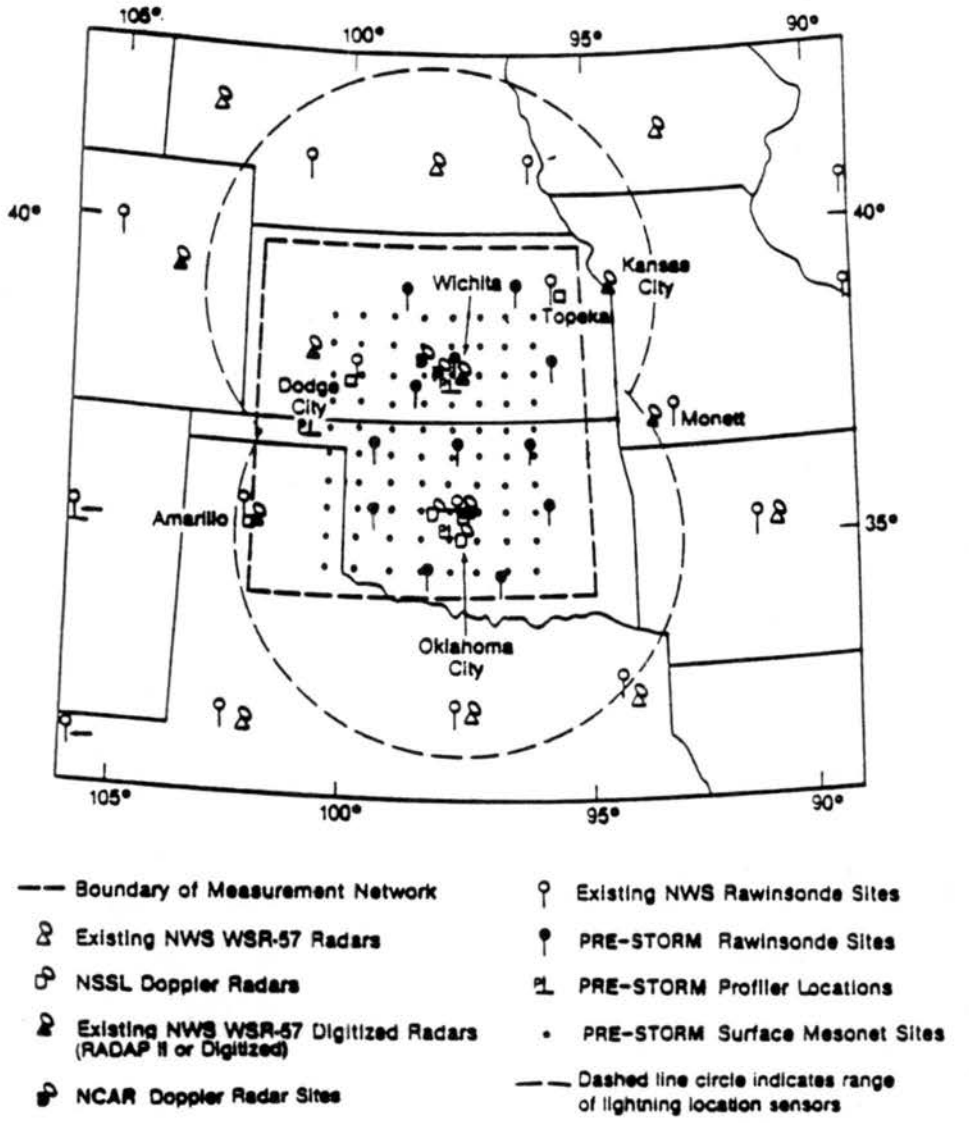

Figure 3.1: Overview of the surface measurement network showing its boundaries and the locations of various instrumentation (from Meitín and Cunning, 1985).

3.1.2 Sounding stations and available data

The sounding data from the OK PRE-STORM field study were obtained from the National Oceanic and Atmospheric Administration (NOAA) Environmental Research Labs (ERL) in Boulder, Colorado. A listing of the upper air network stations used in the analysis is given in Table 3.1. Soundings for all needed times and stations were not available. The levels to which partial soundings extended are provided in Table 3.2. PRE-STORM mesonet rawinsondes measured the same quantities as NWS rawinsondes: pressure, temperature, dew point, wind speed, and wind direction. Rawinsonde balloon positions were also available from PRE-STORM soundings.

Problems existed in the geopotential heights reported by station FSB. During the course of the field study, the rawinsonde station was moved from Fort Sill, Oklahoma (station FSI, elevation 361 meters msl) to Cache, Oklahoma (station FSB, elevation 425 meters msl). This change in station elevation was not taken into account while the soundings were made, resulting in a 64 meter error (i.e., too low) in the height data at every level reported by FSB. The correction was required for any sounding time at FSB for the case being studied, i.e., the 26/27 June 1985 squall line.

In addition to the PRE-STORM mesonet rawinsondes, there were three NWS rawinsonde sites within the measurement network, Oklahoma City (OKC), Dodge City (DDC), and Topeka (TOP). Since the soundings from these sites were not easily available for the time period of interest (00Z on 27 June), and would not have greatly enhanced the resolution, they were not included in this analysis.

3.2 Analysis procedure

The observational study was partially motivated by a need for verification of model output (described in Section 2.3). The model predicts potential vorticity q, and by application of an invertibility principle the component of the geostrophic wind along the squall line, $V_{g_\parallel}$, is then diagnosed. The two-dimensional model output is in an $x - \theta$ domain where x is in the direction perpendicular to the squall line and θ is in the vertical. Thus, analysed q and $V_{g_\parallel}$ fields from PRE-STORM data were of primary interest.

Table 3.1: Supplemental O-K PRESTORM sounding availibility. In the Date/Time column an 'F' denotes a full sounding, a 'P' denotes a partial sounding and an 'M' denotes a missing sounding.

Station ID	Station Name	Station Number	Lat N (° ′)	Long W (° ′)	Elevation (gpm)	Date/Time 26/2230Z	27/0000Z	27/0130Z
CNU	Chanute, KS	74547	37 40	95 29	305	F	F	F
CSM	Burns Flats, OK	74644	35 25	99 12	586	F	F	F
END	Enid, OK	74642	36 21	97 54	359	M	F	P
FRI	Fort Riley, KS	72455	39 06	96 48	403	F	F	F
FSB	Cache, OK	—	34 39	98 42	425	F	F	M
HET	Henryetta, KS	74645	35 25	96 01	271	F	F	F
HOY	Hominy, OK	74643	36 26	96 23	253	F	F	M
IAB	Wichita, KS	74548	37 37	97 16	418	F	P	F
PTT	Pratt, KS	74543	37 42	98 45	595	F	F	F
RSL	Russell, KS	74544	38 52	98 49	569	P	P	P
SUL	Sulphur, OK	74646	34 32	96 59	326	F	F	F
WWR	Woodward, OK	74641	36 26	99 31	667	F	F	F

Table 3.2: Levels to which data is available for stations with partial soundings.

Station ID	Date/Time	Level at which data ends (mb)
END	27/0130Z	570
IAB	27/0000Z	726
RSL	26/2230Z	324
RSL	27/0000Z	355
RSL	27/0130Z	227

Data for each station and each sounding time are contained in separate computer files, each of these contains information for 100 to 150 levels. In order to analyse the desired fields, geopotential heights Z, observed winds $\vec{V}$, and temperature T at every 50 mb between 900 and 200 mb were needed (details on these needed parameters to follow). A vertical interval of 50 mb was chosen as having sufficient resolution for this analysis since the interest here is in the general fields and not in the specific details. The raw soundings did not always give data at the desired level, thus a cubic spline routine was used which provided accurate interpolation if data was not available at the desired level.

To enhance the spatial resolution of the sounding data available over the mesonetwork, soundings from 26/2230Z (i.e., June 26 at 2230Z), 27/0000Z and 27/0130Z were then composited over these times based on the station position relative to the squall line. This approach effectively increased the number of stations from 12 to 33 (not all of the soundings during this period were available, see Table 3.1). The method applied was as follows. Composite radar images were generally available over the measurement network at about 30 minute intervals (Fig. 3.2(a)-(f)). Using the leading edge of the radar image, which represents a 15 dBz radar return, a chronology of the squall-line leading edge positions was obtained. From these positions, the direction of movement of the squall line (the direction towards which the squall line was moving) was determined to be 130°, i.e., southeasterly. The speed of the squall line was calculated over several different time intervals. This ranged from about 9 to 11 ms^{-1}, with an average speed of propagation c = 9.75 ms^{-1}, which agrees with the findings of another investigator (Bill Gallus, personal communication). The location of each station is then moved at the speed c for 90 minutes (i.e., the approximate time interval between soundings) giving a distance of 52.7 km, and in the direction of either 130° or 310° depending on the sounding time. At 26/2230Z the situation at a given station is analogous to the situation 90 minutes ahead of the squall line position at 27/0000Z, so the station position using 26/2230Z data is moved towards 130°. Using 27/0130Z data, station positions are moved towards 310°. An important underlying assumption with this compositing technique is that the squall line is dynamically in steady state over the time interval of interest. This was subjectively determined from radar images to be approximately true for this case (Fig. 3.2(a)-(f)).

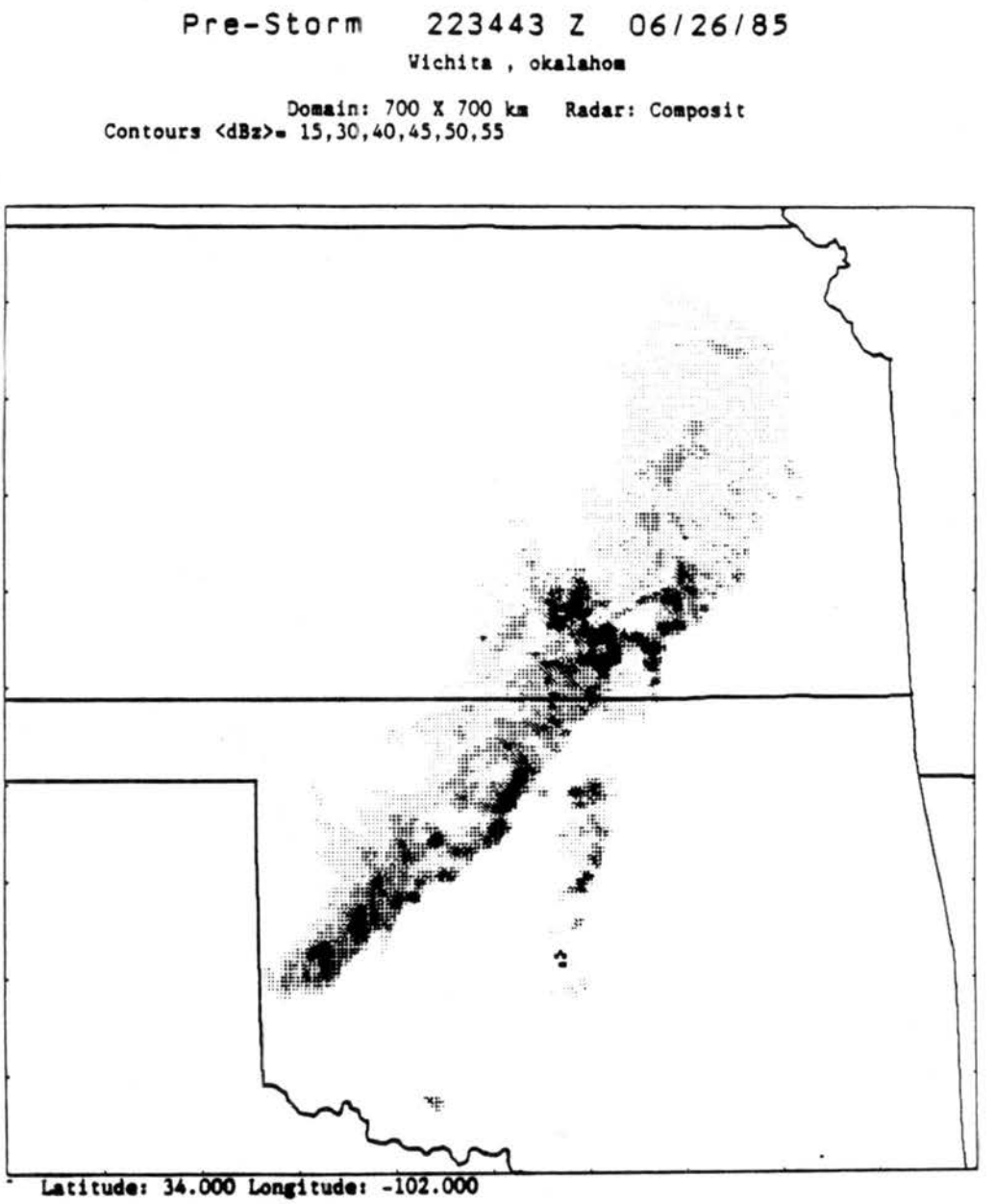

Figure 3.2: (a) PRE-STORM radar images for 26 June 1985 2235Z.

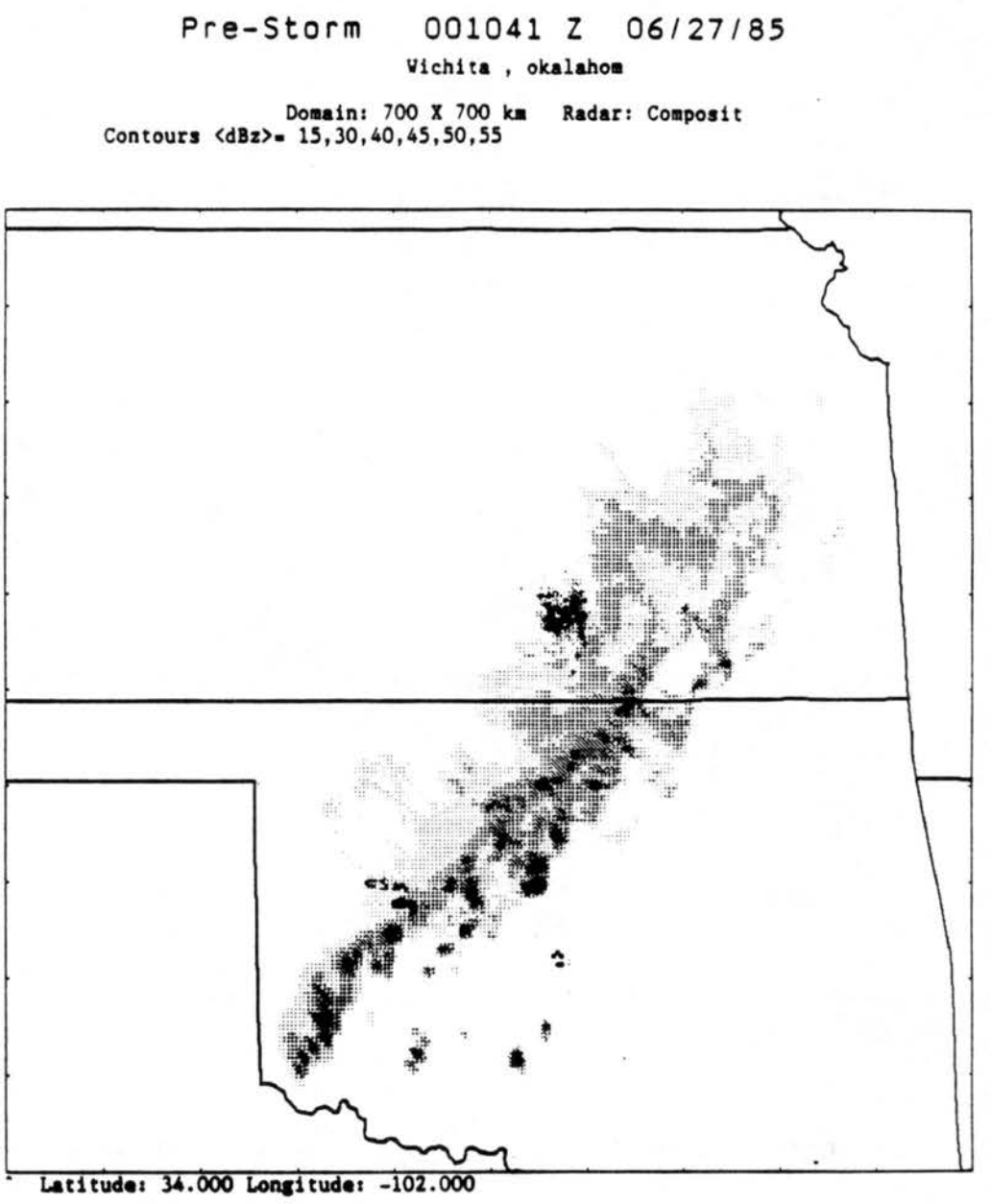

Figure 3.2: (b) PRE-STORM radar images for 27 June 1985 0011Z.

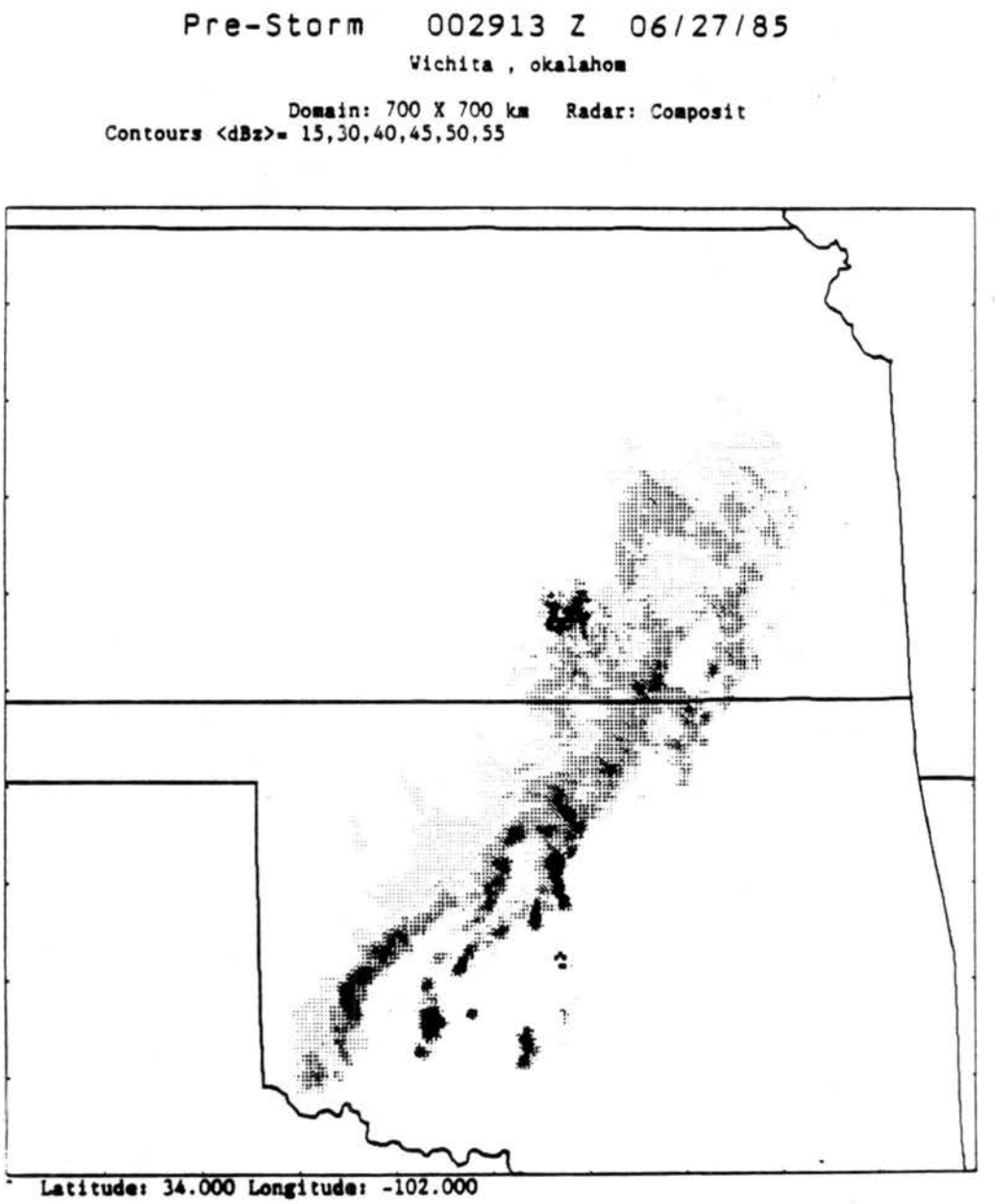

Figure 3.2: (c) PRE-STORM radar images for 27 June 1985 0029Z.

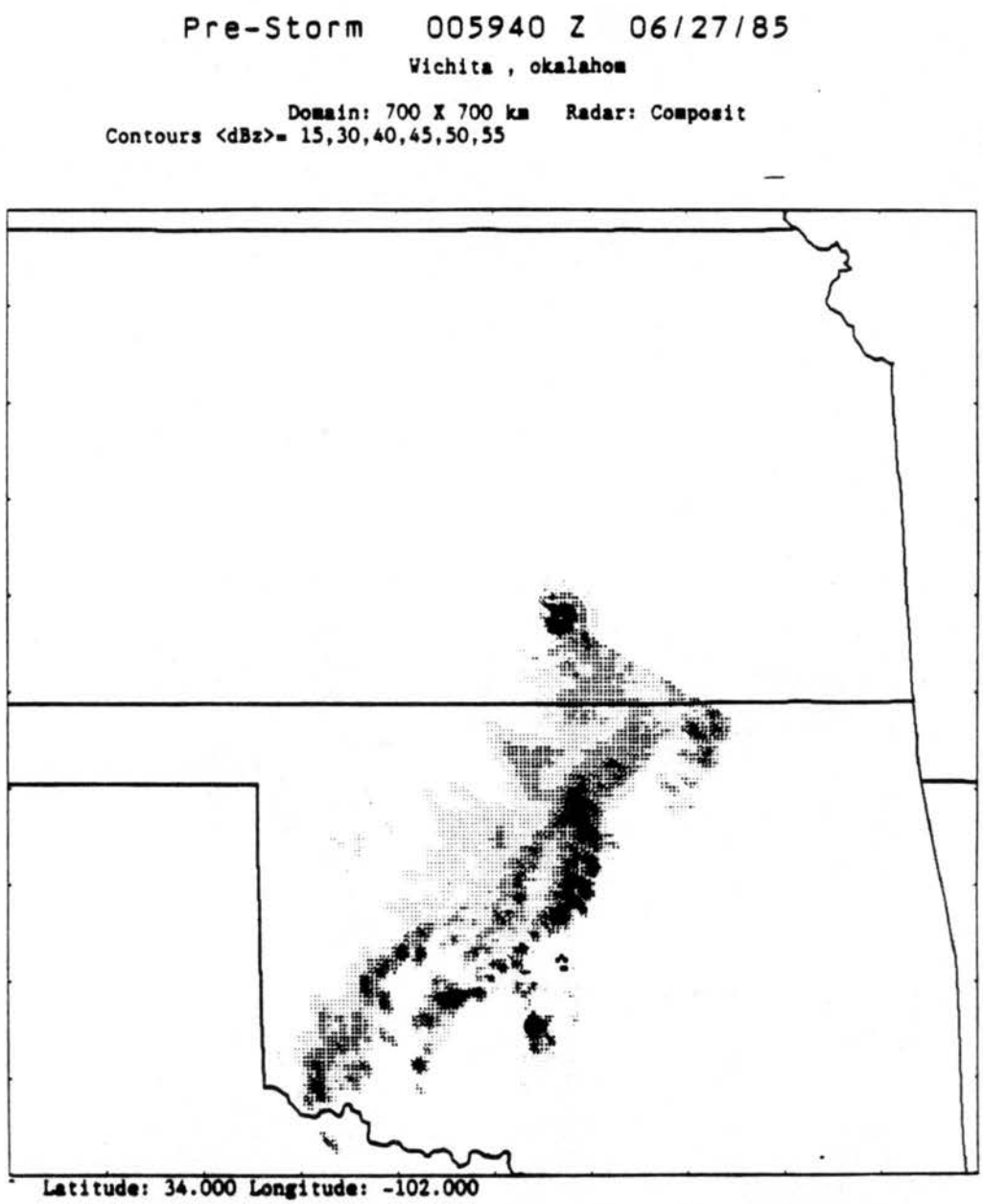

Figure 3.2: (d) PRE-STORM radar images for 27 June 1985 0100Z.

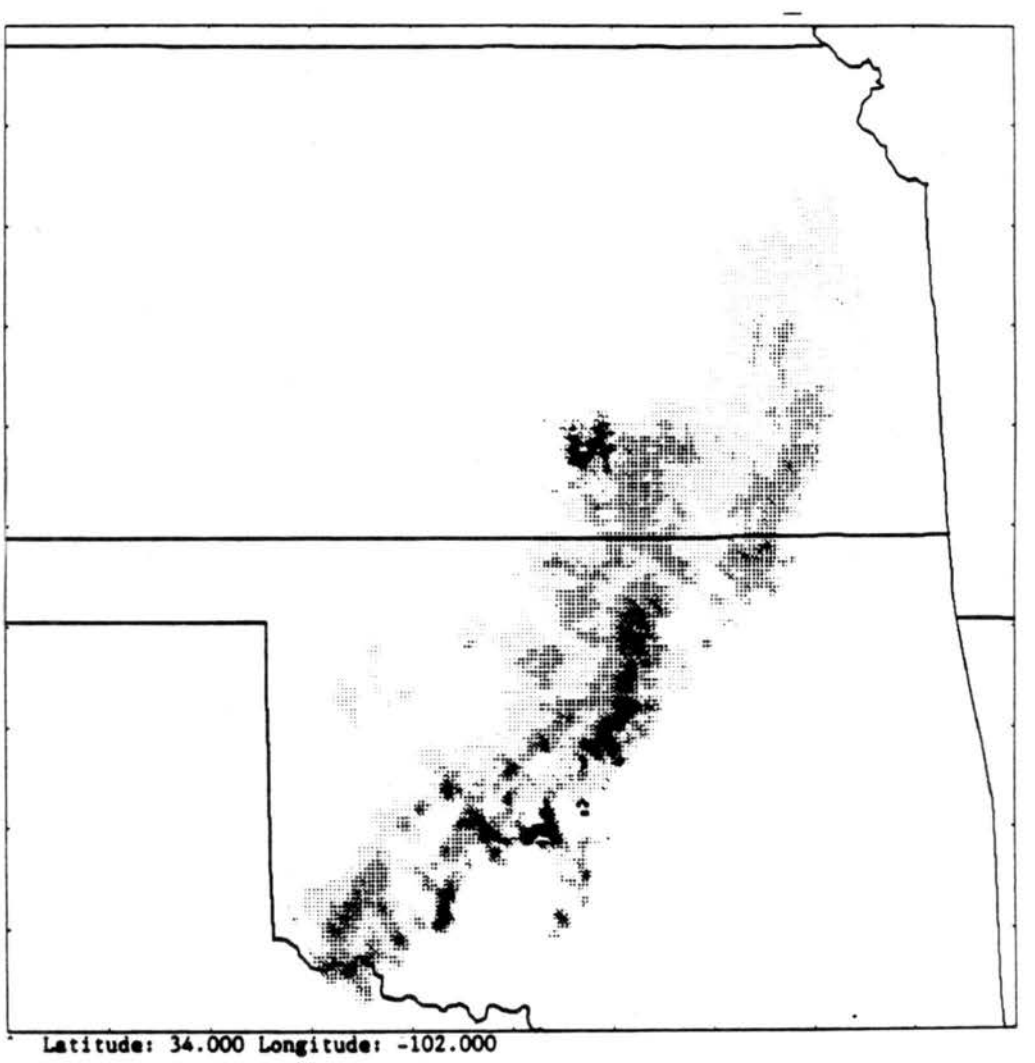

Figure 3.2: (e) PRE-STORM radar images for 27 June 1985 0134Z.

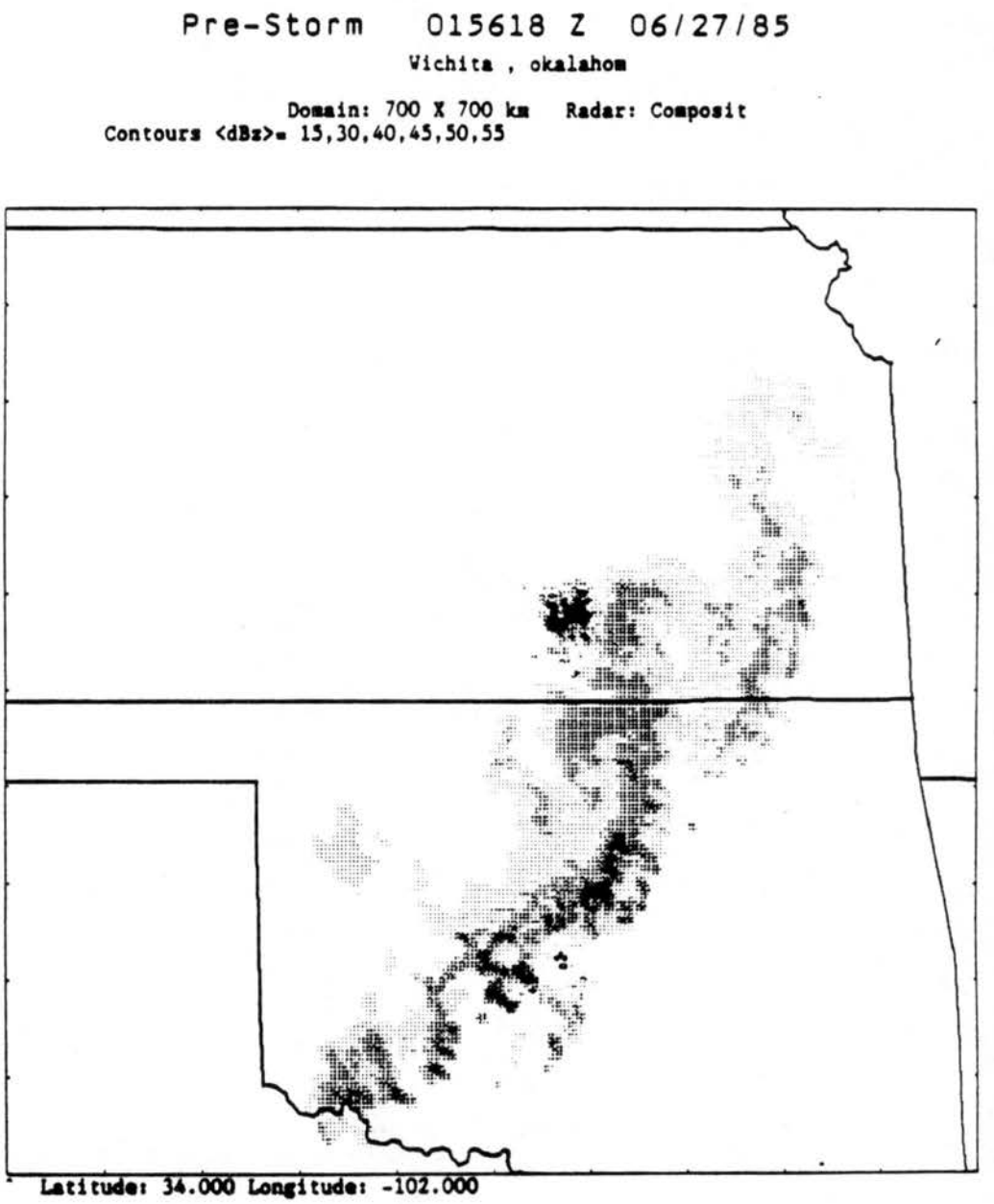

Figure 3.2: (f) PRE-STORM radar images for 27 June 1985 0156Z.

In order to calculate q and $V_{g_{\|}}$, information was needed on a rectangular grid. A Barnes (1964) objective analysis technique was applied to each pressure level for the needed parameters at the 33 composited sounding sites. In an effort to perform the analysis in the most data rich region, the analysis boundaries were set along 33.5° to 40° north latitude and 95° to 100° west longitude (Fig. 3.3). The north-south domain was divided into 29 intervals and the east-west domain into 18 intervals, giving a grid spacing in either direction of approximately 25 km. For calculations, the dependence on latitude of the distance of one degree of longitude was taken into account. An average spacing between observation sites was estimated to be 3 grid units (i.e., 75 km) with a radius of influence also chosen to be 3 grid units. It was suggested (Stanley Barnes, personal communication) that for a mesoscale observational network of this size, features on a scale of less than 150 km could not be reliably resolved. Thus, a response function should be chosen which eliminates essentially all features smaller than 150 km and then increases as rapidly as possible. By experimentation it was determined that a Barnes (1964) analysis parameter $E = 6$, with four objective analysis iterations, produced the most rapid increase after filtering 93 percent of the $6\Delta x$ or $6\Delta y$ features (i.e., those of a size six times the average grid spacing). Fields of interest were analysed at every 50 mb between 900 and 200 mb.

The gridded geopotential height fields were manually contoured for a few levels. These plots were then qualitatively compared to the values at the observation sites as a check of the accuracy of the objective analysis scheme. This also served as a check for possible errors (e.g., due to problems with data transmission) in computer-generated contour plots.

Components of the geostrophic wind were calculated from the gridded values of the Z field and approximations to the geostrophic wind equations

$$u_g = -\frac{g}{f}\frac{\Delta Z}{\Delta y}, \tag{3.1}$$

$$v_g = \frac{g}{f}\frac{\Delta Z}{\Delta x}, \tag{3.2}$$

where u_g and v_g are the east-west and north-south components respectively, $g = 9.8$ ms^{-1} is the acceleration due to gravity, $f = 8.57 \times 10^{-5}$ s^{-1} is the Coriolis parameter at 36°

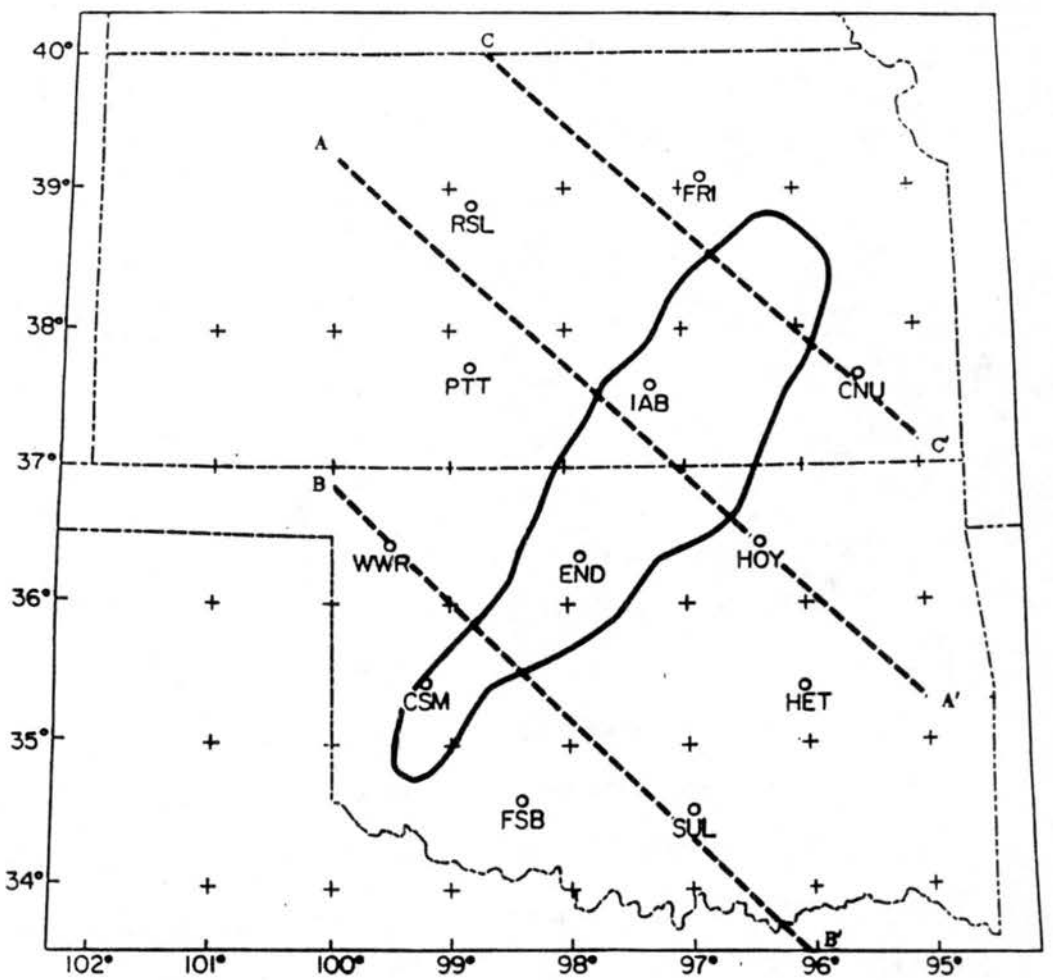

Figure 3.3: Map showing the analysis domain and the location of the supplemental sta tions. The station identifier is labeled next to the actual station location. The dark outlin represents the outline of the squall line radar image from 27/0000Z. Also shown are cross sections AA′, BB′, and CC′ (dashed lines).

north latitude, ΔZ is an increment in the vertical, and Δx and Δy are increments in the east-west and north-south directions respectively.

Since the squall line was aligned along a 40°–220° axis (i.e., northeast to southwest) the component of the geostrophic flow along this direction was required and was calculated from

$$V_{g_{\parallel}} = -V_g \quad \cos(\gamma - 40°), \tag{3.3}$$

where $V_g = ({u_g}^2 + {v_g}^2)^{1/2}$ and $\gamma = \tan^{-1}(u_g/v_g)$.

The height fields in close proximity to a squall line are often rapidly changing, thus there may not have been time for the winds to come into geostrophic balance (Johnson and Gallus, 1988). For this reason it is of interest to also examine the observed wind fields associated with this squall line to investigate whether any agreement exists between the observed and geostrophic wind fields. Observed wind components were analysed at each level and the component of the observed wind parallel to the squall line was calculated in a similar fashion to $V_{g_{\parallel}}$, that is,

$$V_{\parallel} = -V \quad \cos(\gamma - 40°), \tag{3.4}$$

where V is the magnitude of the observed wind and γ is the direction relative to true north.

Three-dimensional fields of $V_{\parallel}$ and $V_{g_{\parallel}}$ were obtained using the analyses at each level. From these, $x - p$ cross sections on isobaric surfaces were created at three locations across the squall line (Fig. 3.3). Since model calculations were on isentropic surfaces the vertical coordinate of the cross sections was transformed from isobaric to isentropic coordinates. From the original sounding data, potential temperature was calculated using Poisson's equation

$$\theta = T\left(\frac{p_0}{p}\right)^{\kappa}$$

where $p_0 = 1000$ mb and $\kappa = 2/7$. A cubic spline routine was accessed to fit p as a continuous function of θ (i.e., $p(\theta)$) and from this the spline was accessed a second time to obtain $V_{g_{\parallel}}(\theta)$ from $V_{g_{\parallel}}(p)$. The same technique was used to obtain $V_{\parallel}(\theta)$.

The final analysis involved cross sections of potential vorticity q along the same three locations in Fig.3.3. A three-dimensional q field was calculated using

$$q = -g\left\{-\frac{\partial v}{\partial p}\frac{\partial \theta}{\partial x} + \frac{\partial u}{\partial p}\frac{\partial \theta}{\partial y} + \left[f + \frac{\partial v}{\partial x} - \frac{\partial u}{\partial y}\right]\frac{\partial \theta}{\partial p}\right\} \tag{3.5}$$

where u and v are the east-west and north-south components, respectively, and $\partial/\partial x$ and $\partial/\partial y$ are taken on isobaric surfaces. As before the cubic spline routine was applied to obtain $q(\theta)$ from $q(p)$. Units of q from (3.5) are 10^{-6} m^2 s^{-1} K kg^{-1} which for convenience will de defined as 1 pvu. Hoskins et al. (1985) found 1.5 pvu to be a typical tropospheric value.

3.3 Synoptic situation

In this section a brief description of the synoptic situation associated with the 26/27 June squall line is presented. The 500 mb heights and vorticity are shown on Figs. 3.4 and 3.5. On 26/0000Z a trough with an associated vorticity maximum was located over the western United States (Fig. 3.4a). By 27/0000Z the trough axis moved about 500 miles to the east and the heights had risen by 20 meters (Fig. 3.5a). The vorticity maximum maintained its magnitude and moved in a northeasterly direction, which would put it well to the north of the PRE-STORM mesonetwork.

In connection with the 500 mb trough, a surface low was centered in central Minnesota on 26/1200Z with a surface cold front stretching southwestward through Kansas into New Mexico (Fig 3.6). The air mass in Oklahoma and southern Kansas was tropical in nature with dew points around 65°F.

The forecast group associated with the PRE-STORM field study expected scattered and mostly disorganised convection over western Oklahoma and central Kansas. Some of these were forecast to be heavy rain producers with the possibility that some could reach severe limits. Within the mesonetwork numerous thunderstorms were expected with some organization into a β–scale (i.e., approximately 200 km) system.

The squall line formed along the slow moving cold front and reached its greatest intensity in the few hours before and after 27/0000Z. By 27/1200Z (Fig. 3.7) the system

had moved southeast of the mesonetwork. As it passed over the area the squall line did produce numerous thunderstorms with heavy rainfall and one reported severe wind gust in Kansas.

3.4 Observational results

As described in Section 3.2, geopotential height Z fields were needed for the calculation of V_g. Analyses of Z at various levels are presented in Figs. 3.8–3.15. These figures represent a horizontal domain which extends 725 km in the north-south direction and 450 km in the east-west direction.

The major features below 500 mb are: 1. a general trough along the squall line 2. a mesolow to the northwest of the squall line 3. a mesohigh ahead and to the southeast of the main convective line. These features are somewhat in agreement with the findings of Johnson and Gallus (1988) in their analysis of the 10-11 June 1985 PRE-STORM squall line. In particular, at 650 mb (Fig. 3.11) the trough along the squall line is a common feature and possibly represents the stratiform region mesolow. This mesolow is thought to form in the mid-troposphere because latent heating in the stratiform cloud above and evaporative cooling in the precipitation below causes an evacuation of mass at that level. The along squall line trough may be in part due to the fact that this squall line formed along a cold front. Thus in this case it is somewhat difficult to differentiate features which are caused by the squall line itself and those which exist because of the synoptic situation. This feature becomes less obvious by 600 mb (not shown) and no longer evident by 500 mb (Fig. 3.12).

Another feature which is seen to about 400 mb and is most distinct at 700 mb is a mesolow to the rear and northwest of the squall line. Since this mesolow is located about 150 km from the stratiform region it is possibly not directly associated with the squall line dynamics. A third feature, the mesohigh ahead of the squall line, may be a relative feature due to the fact that air ahead of the squall line is still unperturbed.

Examination of the 500 mb heights (Fig. 3.12) shows a change in the general pattern from that observed in the lower troposphere. The definite trough along the squall line

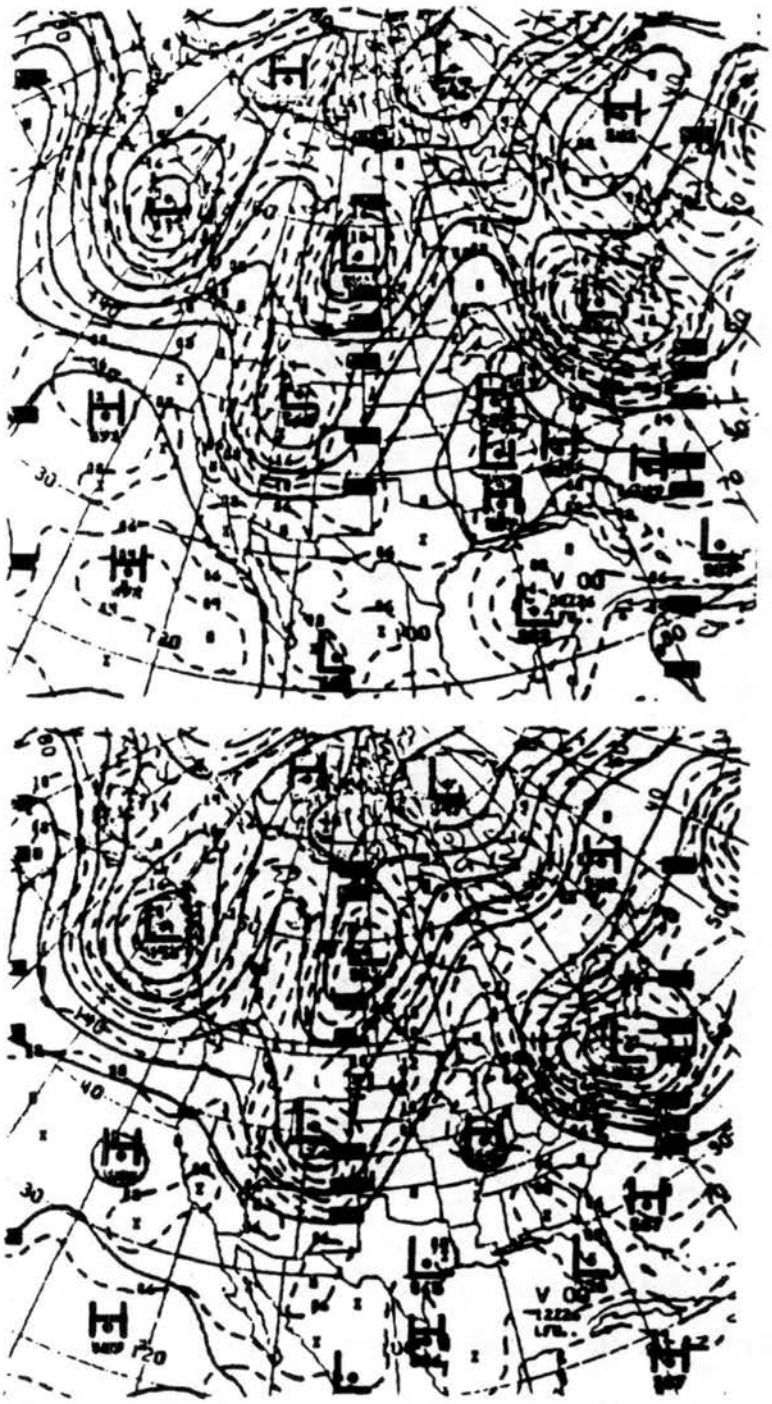

(a)

(b)

Figure 3.4: 500 mb heights (solid lines) and vorticity (dashed lines) for (a) 26 June 1985 0000Z and (b) 26 June 1985 1200Z.

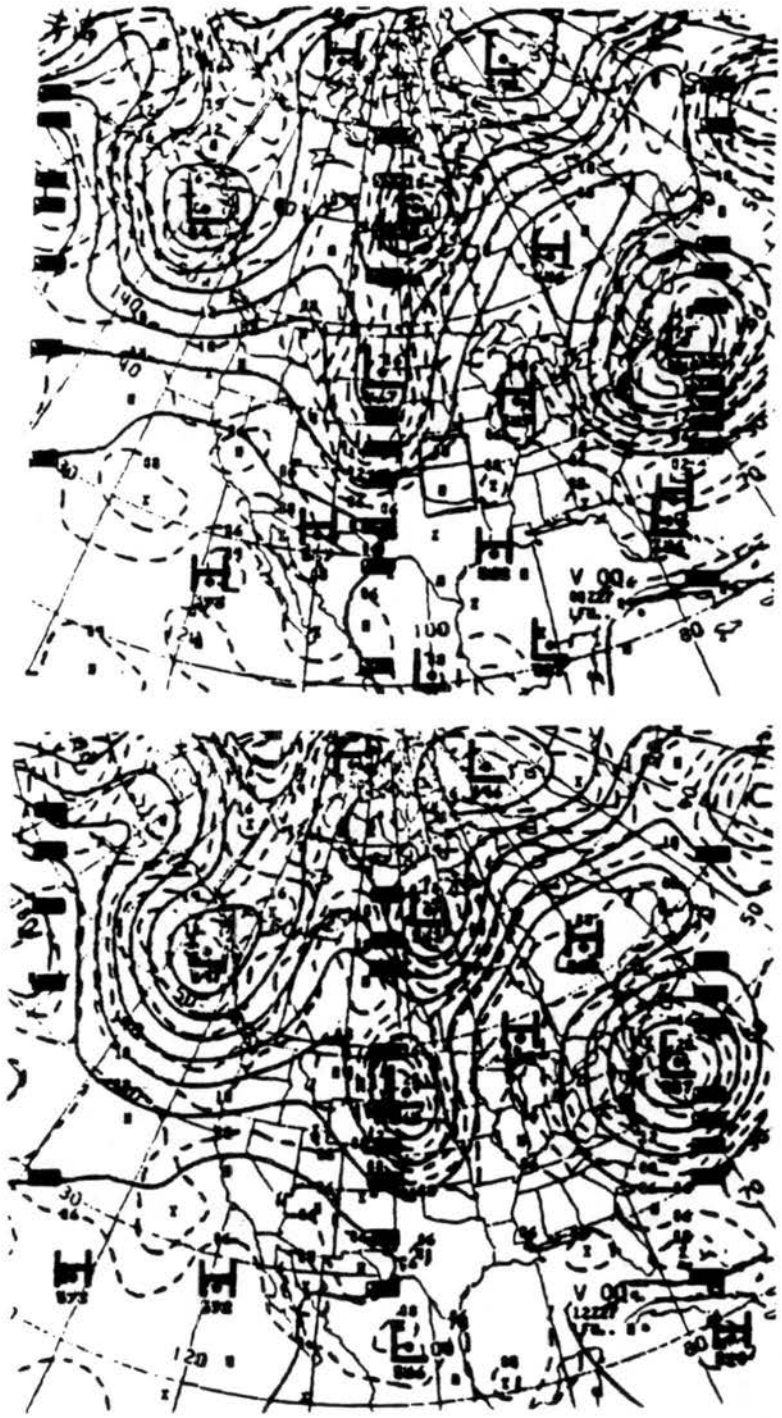

(a)

(b)

Figure 3.5: 500 mb heights (solid lines) and vorticity (dashed lines) for (a) 27 June 1985 0000Z and (b) 27 June 1985 1200Z.

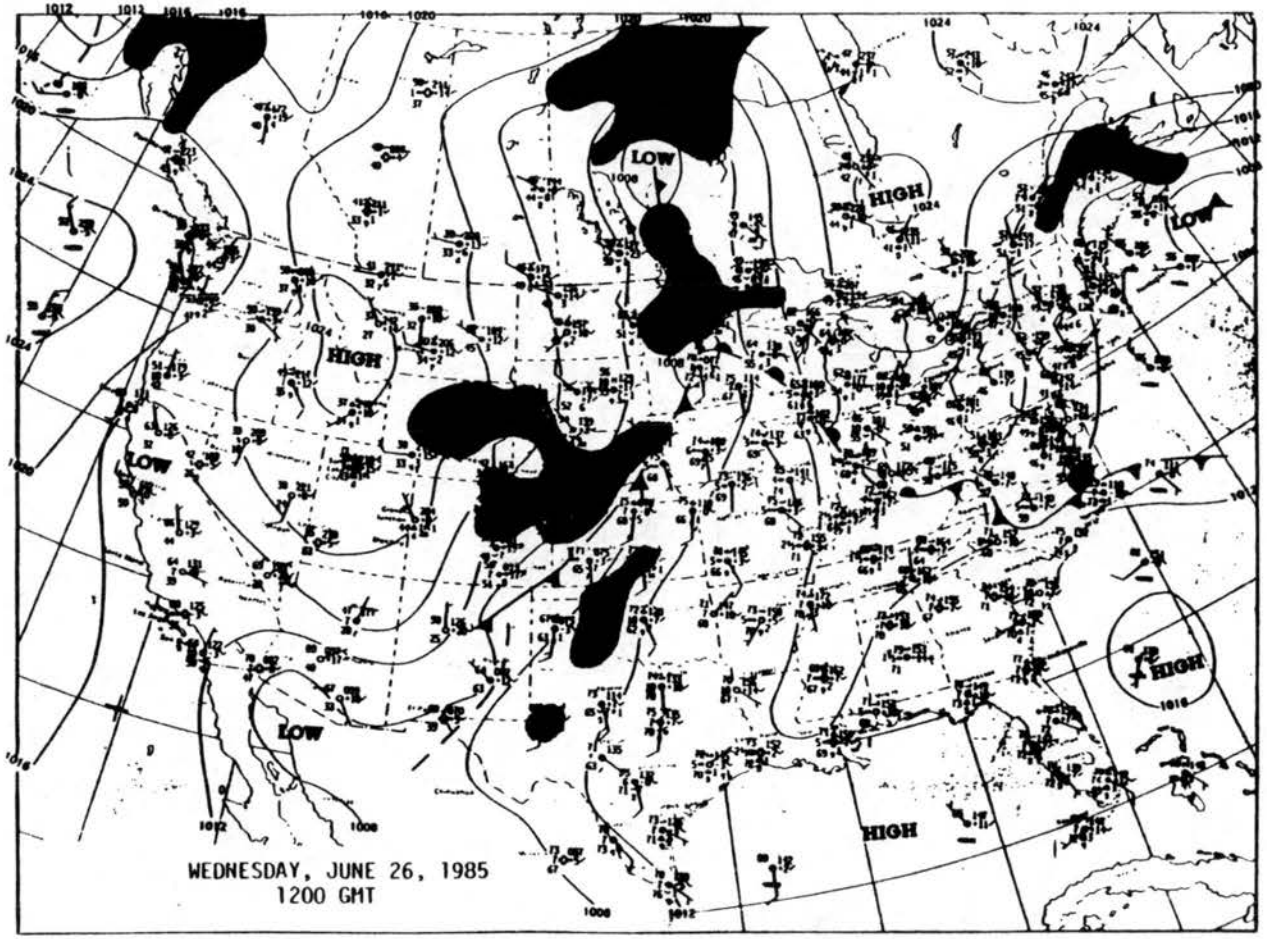

Figure 3.6: Surface chart for 26 June 1985 1200Z. Precipitation areas are shaded.

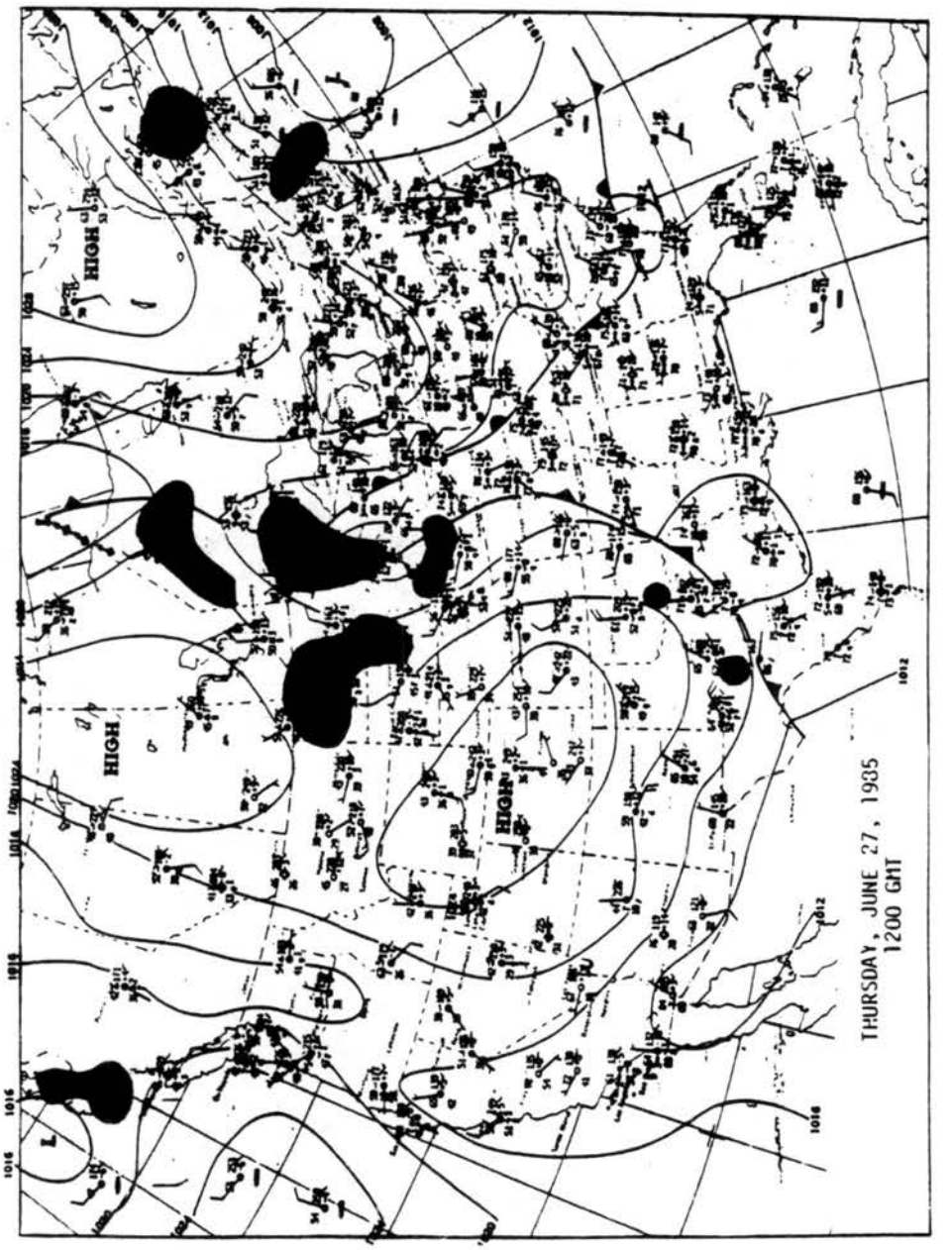

Figure 3.7: Surface chart for 27 June 1985 1200Z. Precipitaion areas are shaded.

is no longer present, the mesolow located to the northwest is much less evident and a mesohigh is now present to the rear squall line towards the southwest end. A gradual transition to this pattern is seen by inspecting Z fields at every 50 mb between 700 and 500 mb (600 and 550 mb not shown). By 400 mb a mesolow forms ahead of the squall line at the southwestern end; this features also shows up at 300 mb (Fig. 3.14) and to a lesser extent at 200 mb (Fig. 3.15).

Some caution is required when analysing the height fields since these fields are calculated from the hypsometric equation, which itself is derived from the hydrostatic equation. It is very possible in regions of strong convection to have non-hydrostatic effects, i.e., vertical accelerations. For this reason, the mesohigh to the rear of the squall line in the upper troposphere is suspect. Examination of the raw sounding data for station CSM shows that the 250 mb height at 26/2230Z is about 100 m higher than at either 27/0000Z or 27/0130Z. This large difference is likely due to a few strong convective cells that were in that area at 26/2230Z and then moved to the southeast (Fig. 3.2). Although a mesohigh is often found above and below the stratiform region mesolow, this mesohigh was located well to the southwest of the observed stratiform region.

Observed and calculated geostrophic wind fields associated with the height fields are found in Figs. 3.16–3.23. The observed flows at 850 mb (Fig. 3.17a) and 700 mb (Fig. 3.18a) are characterized by a trough-like feature with confluence along the leading edge of the squall line. The confluence becomes less evident by 700 mb, as the observed flow to the rear of the squall line becomes more zonal. The observed flows at 850 and 700 mb are in agreement with the findings of Johnson and Hamilton (1988) in their study of the 10/11 June 1985 squall line, but the magnitudes in this case are weaker by 5-10 ms^{-1}. There is some evidence for a weak rear inflow jet; the region of maximum flow within the radar echo region appears to shift towards the leading edge from 700 mb down to 900 mb.

The observed flow at 500 mb (Fig. 3.20a) appears to be most influenced by the major synoptic features, i.e., the trough at 500 mb approaching the mesonet from the northwest (Figs. 3.4 and 3.5). The general flow at this level is following the height contours, with stronger southwesterly flow in the northwest quadrant of the mesonet. However, the flow

is definitely being deflected by the squall line. Above 500 mb the observed flow is southerly to southwesterly in the northwest half of the domain and very weak in the southeast half. This again is in agreement with the synoptic flow at this level. Observed flow at 200 mb (Fig. 3.23a) shows a diffluence from the leading edge of the squall line probably due to outflow from the convective line. It should be noted that the vector lengths have been defined differently at 300 mb and 200 mb than at lower levels because of stronger flows at the upper levels.

Associated geostrophic winds (Figs. 3.16(b)-3.23(b)) do not agree well with the observed flow at the respective levels. At 850 mb (Fig. 3.17b) and 700 mb (Fig. 3.18b) there is some agreement in a qualitative sense with a general southwesterly geostrophic flow ahead and northwesterly geostrophic flow to the rear of the squall line. Above these levels it is difficult to find any consistent agreement between observed and geostrophic winds. Calculated geostrophic winds are also unrealistically strong at upper levels, reaching 176 ms^{-1} at 200 mb. At all levels the observed winds are subgeostrophic; this implies that the geopotential height fields are rapidly changing features and the winds have not yet had time to come into geostrophic balance.

Three cross sections analysed for this case are shown in Fig. 3.3. Cross sections AA′ and CC′ were taken across an area in which the squall line has a relatively wide horizontal extent, with a well developed stratiform region. Cross section BB′ was taken across an area in which the squall line is narrower in horizontal extent. All of the cross sections are presented using (a) an isobaric vertical coordinate and (b) an isentropic vertical coordinate.

The potential temperature θ cross section along AA′ (Fig. 3.24a) shows cooler temperatures at the surface to the rear of the squall line, while ahead of the squall line the lapse rate tends towards dry adiabatic in the lowest 50 mb (in all cross sections $x = 0$ km represents the squall line leading edge). Perturbations in the pressure fields become more apparent to the rear of the squall line. There is also a change in the vertical stability profile ahead of the squall line compared to behind the squall line. Ahead of the squall line the isentropes are relatively broadly spaced (less stable) below 600 mb and relatively closely spaced (more stable) above 600 mb. By contrast, to the rear of the squall line the

lower troposphere isentropes are relatively closely spaced and the mid troposphere isentropes (550-450 mb) are relatively broadly spaced. The stabilizing effect to the rear of the squall line in the lower troposphere may be due to cooling from stratiform precipitation while the upper troposphere destabilization is likely associated with latent heating in the stratiform cloud.

For cross section AA′, the potential vorticity q (Fig. 3.25) shows some vertical variation ahead of the squall line, with -0.2 pvu in the lower troposphere and 0.4 pvu in the upper troposphere (1 pvu = 10^{-6} K s^{-1} pa^{-1}). No distinct pattern appears ahead of the squall line, however behind the the squall line a definite perturbation pattern appears. Lower troposphere values of q have increased to a maximum of 1.5 pvu. Between 700 and about 350 mb the pattern behind the squall line is similar to that ahead of the squall line. Negative values of q are seen above 350 mb in the area behind the squall line with a minimum of -0.1 pvu. Thus the squall line has produced an anomaly in the q field such that an increase occurs in the lower troposphere while a decrease occurs in the upper troposphere.

The along squall line component of the observed wind $V_{\|}$ for cross section AA′ is shown in Fig. 3.26. Positive flow is into the page (solid lines) and negative flow is out of the page (dashed lines). Ahead of the squall line the flow is positive up to about 300-400 mb and negative above that. A more distinct pattern appears behind the squall line with a minimum of -8 ms^{-1} at 850 mb and a maximum of 28 ms^{-1} at 300 mb.

The $V_{\|}$ field agrees with what would be expected from the q field (Fig. 3.25) for cross section AA′. Potential vorticity is a combination of absolute vorticity and the mass field, as seen by (3.5). Thus the positive q anomaly in the lower troposphere would be expected to have associated cyclonic shear as well as the θ field perturbations (Fig. 3.24a). Similarly, the negative q anomaly in the upper troposphere should have associated anticyclonic shear.

Analyses at each level revealed little agreement between observed winds and geostrophic winds. However, inspection of cross sections of the along squall line component of the observed wind $V_{\|}$ and geostrophic wind $V_{g_{\|}}$ does show some agreement in the overall features behind the squall line. For cross section AA′, $V_{g_{\|}}$ (Fig. 3.27) shows a

lower troposphere minimum of -6 ms^{-1} near the surface and an upper troposphere maximum of 30 ms^{-1} at 300 mb. A mid-tropospheric $V_{g_{\|}}$ maximum is found at about 600 mb just behind the squall line leading edge. Ahead of the squall line there is little agreement.

Cross section BB′ was taken across a part of the squall line which was southwest of AA′ and which represents a less active part of the squall line. Examination of the θ field (Fig. 3.28a) shows a similar but less distinct pattern than AA′, with stabilization in the lower troposphere (especially below 750 mb) and destabilization in the layer between 550-450 mb.

Potential vorticity along BB′ (Fig. 3.29) shows a positive q anomaly in the lower troposphere below about 750 mb to the rear of the squall line. A negative q anomaly does not exist in the upper troposphere but values have decreased by a factor of about 3 from those ahead of the squall line at these levels. Also of note is that the magnitudes of q are lower by almost half those of the stronger squall line region represented along AA′.

Observed flows $V_{\|}$ along BB′ (Fig. 3.30) again show a similar pattern to AA′ but the magnitudes behind the squall line are weaker. The lower tropospheric $V_{\|}$ shows no significant negative flow and the upper tropospheric positive flow is about 10 ms^{-1} weaker than those along AA′. Geostrophic flows $V_{g_{\|}}$ along BB′ (Fig. 3.31) shows agreement with AA′ only in a confined region behind the squall line and below 600 mb.

Cross section CC′ represents an area in which the squall line has similar intensity to AA′. The θ field (Fig. 3.32a) shows the same characteristics as AA′, with stabilization in the lower troposphere and destabilization centered around 500 mb. Potential vorticity anomalies induced by the squall line along CC′ (Fig. 3.33) show the same pattern as AA′, however there are two differences. First the lower troposphere positive maximum is displaced further behind the squall line along CC′ (by approximately 50 km) and is stronger by about 0.6 pvu. Second, the horizontal extent of the negative q anomaly in the upper troposphere is smaller along CC′ than AA′.

Observed winds along CC′ again show the same pattern as along AA′ but the magnitudes of $V_{\|}$ (Fig. 3.34) in both the upper and lower troposphere are weaker than AA′. Geostrophic flows $V_{g_{\|}}$ along CC′ (Fig. 3.35) also show some agreement with those in AA′.

Summarizing the main features found in the cross sections, the following appear to be induced by the squall line passage:

1. a positive potential vorticity anomaly in the lower troposphere and negative potential vorticity anomaly in the upper troposphere.

2. negative $V_{\parallel}$ in the lower troposphere and positive $V_{\parallel}$ in the upper troposphere.

3. geostrophic flows $V_{g_{\parallel}}$ that have the same pattern and general magnitude as $V_{\parallel}$.

4. stabilization of the lower troposphere and destabilization in mid levels around 500 mb.

The third item implies that the structure along the squall line has been dynamically steady enough over time for some balanced flow to begin, whereas the analyses at each level indicate that no balance occurs in the direction across the squall line. This is probably due to the individual convective cells along the squall line that are not at all steady in time.

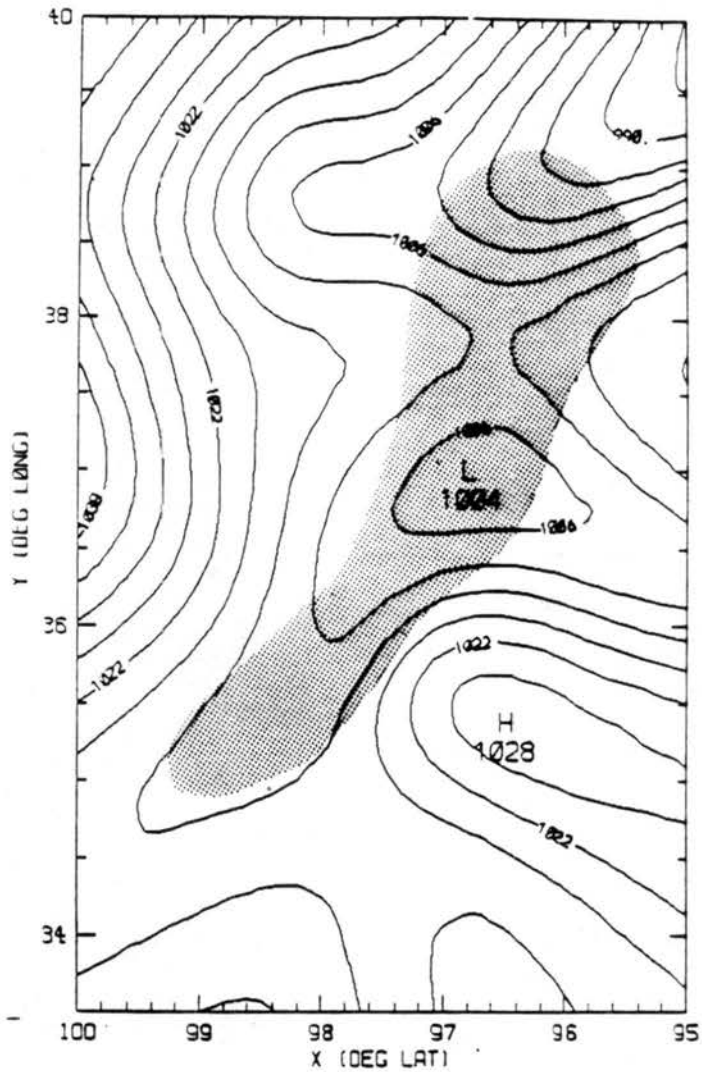

Figure 3.8: Geopotential heights (m) at 900 mb. Shaded area represents the 15 dBz or greater radar image at 0000Z.

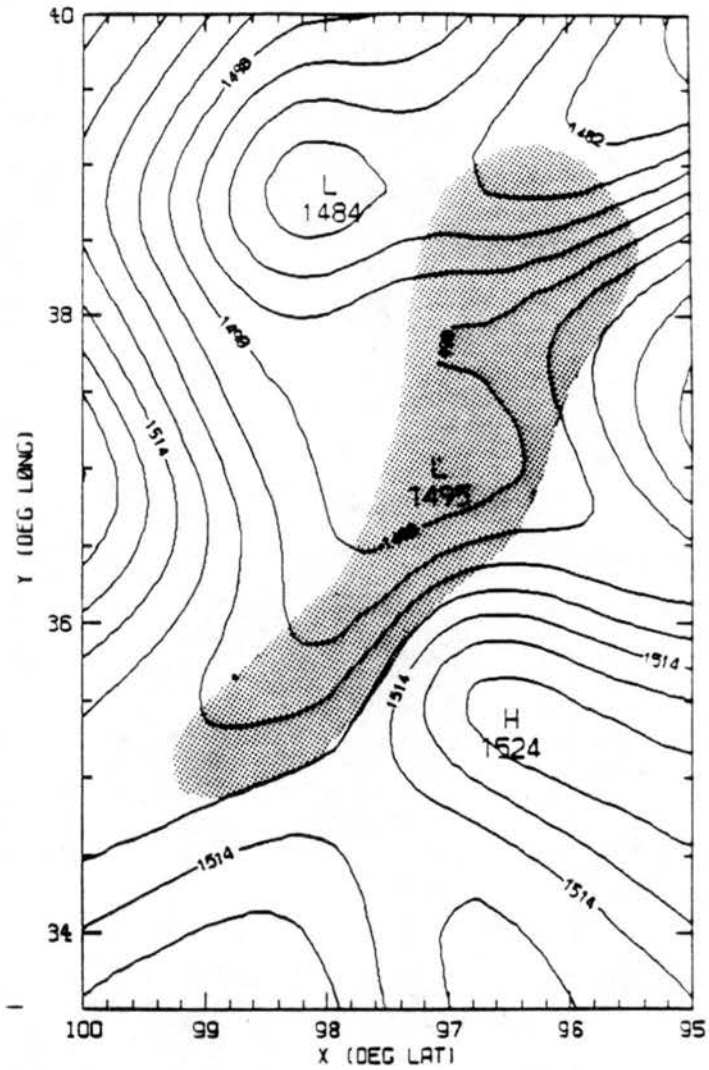

Figure 3.9: As in Fig. 3.8 except at 850 mb.

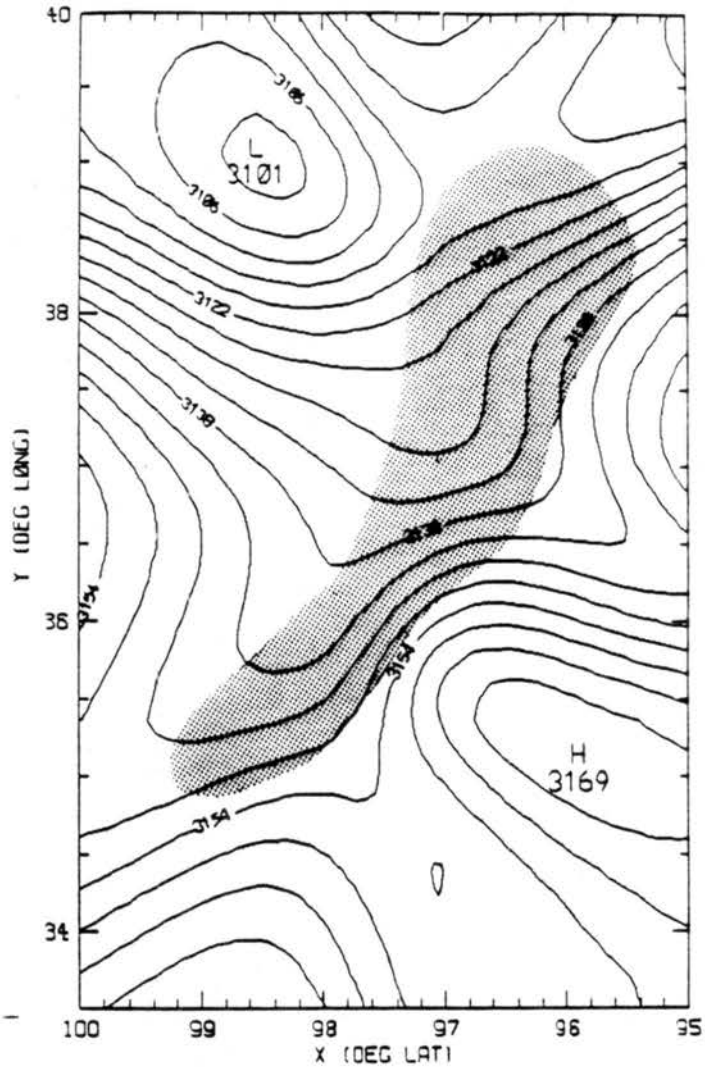

Figure 3.10: As in Fig. 3.8 except at 700 mb.

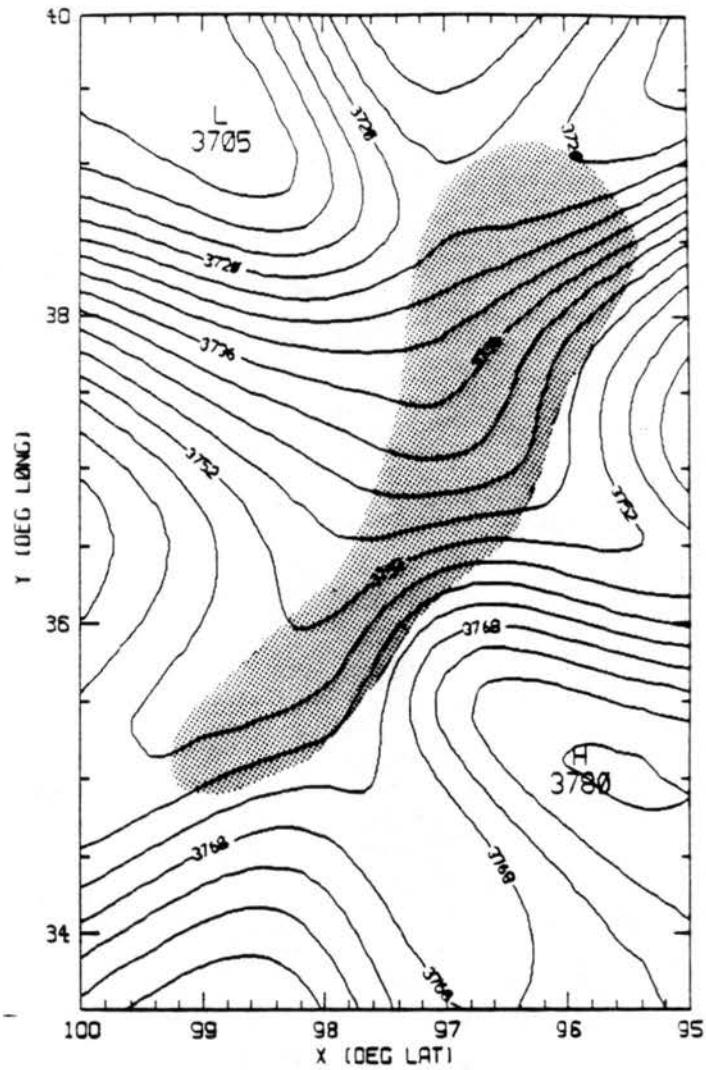

Figure 3.11: As in Fig. 3.8 except at 650 mb.

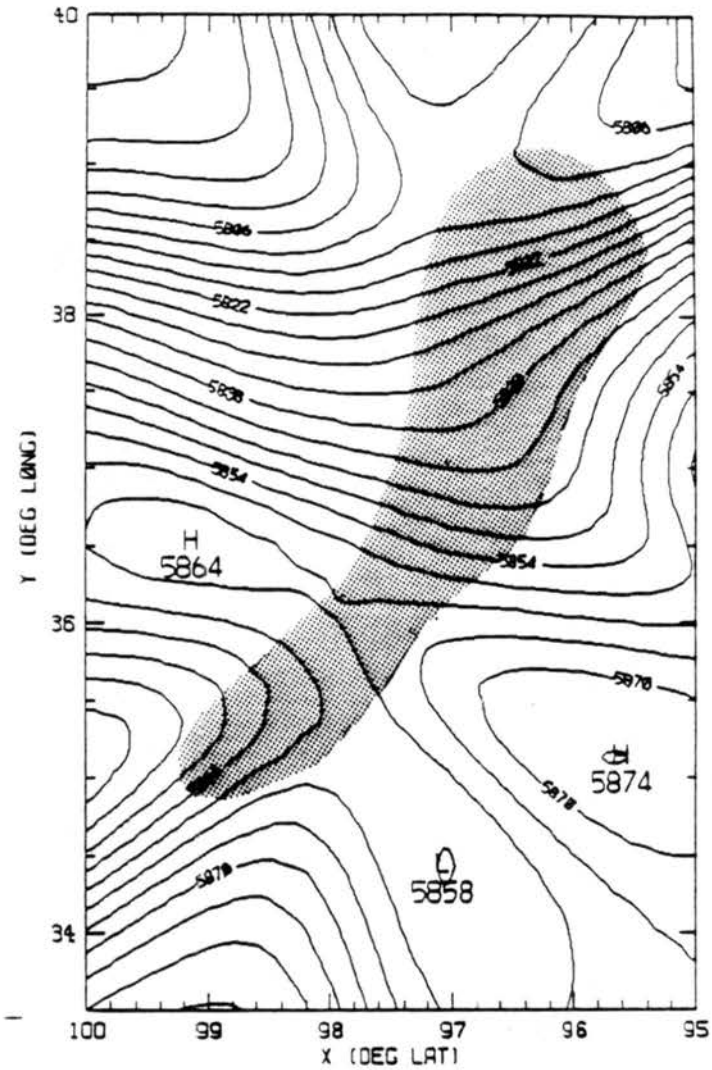

Figure 3.12: As in Fig. 3.8 except at 500 mb.

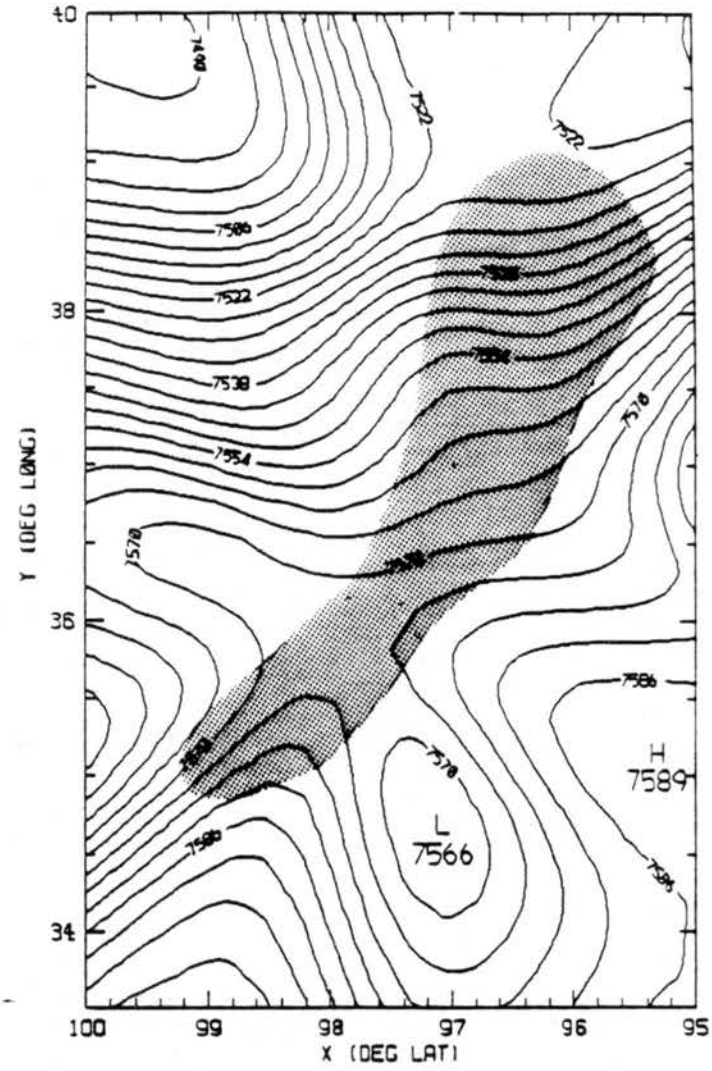

Figure 3.13: As in Fig. 3.8 except at 400 mb.

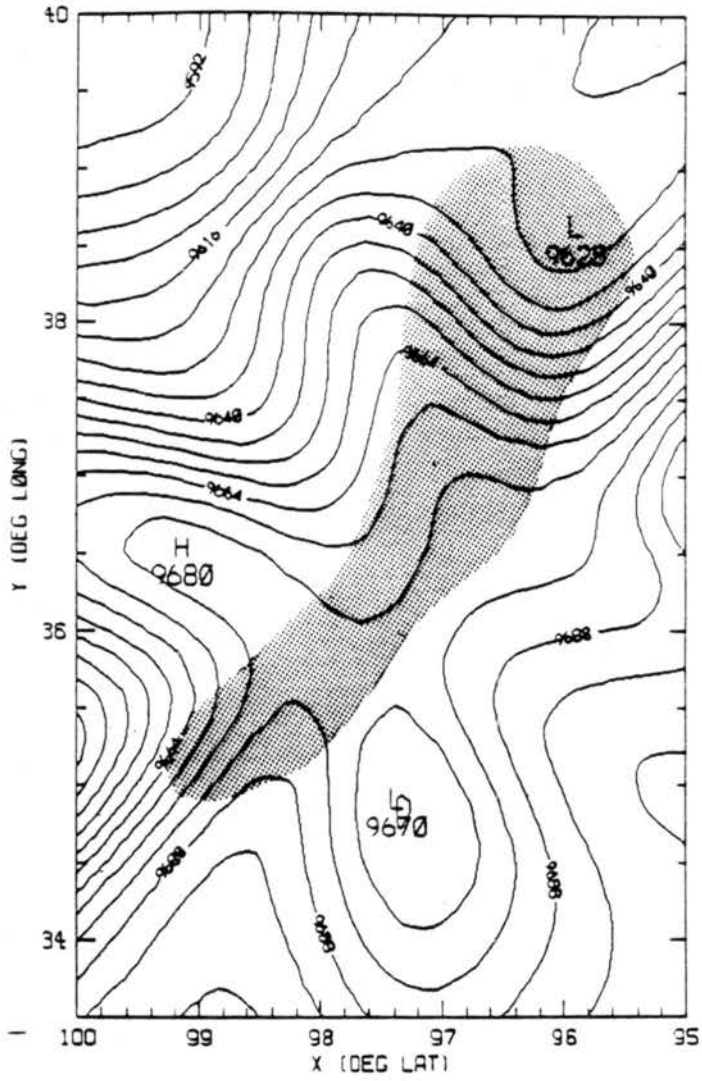

Figure 3.14: As in Fig. 3.8 except at 300 mb.

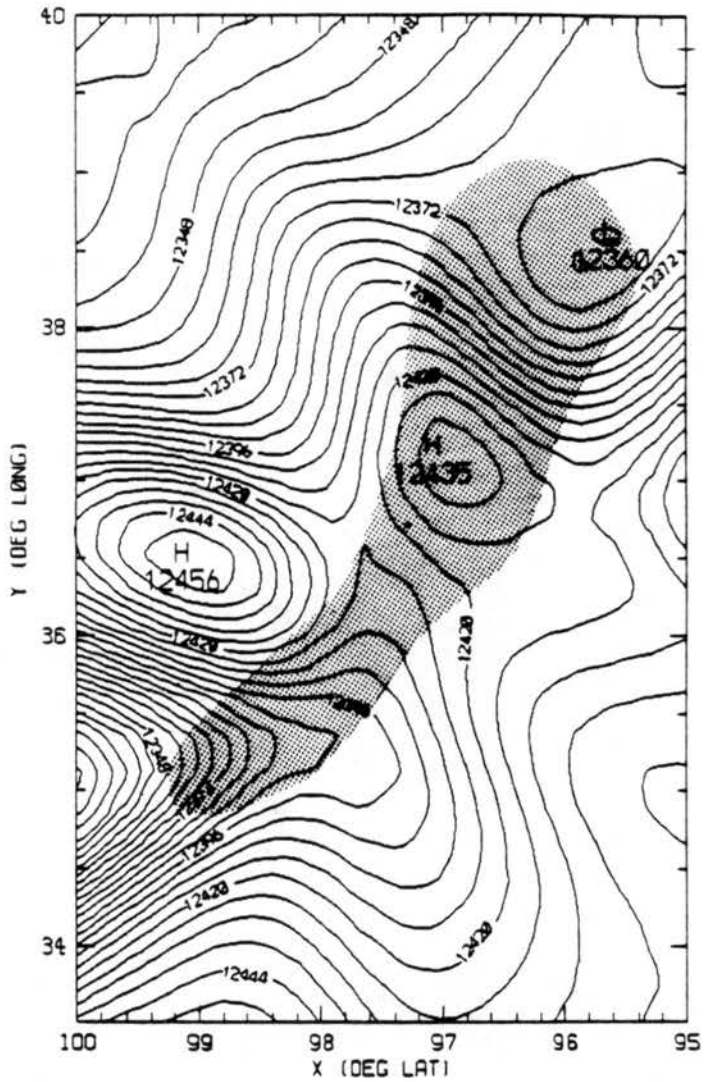

Figure 3.15: As in Fig. 3.8 except at 200 mb.

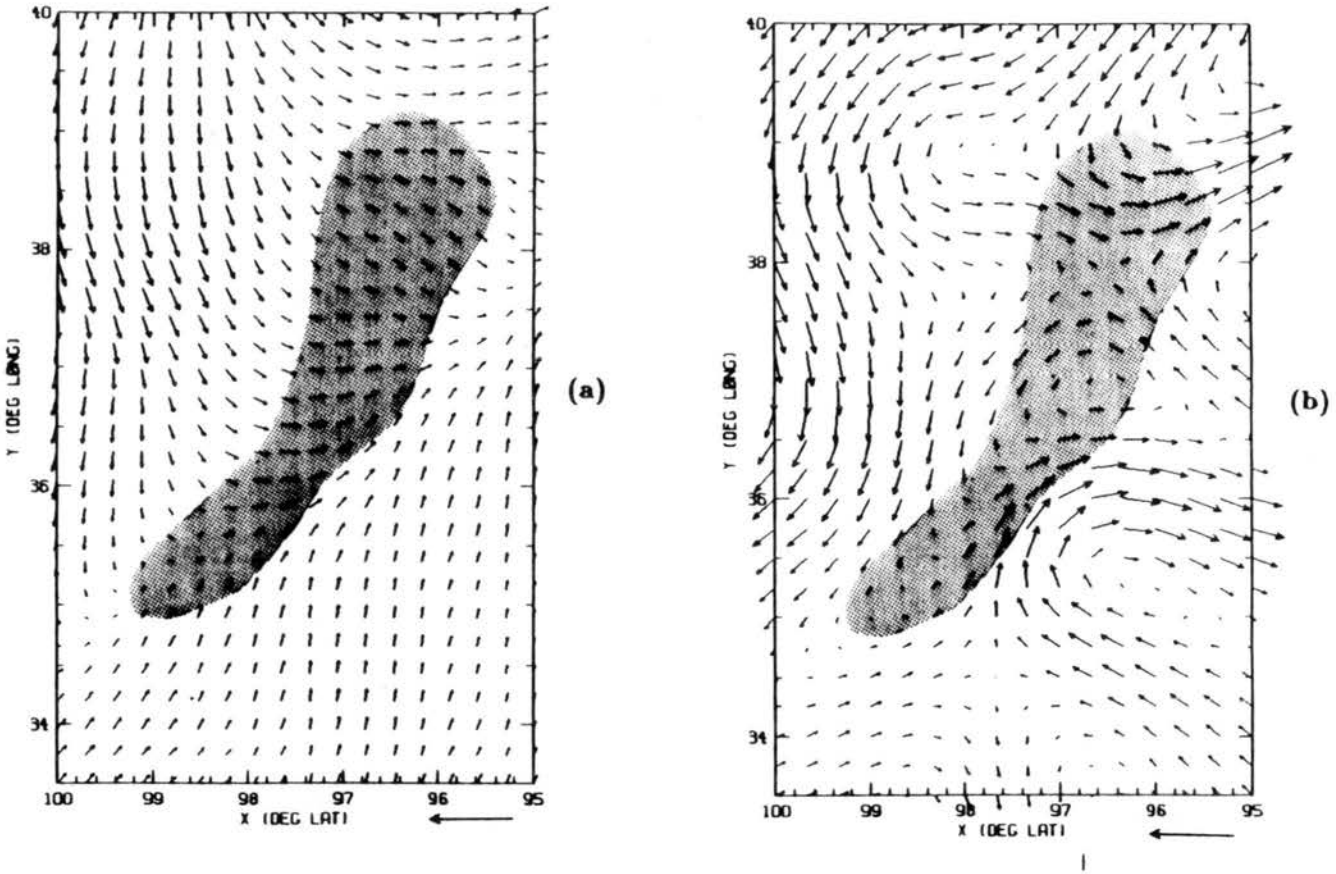

Figure 3.16: Flow pattern at 900 mb for (a) component of the observed flow along the squall line and (b) component of the geostrophic wind along the squall line. Shaded area represents the 15 dBz or greater radar image at 0000Z. Vector along the abscissa represents 60 ms^{-1}.

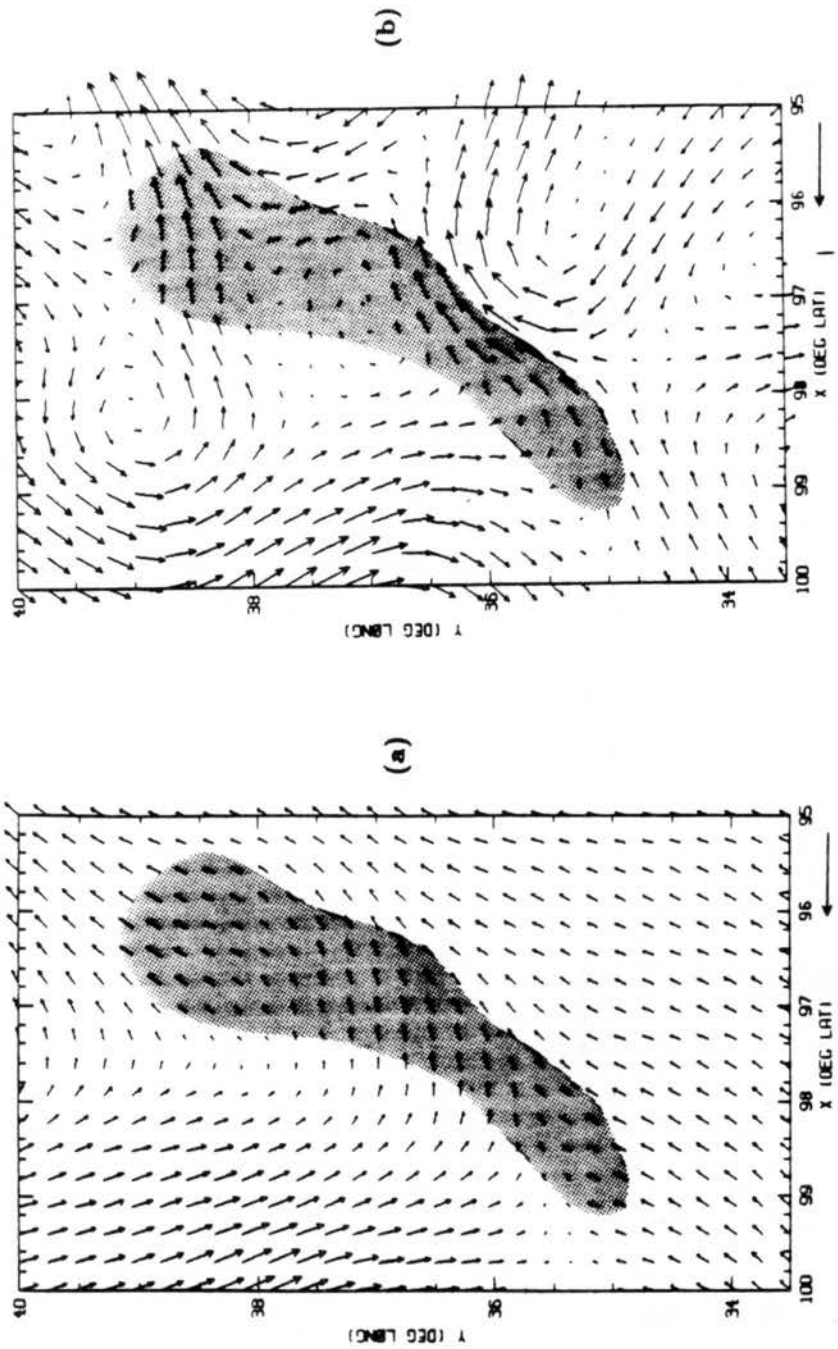

Figure 3.17: As in Fig. 3.16 except at 850 mb.

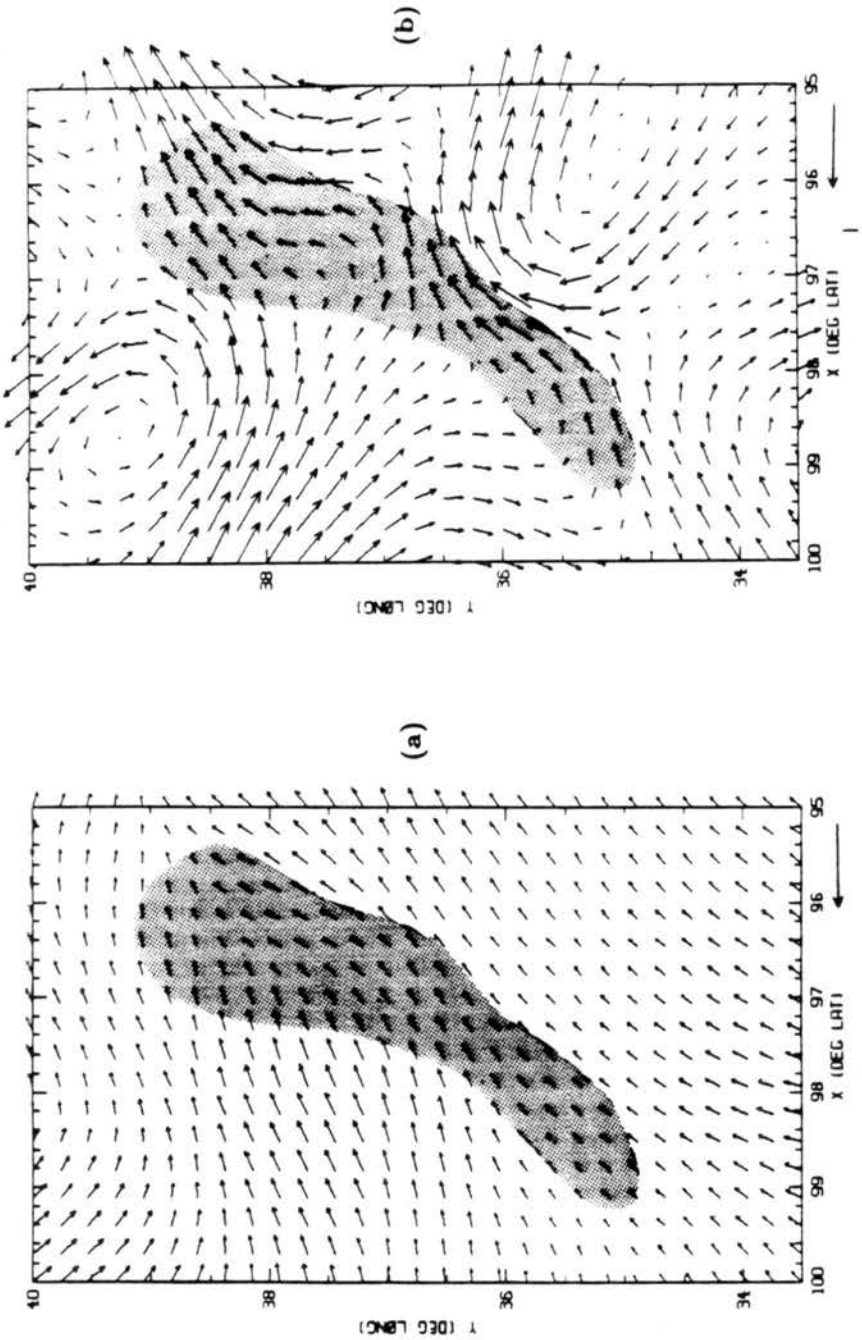

Figure 3.18: As in Fig. 3.16 except at 700 mb.

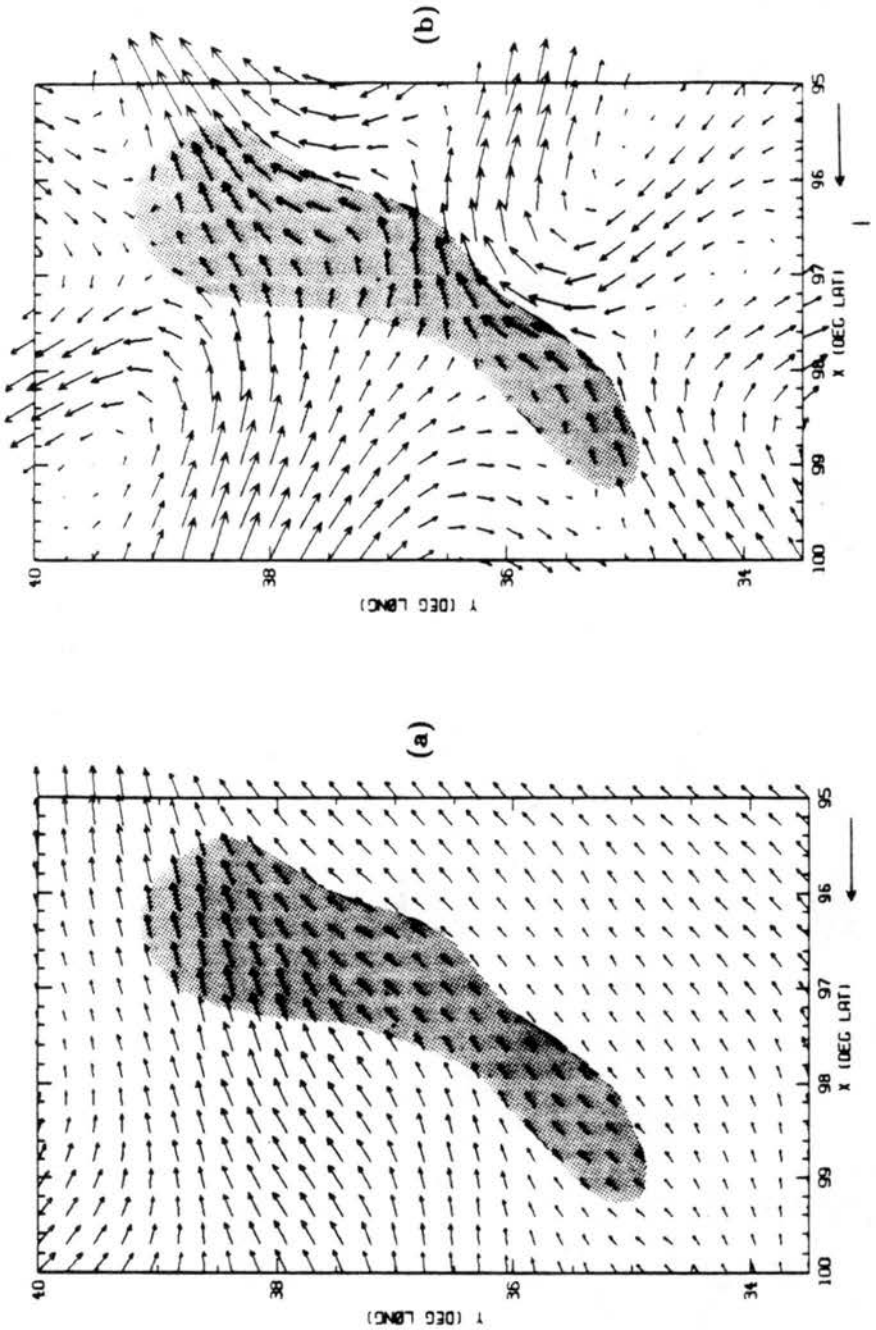

Figure 3.19: As in Fig. 3.16 except at 650 mb.

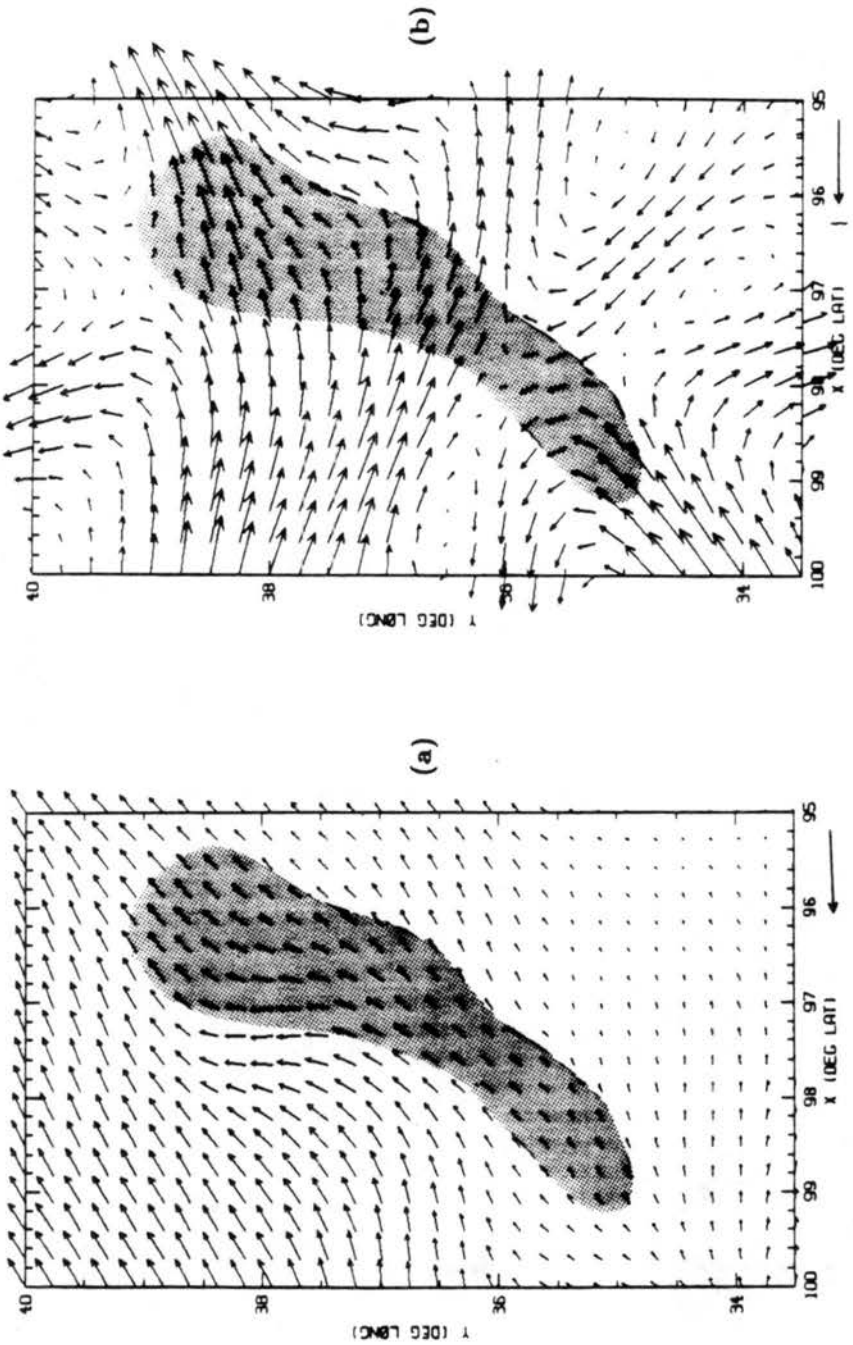

Figure 3.20: As in Fig. 3.16 except at 500 mb.

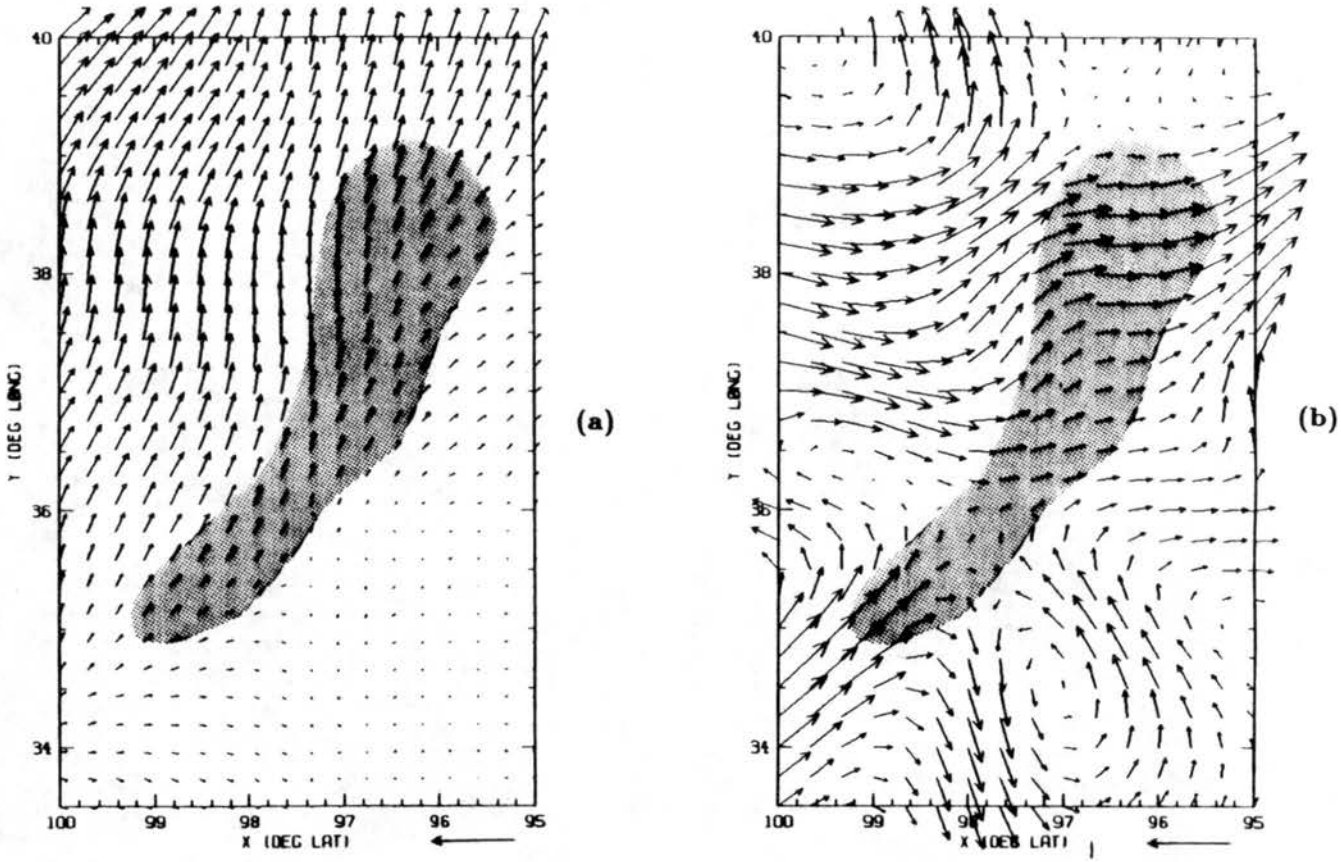

Figure 3.21: As in Fig. 3.16 except at 400 mb.

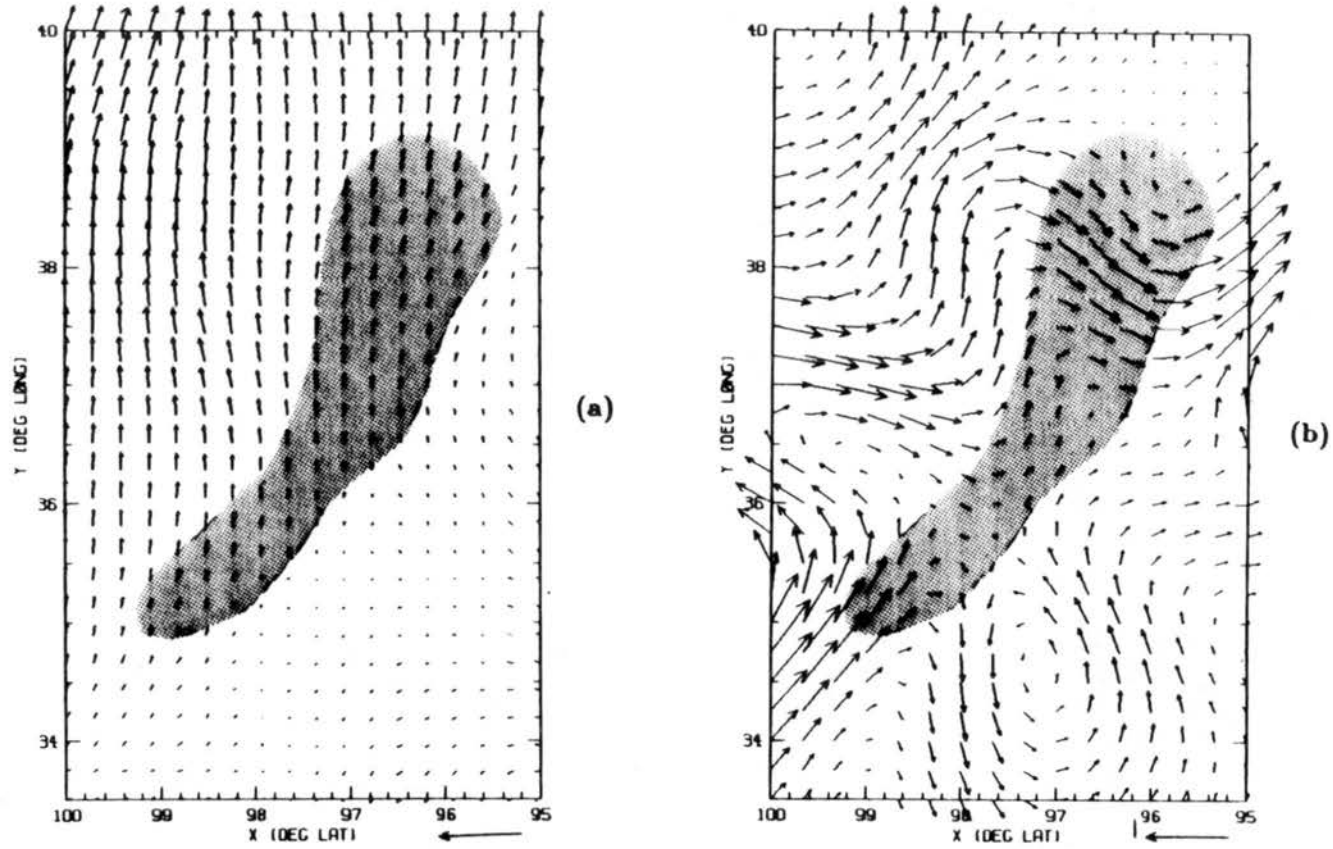

Figure 3.22: Flow pattern at 300 mb for (a) component of the observed flow along the squall line and (b) component of the geostrophic wind along the squall line. Shaded area represents the 15 dBz or greater radar image at 0000Z. Vector along the abscissa represents 100 ms^{-1}.

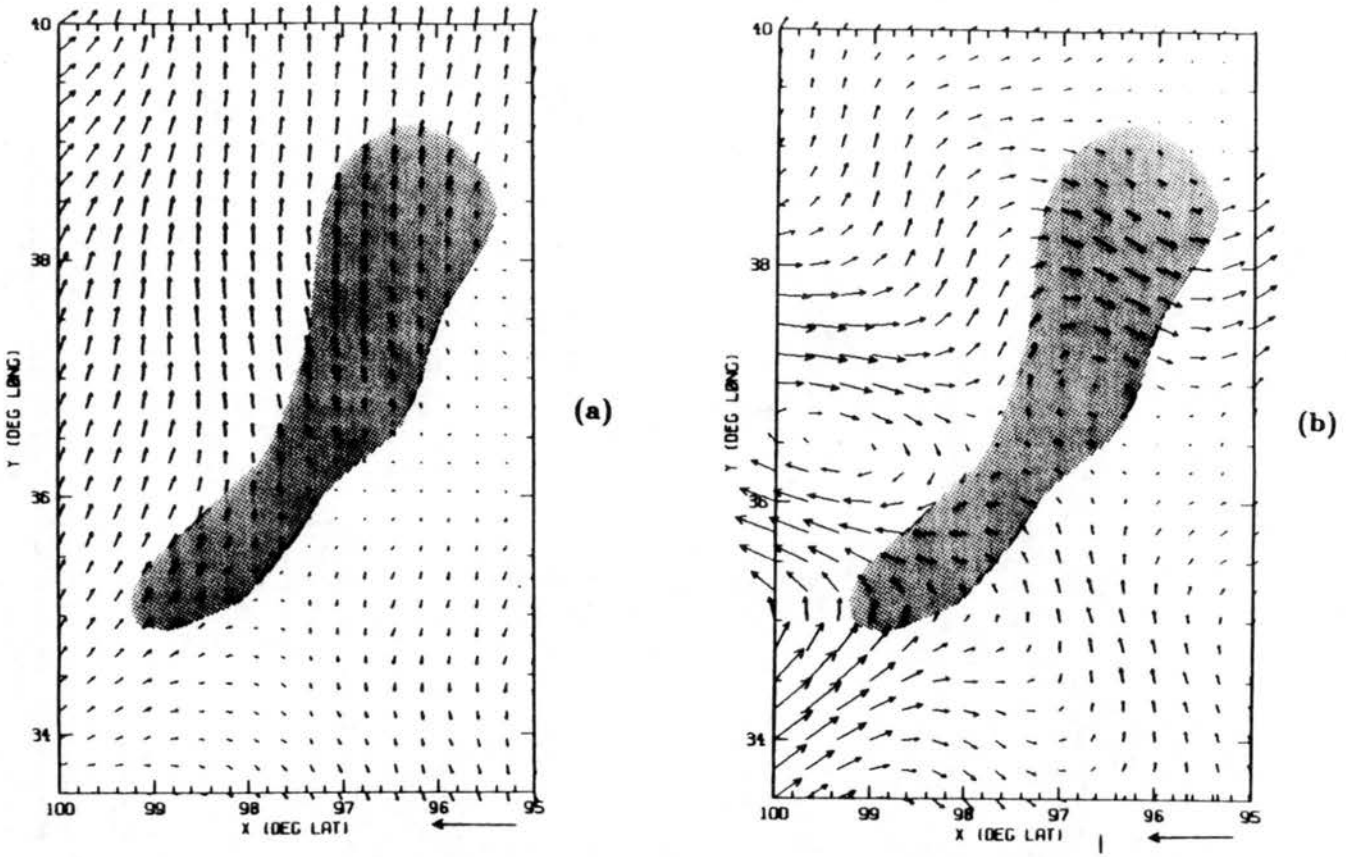

Figure 3.23: Flow pattern at 200 mb for (a) component of the observed flow along the squall line and (b) component of the geostrophic wind along the squall line. Shaded area represents the 15 dBz or greater radar image at 0000Z. Vector along the abscissa represents 100 ms^{-1} in (a) and 200 ms^{-1} in (b).

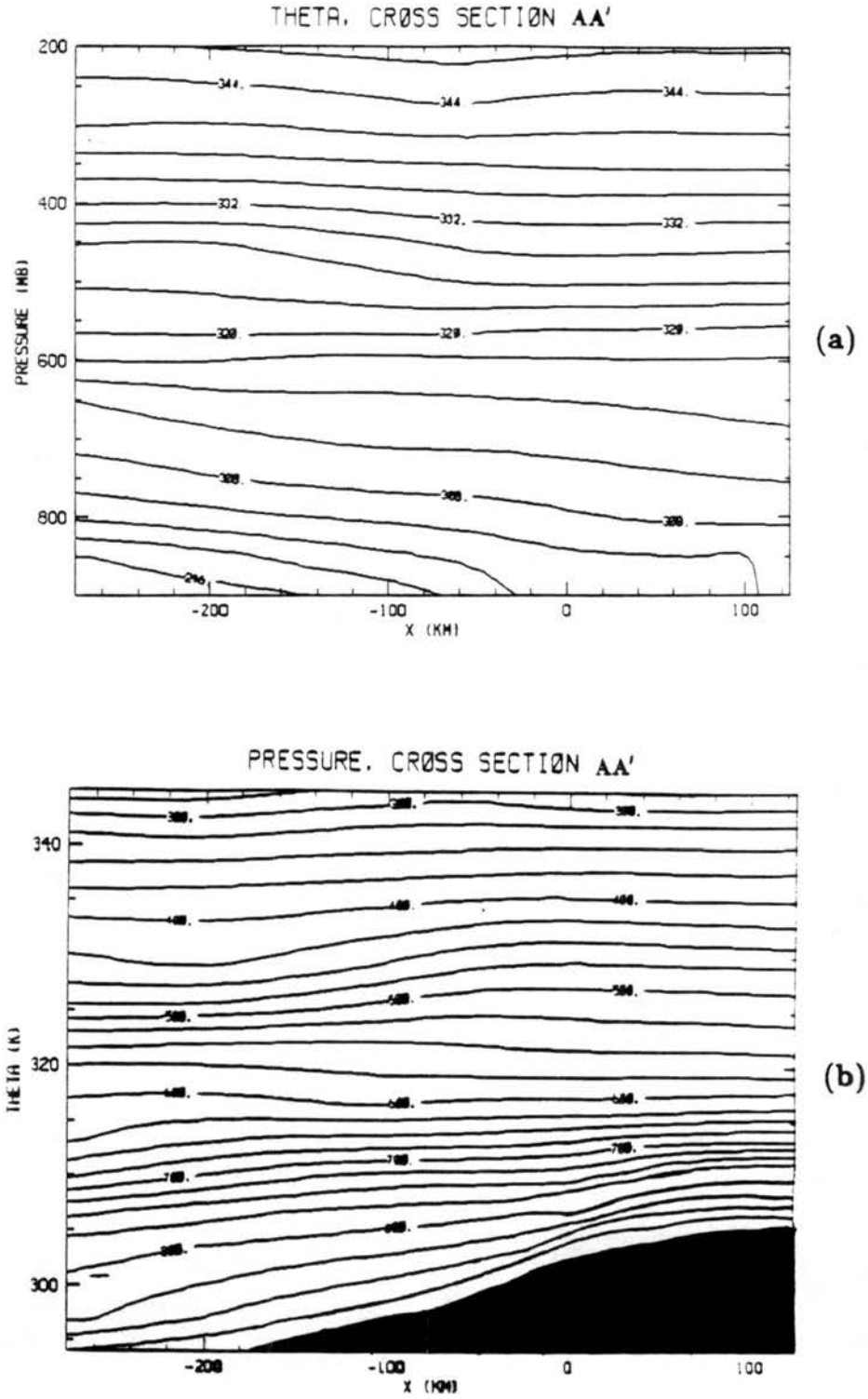

Figure 3.24: (a) Cross section of potential temperature along AA′ with pressure as a vertical coordinate. Contour interval is 3 K. (b) Cross section of pressure along AA′ with potential temperature as a vertical coordinate. Contour interval is 25 mb. The darker line represents the 900 mb surface with hashing under that surface.

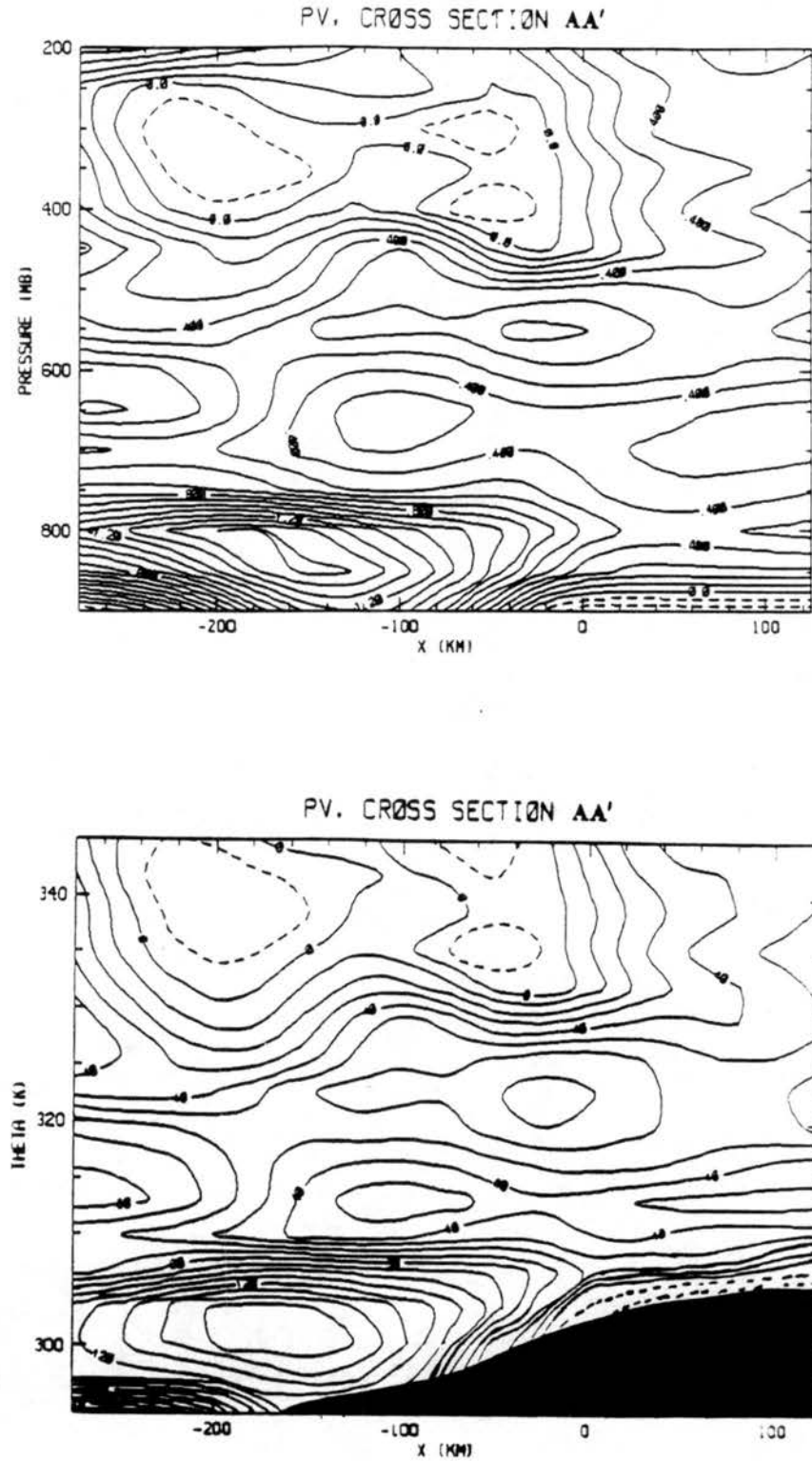

Figure 3.25: Cross section of potential vorticity along AA′ (a) with pressure as the vertical coordinate and (b) with potential temperature as a vertical coordinate. Darker line in (b) represents the 900 mb surface with hashing under that surface.

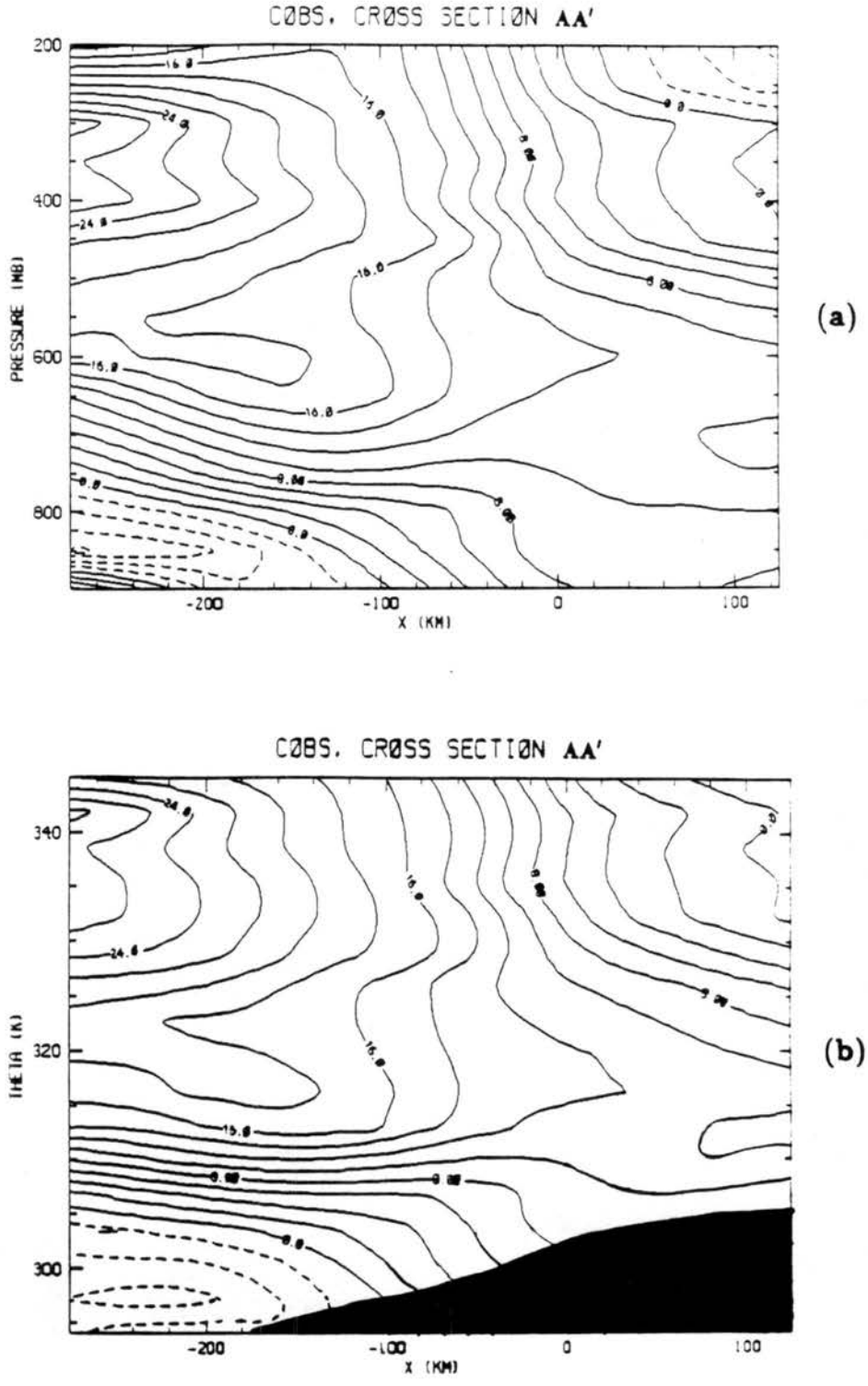

Figure 3.26: As in Fig. 3.25 except for the component of the observed wind along the squall line $V_{\|}$.

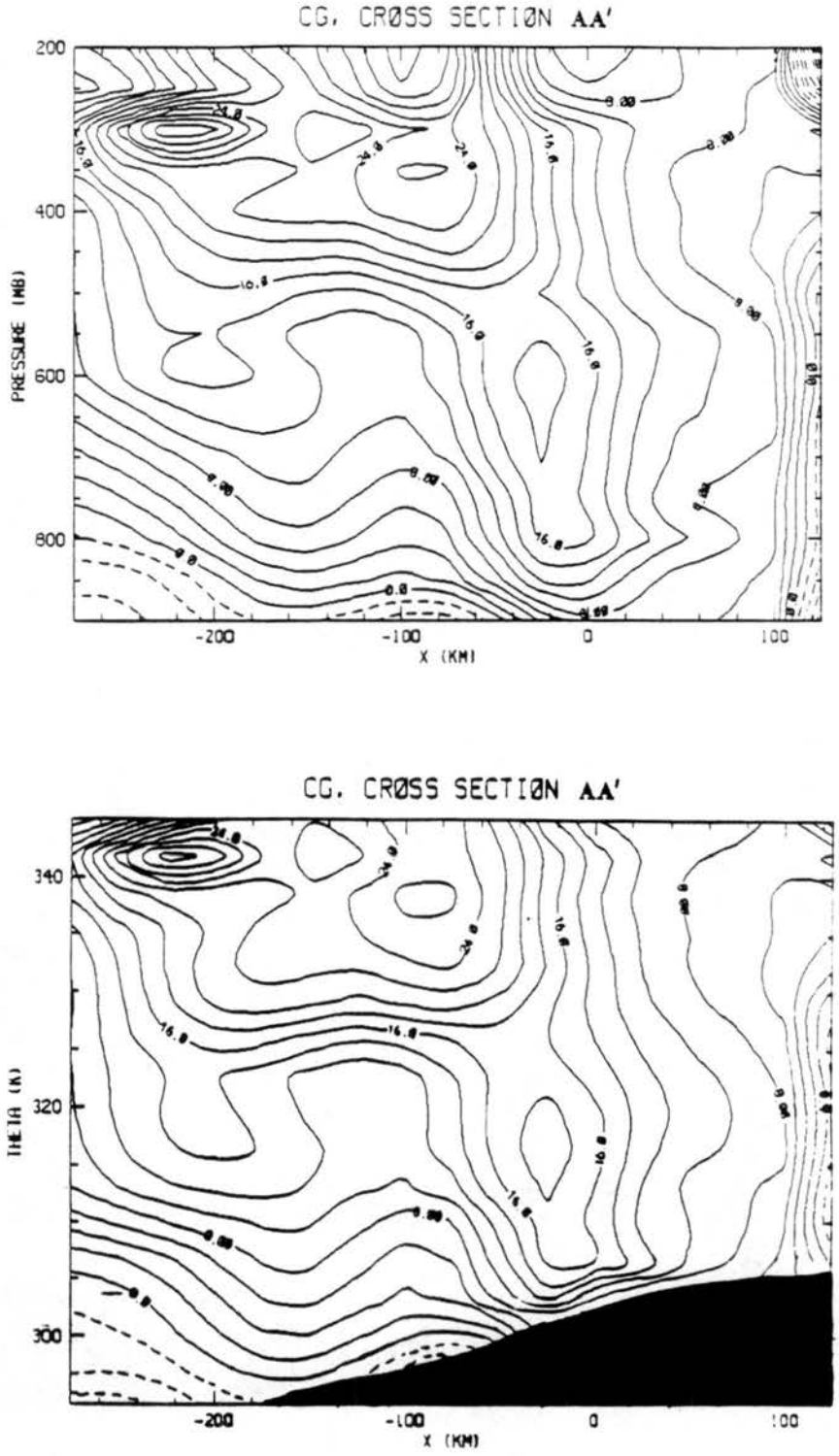

Figure 3.27: As in Fig. 3.25 except for the component of the geostrophic wind along the squall line $V_{g_{\parallel}}$.

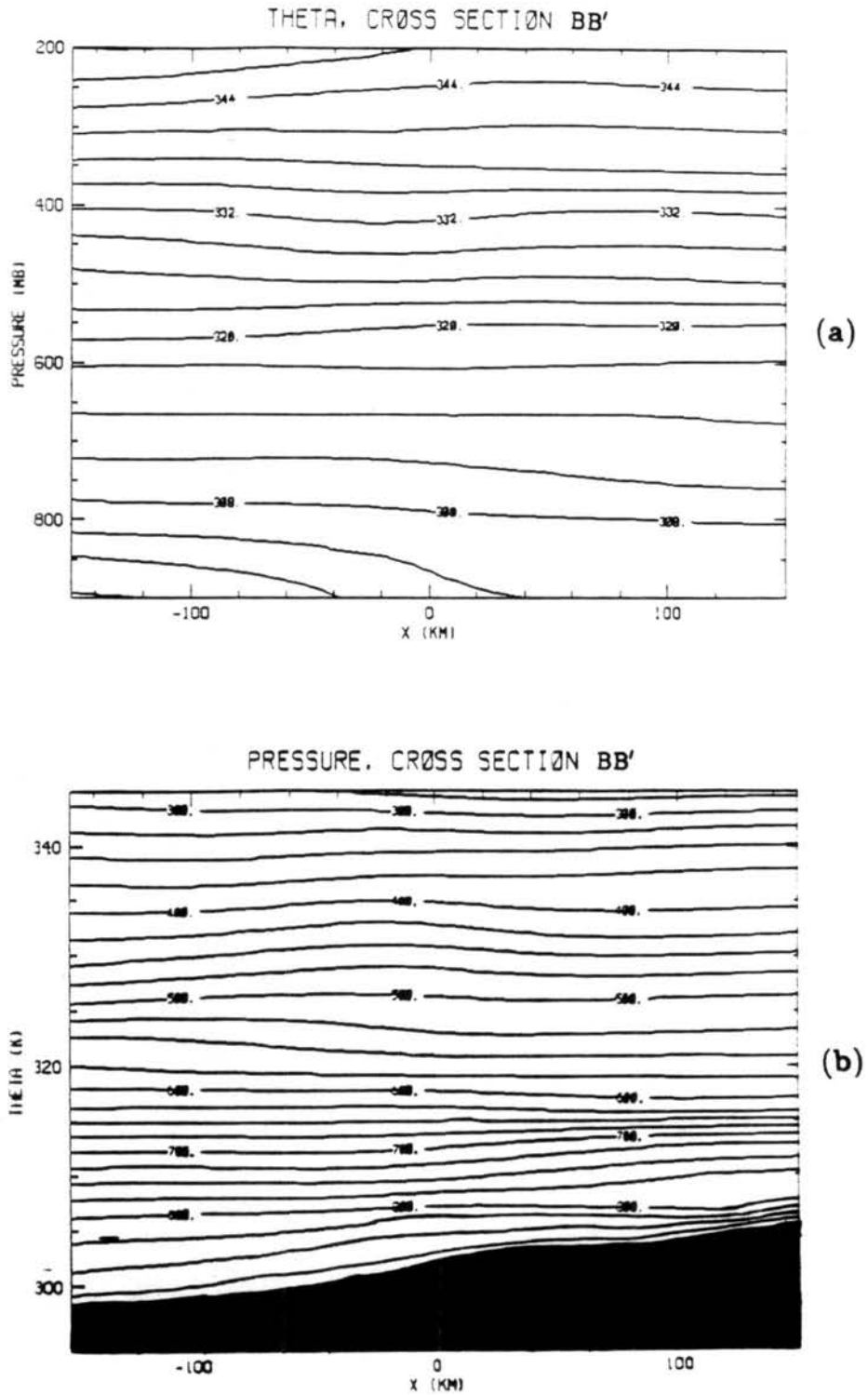

Figure 3.28: As in Fig. 3.24 except along cross section BB′.

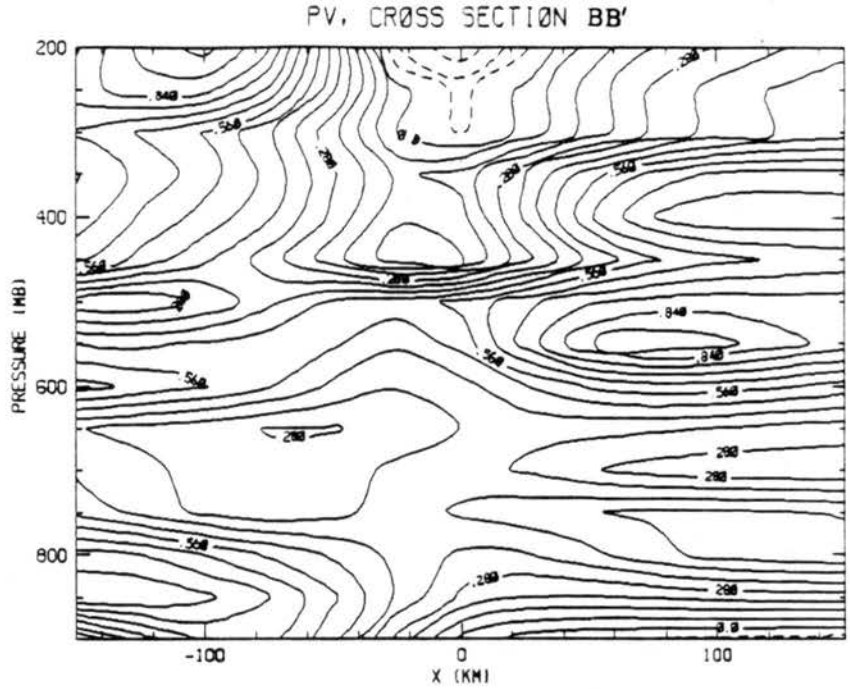

(a)

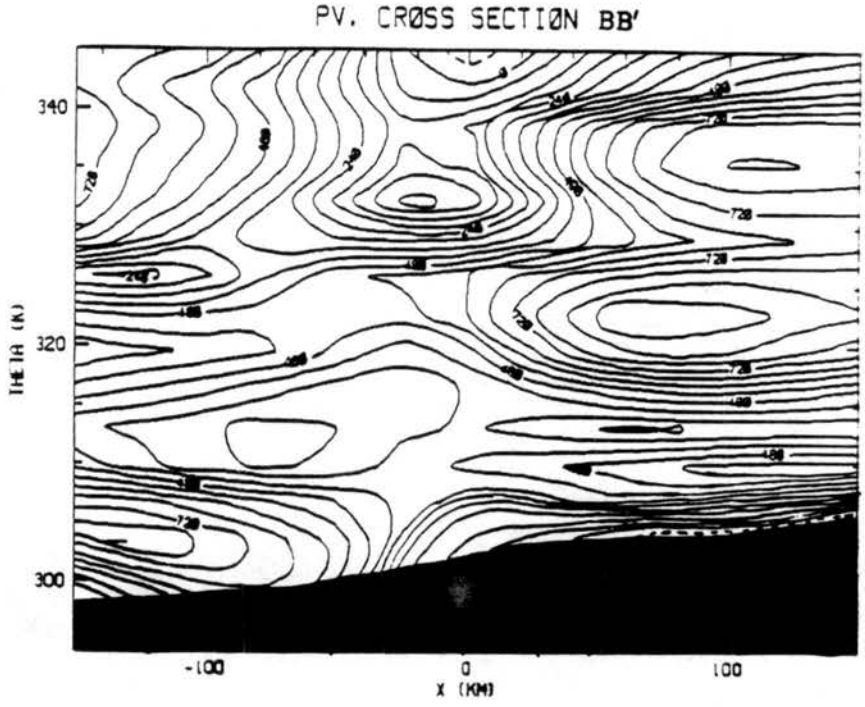

(b)

Figure 3.29: As in Fig. 3.25 except along cross section BB'.

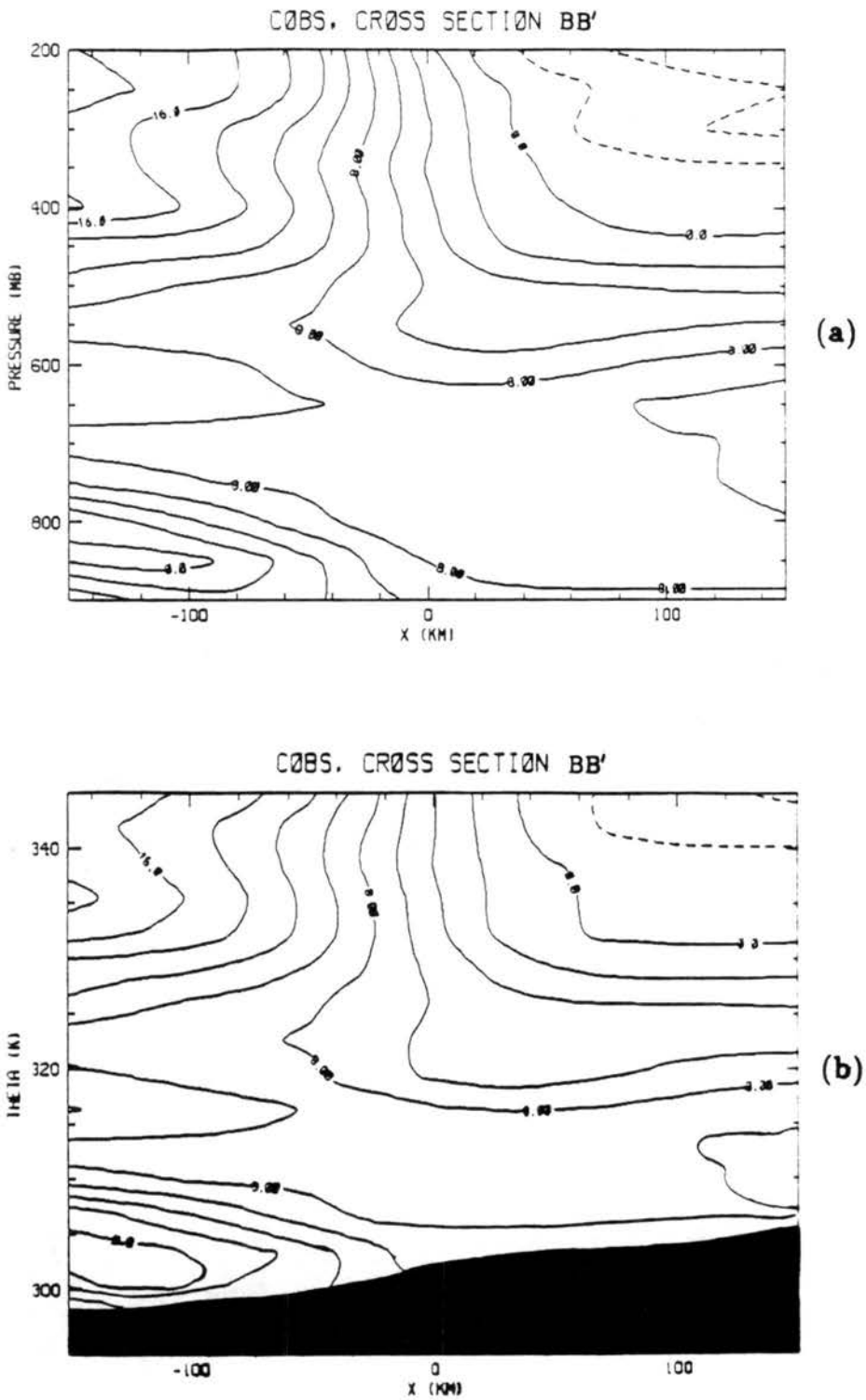

Figure 3.30: As in Fig. 3.26 except along cross section BB′.

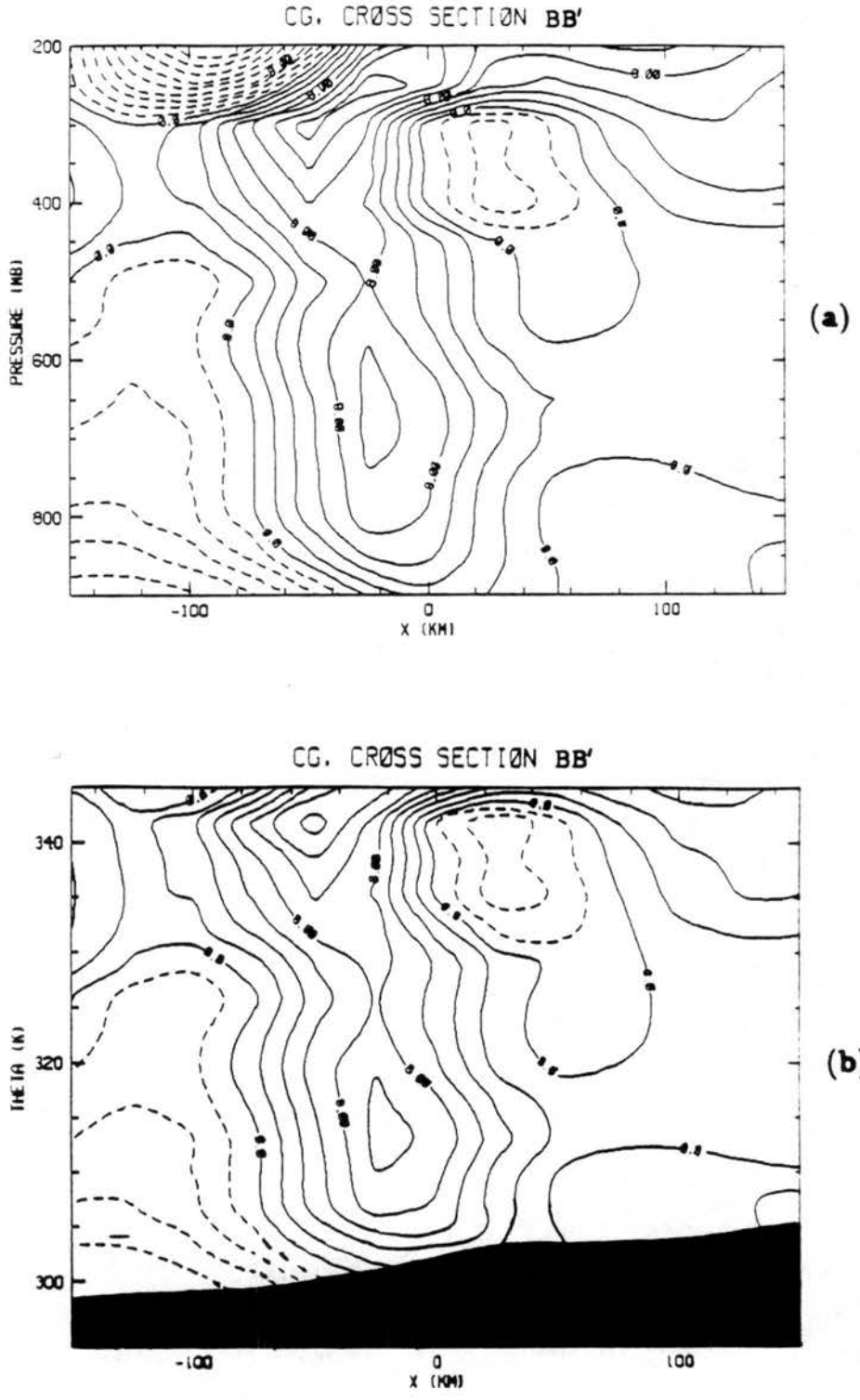

Figure 3.31: As in Fig. 3.27 except along cross section BB′.

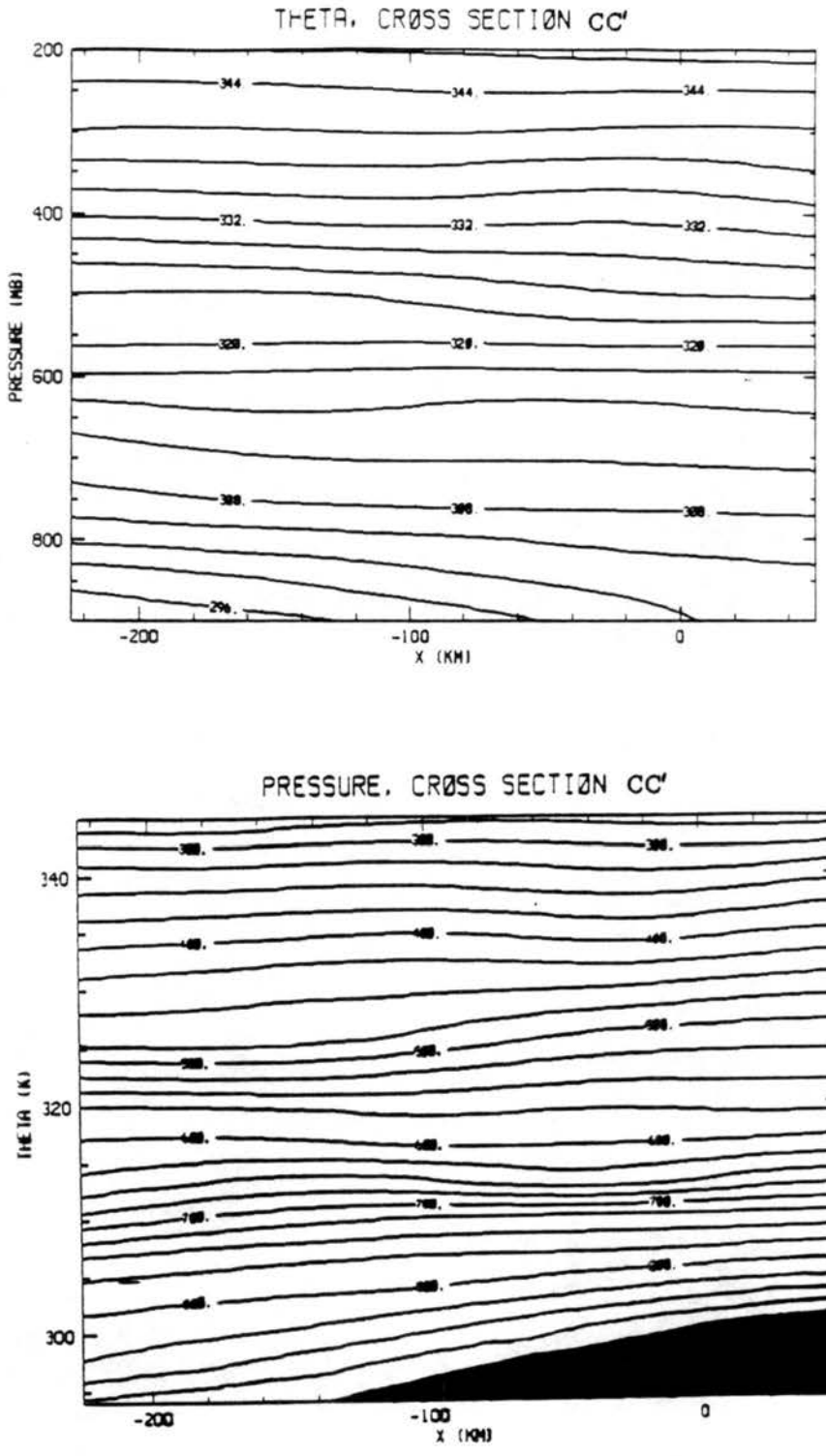

Figure 3.32: As in Fig. 3.24 except along cross section CC′.

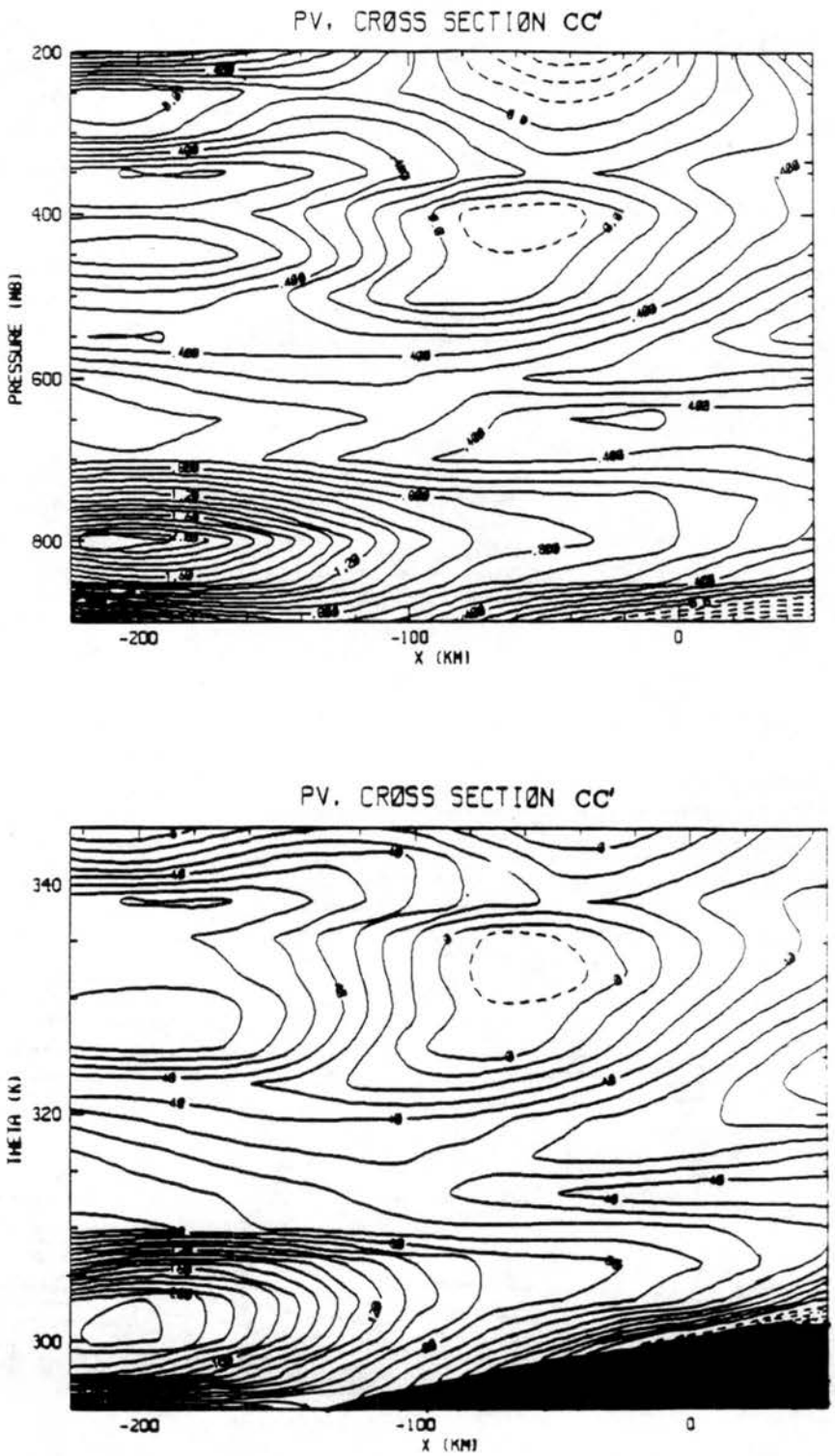

Figure 3.33: As in Fig. 3.25 except along cross section CC′.

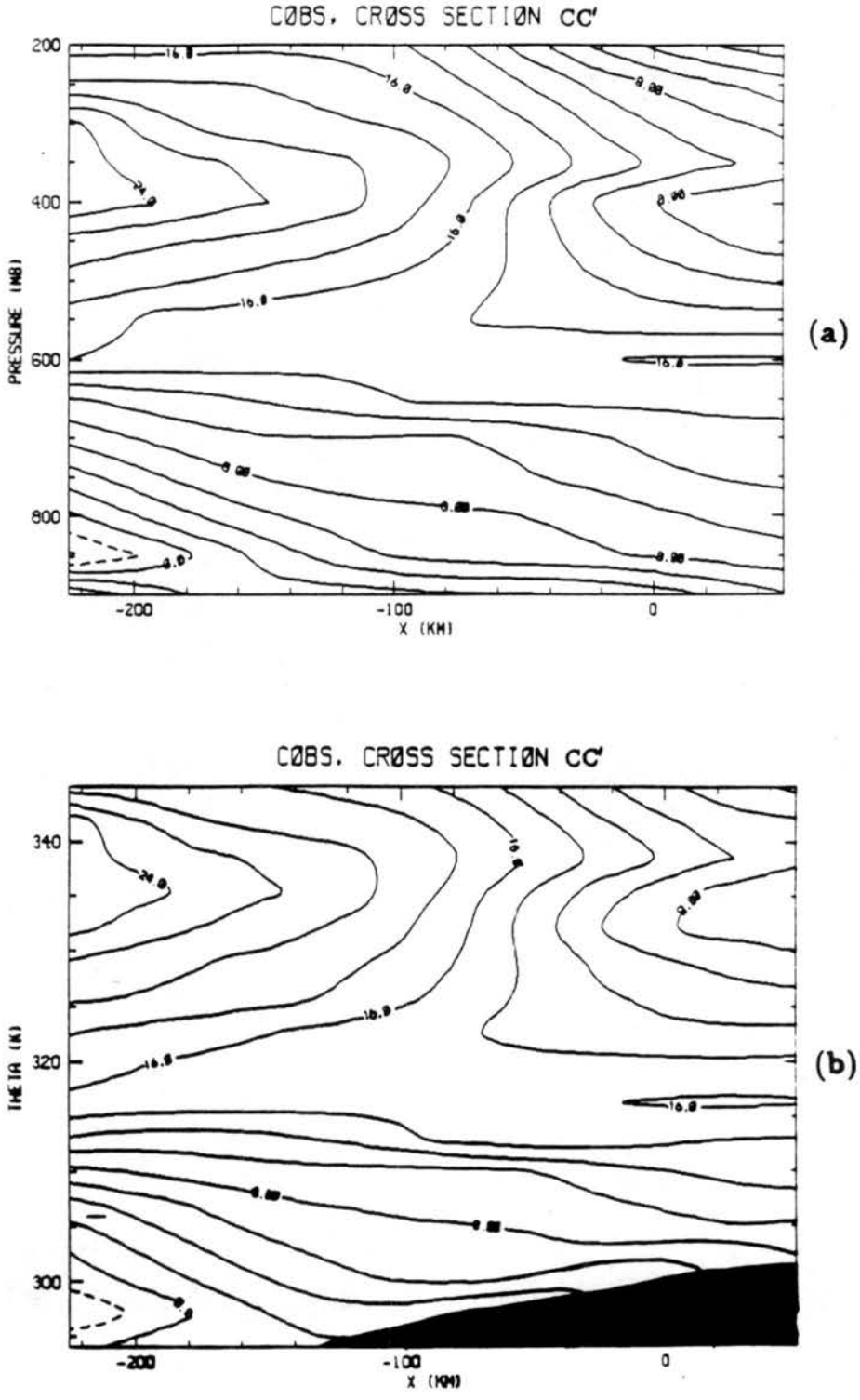

Figure 3.34: As in Fig. 3.26 except along cross section CC′.

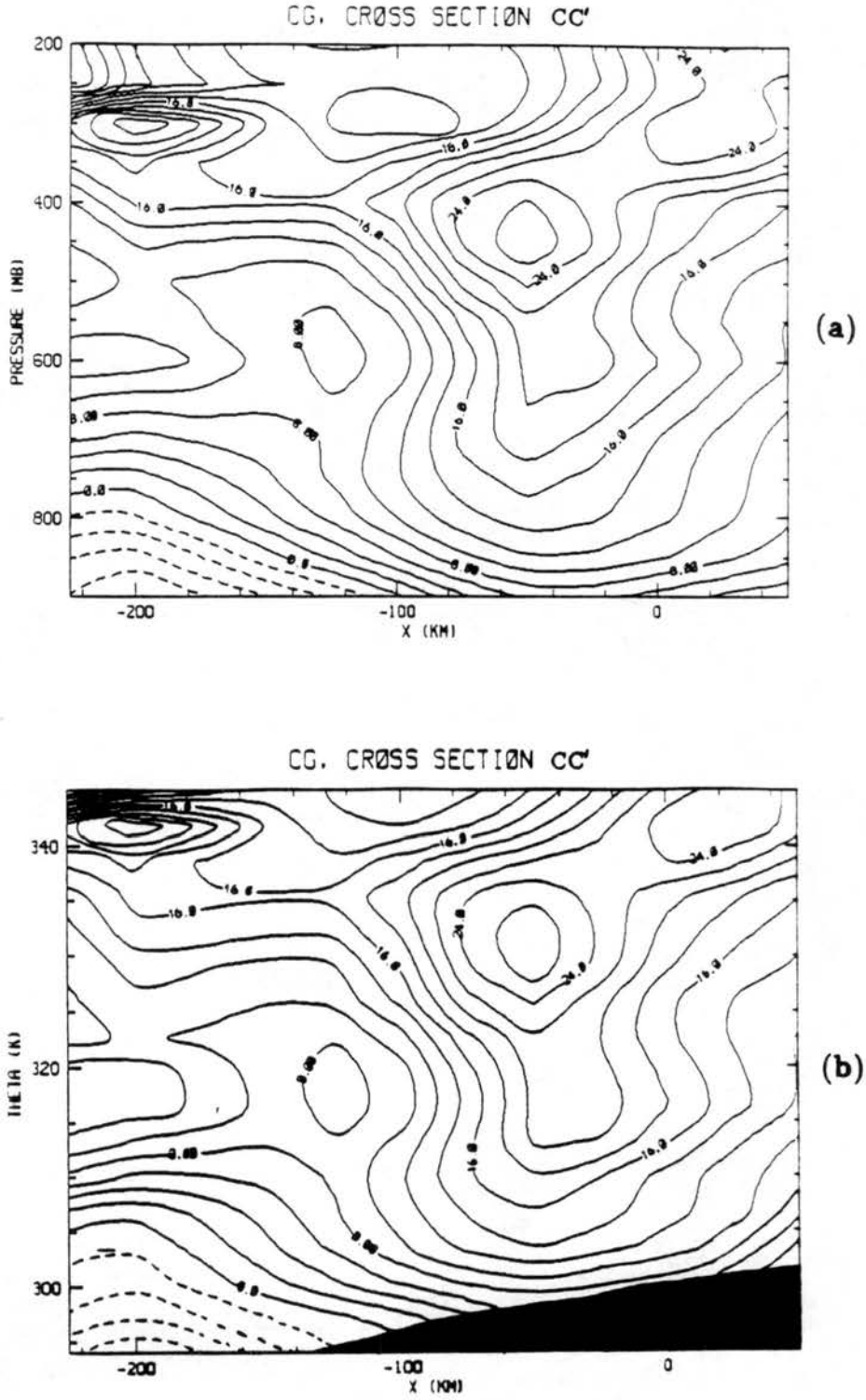

Figure 3.35: As in Fig. 3.27 except along cross section CC′.

Chapter 4

CONCLUSIONS

In this chapter comparisons will be made between model and observational results. Concluding remarks will be given as well as recommendations for further study.

The two-dimensional model predicts potential vorticity q anomalies induced by the passage of a squall line. Using model results from the general case as an example (Fig. 2.2), q increased to about 2.1 times its unperturbed value in the lower troposphere and decreased by about 0.5 times in the upper troposphere. Observational results are in qualitative agreement with the model results. Cross sections AA′ (Fig. 3.25) and CC′ (Fig. 3.33) show increasing q in the lower troposphere and decreasing q in the upper troposphere behind the squall line. However, the observed anomalies are stronger by a factor of approximately 2 compared with the model results. Caution is required in comparing the location of the q anomaly from model and observed results since the scale on the horizontal axes are much different.

Pressure fields as diagnosed by the model (Fig. 2.3) show a destabilization of the mid to upper troposphere and stabilization of the lower troposphere behind the squall line. Observations of the perturbation pressure fields (e.g., Fig. 3.24b) reveals stabilization of the lower troposphere and destabilization at about 500 mb. The layer centered at about 700 mb behind the squall line (Fig. 3.24b) appears to also shows destabilization, but examination of the pre-squall line pressure field at 700 mb shows that the isobars have become somewhat less closely packed (i.e., stabilization).

Model predicted geostrophic flow along the squall line (Fig. 2.3) shows cyclonic shear in the lower troposphere and anticyclonic shear in the upper troposphere. Assuming that the simulated squall line is aligned north-south, then flow into the page ahead of the

squall line is southerly. In this sense the squall line has induced southerly flow ahead and northerly flow behind the squall line in the lower troposphere. This flow pattern is reversed in the upper troposphere. Geostrophic wind along the observed squall line calculated from the geopotential height fields show agreement with the model results behind the squall line for cross sections AA′ and CC′ (Figs. 3.27a and 3.35a respectively). Magnitudes of the observed lower troposphere northeasterly flow is weaker and upper troposphere southwesterly flow is stronger than the model results (recall the observed squall line was aligned southwest-northeast). The model is diagnosing only geostrophic flow induced by the squall line, the magnitude of the observed geostrophic flow is probably somewhat influenced by the ambient flow, which may account for the difference in magnitude between model and observational results. Geostrophic flow ahead of the squall line as predicted by the model does not appear to be well substantiated by the observational results. This may be because the observational analysis extends only about 100 km ahead of the squall line, thus this analysis may not extend far enough ahead of the squall line to pick up these features.

There are differences in magnitudes between potential vorticity and geostrophic flows when comparing the model and observational results. However, comparisons of the model and observational results show that the model does predict many of the features associated with the observed squall line. Thus, the model, with its simple parameterization of the squall line as a moving heat source (2.30) captures the essence of these fields.

I have several recommendations for further study for the modeling study. Various interesting experimental runs can be made by varying the heating function $\dot{\theta}$. First, for the experiments described in this study, $\dot{\theta}$ was chosen as proportional to sin $(\Theta - \Theta_B)/(\Theta_T - \Theta_B)$, which is an approximation to the apparent heat source for tropical cloud clusters found by Yanai et al. (1973). Other vertical structures of $\dot{\theta}$ could be used to study their effect on the potential vorticity anomaly produced.

Further experiments could be performed to more realistically parameterize $\dot{\theta}$. One such experiment would define $\dot{\theta}$ such that it also represents cooling due to precipitation and evaporation processes below the stratiform region. In addition, $\dot{\theta}$ could be extended

horizontally in the region to the rear of the squall line in the upper troposphere to represent latent heating effects in the stratiform region. A second experiment (possibly in conjunction with the first) would extend the heating up into the stratosphere, simulating convection which overshoots into the stratosphere.

It would also be interesting to test the hypothesis that the upper level destabilization induced by the potential vorticity anomaly forms a background state for the stratiform rain region. This would be accomplished by quantifying the destabilization in the mid to upper troposphere to study whether this destabilization could account for a mesoscale updraft.

As a recommendation for the observational study, it would be of interest to analyse a second PRE-STORM case. The 26-27 June 1985 squall line was not a very intense storm. Another case, the 10-11 June 1985 squall line was one of the stronger squall lines during PRE-STORM (Richard Johnson, personal communication). Cross sections similar to those produced in this study would be useful in verifying the results in the observational study to investigate whether these features are general to squall lines.

REFERENCES

Andrews, D. G., 1983: A finite-amplitude Eliassen-Palm theorem in isentropic coordinates. *J. Atmos. Sci.*, **40**, 1877–1883.

Barnes, S.L., 1964: A technique for maximizing details in numerical weather map analysis. *J. Appl. Meteor.*, **3**, 396–409.

Bretherton, F. P., 1966: Critical layer instability in baroclinic flows. *Quart. J. R. Met. Soc.*, **92**, 325–334.

Ciesielski, P.E., S.R. Fulton and W.H. Schubert, 1986: Multigrid solution of an elliptic boundary value problem from tropical cyclone theory. *Mon. Wea. Rev.*, **114**, 797–807.

Eliassen, A., 1948: The quasi-static equations of motion. *Geofys. Publ.*, **17**(3).

Fulton, S.R., 1988: Multigrid solution of the semi-geostrophic invertibility relation. Submitted to *Mon. Wea. Rev.*

Fulton, S.R., P.E. Ciesielski and W.H. Schubert, 1986: Multigrid methods for elliptic problems: a review. *Mon. Wea. Rev.*, **114**, 943–959.

Gamache, J. F., and R. A. Houze, Jr., 1982: Mesoscale air motions associated with a tropical squall line. *Mon. Wea. Rev.*, **110**, 118–135.

Gamache, J. F., and R. A. Houze, Jr., 1983: Water budget of a mesoscale convective system in the tropics. *J. Atmos. Sci.*, **40**, 1835–1850.

Haynes, P.H., and M.E. McIntyre, 1987: On the evolution of vorticity and potential vorticity in the presence of diabatic heating and frictional or other forces. *J. Atmos. Sci.*, **44**, 828–841.

Hoskins, B. J., 1975: The geostrophic momentum approximation and the semi-geostrophic equations. *J. Atmos. Sci.*, **32**, 233–242.

Hoskins, B. J., and I. Draghici, 1977: The forcing of ageostrophic motion according to the semi-geostrophic equations and in an isentropic coordinate model. *J. Atmos. Sci.*, **34**, 1859–1867.

Hoskins, B. J., M. E. McIntyre and A. W. Robertson, 1985: On the use and significance of isentropic potential vorticity maps. *Quart. J. R. Met. Soc.*, **111**, 877–946.

Johnson, R.H., and R.A. Houze, Jr., 1987: Precipitating cloud systems of the Asian Monsoon. *Monsoon Meteorology*, C.-P. Ghang and T.N. Krishnamurti, Eds., Oxford University Press, New York, 298–353.

Johnson, R.H., and W.A. Gallus, 1988: The wake structure of an intense midlatitude squall line in OK PRE-STORM. Preprint Volume 15th Conference on Severe Local Storms, Baltimore, Maryland, 229–232.

Johnson, R.H., and P.J. Hamilton, 1988: The relationship of surface features to the precipitation and airflow structure of an intense midlatitude squall line. *Mon. Wea. Rev.*, **116**, 1444–1472.

Lorenz, E. N., 1955: Available potential energy and the maintenance of the general circulation. *Tellus*, **7**, 157–167.

Meit'in, J.G., Jr. and J.B. Cunning, 1985: The Oklahoma-Kansas preliminary experiment for STORM-Central. Vol I-Daily operations summary, NOAA Tech. Memo, ERL ESG-20, Boulder, Colorado, 80303, 312 pp.

Ogura, Y., and Y.-L. Chen, 1977: A life history of an intense mesoscale convective storm in Oklahoma. *J. Atmos. Sci.*, **34**, 1458–1476.

Ogura, Y., and M.-T. Liou, 1980: The structure of a midlatitude squall line: A case study. *J. Atmos. Sci.*, **37**, 553–567.

Schubert, W.H., and B.T. Alworth, 1987: Evolution of potential vorticity in tropical cyclones. *Quart. J.R. Met. Soc.*, **113**, 147–162.

Schubert, W.H., S.R. Fulton and R.F.A. Hertenstein, 1988: Balanced atmospheric response to squall lines. Submitted to *J. Atmos. Sci.*

U.S. Standard Atmosphere Supplements, 1966, U.S. Government Printing Office, Washington D.C., 20402.

Yanai, M., S. Esbensen and J. Chu, 1973: Determination of bulk properties of tropical cloud clusters from large-scale heat and moisture budgets. *J. Atmos. Sci.*, **30**, 611-627.

)GRAPHIC DATA	1. Report No.	2.	3. Recipient's Accession No.
tle and Subtitle	Modeling and Observations of the Atmospheric Response to Squall Lines		5. Report Date November, 1988
			6.
thor(s) Rolf F.A. Hertenstein			8. Performing Organization Rept. No.
rforming Organization Name and Address partment of Atmospheric Science lorado State University Collins, Colorado 80523			10. Project/Task/Work Unit No. 11. Contract/Grant No. ATM 8510664
onsoring Organization Name and Address tional Science Foundation			13. Type of Report & Period Covered 14.

)plementary Notes

stracts

In order to study the atmospheric response to a moving squall line a two-dimensional rsion of the semi-geostrophic theory on isentropic coordinates is used. This model duces to a system of two equations which includes the predictive equation of the tential pseudo-density (or inverse potential vorticity), and an invertibility inciple which can be solved for the Bernoulli function. Wind and mass fields can diagnosed for the solutions of the Bernoulli function.

The two-dimensional model incorporates very simple physics; specifically, it does capture the complicated moist physics associated with a squall line. However, nparisons of the model and observational results show that the model does predict ny of the features associated with the observed squall line.

Words and Document Analysis. 17a. Descriptors

squall lines
potential vorticity
semi-geostrophic theory

entifiers/Open-Ended Terms

SATI Field/Group

lability Statement	19. Security Class (This Report) UNCLASSIFIED	21. No. of Pages
	20. Security Class (This Page) UNCLASSIFIED	22. Price

-35 (Rev. 3-72)